

AD-A122 131

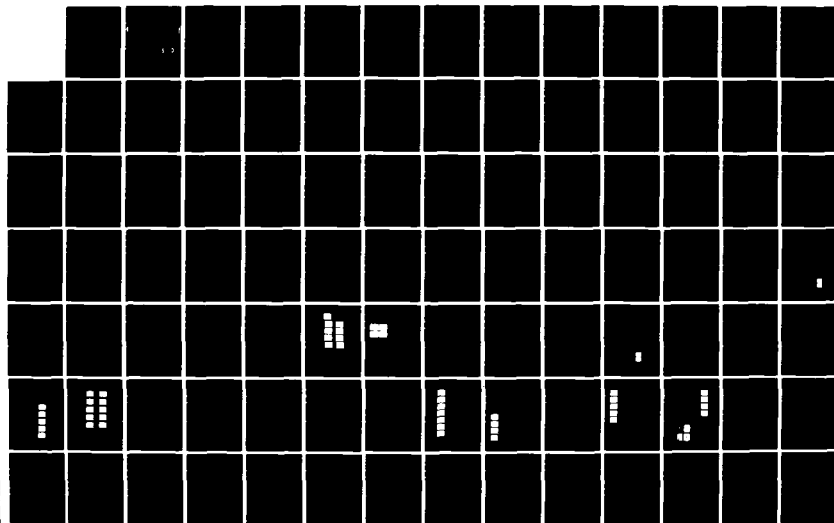
CONTINUOUSLY TUNABLE OPTICALLY PUMPED HIGH-PRESSURE DF  
YIELDS CO2 TRANSFER LASER(U) NORWEGIAN DEFENCE RESEARCH  
ESTABLISHMENT KJELLER K STENERSEN 25 AUG 82  
NDRE/PUBL-82/1003

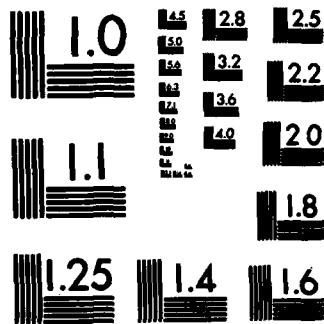
1/2

UNCLASSIFIED

F/G 20/5

NL





MICROCOPY RESOLUTION TEST CHART  
NATIONAL BUREAU OF STANDARDS-1963-A

AD A 122 131

**CONTINUOUSLY TUNABLE OPTICALLY  
PUMPED HIGH-PRESSURE DF → CO<sub>2</sub>  
TRANSFER LASER**

**BY  
KNUT STENERSEN**

**NDRE/PUBL-82/1003**

**DTIC  
ELECTE  
DEC 7 1982  
S B D**

**FORSVARETS FORSKNINGSINSTITUTT  
NORWEGIAN DEFENCE RESEARCH ESTABLISHMENT  
P O Box 25 - N-2007 Kjeller, Norway**

**DISTRIBUTION STATEMENT A**

**Approved for public release;  
Distribution Unlimited**

**8 2 12 07 052**

**DTIC FILE COPY**

1/2

**CONTINUOUSLY TUNABLE OPTICALLY PUMPED HIGH-PRESSURE  
DF→CO<sub>2</sub> TRANSFER LASER**

**by  
Knut Stenersen**

**NDRE/PUBL-82/1003**

**FORSVARETS FORSKNING SINSTITUTT  
NORWEGIAN DEFENCE RESEARCH ESTABLISHMENT  
P O Box 25 - N-2007 Kjeller, Norway**

**August 1982**


3/4

NORWEGIAN DEFENCE RESEARCH ESTABLISHMENT (NDRE)  
 FORSVARETS FORSKNINGINSTITUTT (FFI)  
 POST OFFICE BOX 25  
 N-2007 KJELLER, NORWAY

UNCLASSIFIED

SECURITY CLASSIFICATION OF THIS PAGE  
 (when data entered)

## REPORT DOCUMENTATION PAGE

1) PUBL/REPORT NUMBER NDRE/PUBL-82/1003 1a) JOB REFERENCE FFI/E/415	2) SECURITY CLASSIFICATION UNCLASSIFIED 2a) DECLASSIFICATION/DOWNGRADING SCHEDULE -	3) NUMBER OF PAGES 105												
4) TITLE CONTINUOUSLY TUNABLE OPTICALLY PUMPED HIGH-PRESSURE DF→CO <sub>2</sub> TRANSFER LASER														
5) NAMES OF AUTHOR(S) IN FULL (surname first) STENERSEN Knut														
6) DISTRIBUTION STATEMENT Approved for public release. Distribution unlimited (Offentlig tilgjengelig)														
7) INDEXING TERMS <table border="0"> <tr> <td>IN ENGLISH:</td> <td>IN NORWEGIAN</td> </tr> <tr> <td>a) <u>Lasers</u></td> <td>a) <u>Lasere</u></td> </tr> <tr> <td>b) <u>Infrared Lasers</u></td> <td>b) <u>Infrarøde lasere</u></td> </tr> <tr> <td>c) <u>Carbon Dioxide Lasers</u></td> <td>c) <u>Karbondioksyd lasere</u></td> </tr> <tr> <td>d) <u>Optical Pumping</u></td> <td>d) <u>Optisk pumping</u></td> </tr> <tr> <td>e) <u>Tuning</u></td> <td>e) <u>Avstemming</u></td> </tr> </table> THESAURUS REFERENCE: NASA Thesaurus			IN ENGLISH:	IN NORWEGIAN	a) <u>Lasers</u>	a) <u>Lasere</u>	b) <u>Infrared Lasers</u>	b) <u>Infrarøde lasere</u>	c) <u>Carbon Dioxide Lasers</u>	c) <u>Karbondioksyd lasere</u>	d) <u>Optical Pumping</u>	d) <u>Optisk pumping</u>	e) <u>Tuning</u>	e) <u>Avstemming</u>
IN ENGLISH:	IN NORWEGIAN													
a) <u>Lasers</u>	a) <u>Lasere</u>													
b) <u>Infrared Lasers</u>	b) <u>Infrarøde lasere</u>													
c) <u>Carbon Dioxide Lasers</u>	c) <u>Karbondioksyd lasere</u>													
d) <u>Optical Pumping</u>	d) <u>Optisk pumping</u>													
e) <u>Tuning</u>	e) <u>Avstemming</u>													
8) ABSTRACT (continue on reverse side if necessary) <p>The possibility of operating a continuously tunable high-pressure CO<sub>2</sub> laser by exciting the gas optically with radiation from a pulsed DF laser is studied experimentally and theoretically. The pumping radiation is absorbed by DF in a high-pressure DF/CO<sub>2</sub>/He mixture, and subsequent vibrational energy transfer to the CO<sub>2</sub> ν<sub>3</sub> mode provides the CO<sub>2</sub> laser population inversion. Continuous tuning of the CO<sub>2</sub> laser frequency between two CO<sub>2</sub> line centres in the R-branch at 10.26 μm is demonstrated at 12 atm laser gas pressure. The operational characteristics of the laser are studied for several gas mixtures at gas pressures up to 19 atm. For a 10 atm gas mixture containing 0.6% DF, 5% CO<sub>2</sub> and 94.4% He the maximum CO<sub>2</sub> laser output energy obtained with a two-mirror CO<sub>2</sub> laser resonator is approximately 6 mJ, corresponding to a total quantum efficiency of 20%. The slope quantum efficiency is then about 35%. The choice of gas mixture is not critical for the laser performance. A maximum output energy of 1 mJ is obtained in the frequency tuning experiments. A theoretical laser model is outlined, and the results of computer simulations based on this model are in reasonable agreement with the experimental results.</p>														
9) DATE 25 August 1982	AUTHORIZED BY  Finn Lied	POSITION Director												

UNCLASSIFIED

SECURITY CLASSIFICATION OF THIS PAGE  
 (when data entered)

## CONTENTS

	Page
<b>1 INTRODUCTION</b>	<b>7</b>
<b>2 OPTICAL PUMPING AND THE DF→CO<sub>2</sub> TRANSFER LASER CONCEPT</b>	<b>11</b>
2.1 The optical excitation technique	11
2.1.1 Optical excitation schemes	11
2.1.2 Optical pumping geometries	12
2.2 The DF→CO <sub>2</sub> transfer laser concept	14
<b>3 THEORY OF THE OPTICALLY PUMPED HIGH-PRESSURE DF→CO<sub>2</sub> TRANSFER LASER</b>	<b>18</b>
3.1 High-pressure CO <sub>2</sub> gas as an amplifying laser medium	18
3.1.1 Energy levels and regular laser transitions of the CO <sub>2</sub> molecule	19
3.1.2 Sequence bands and hot bands	21
3.1.3 Population distributions and the four-temperature model	23
3.1.4 CO <sub>2</sub> laser gain	25
3.1.5 High-pressure CO <sub>2</sub> laser gain	27
3.2 Theory of the optically pumped DF→CO <sub>2</sub> transfer laser	29
3.2.1 The DF pumping laser	29
3.2.2 Extension of the four temperature model	31
3.2.3 The pumping process	32
3.2.4 Energy transfer from DF to CO <sub>2</sub>	36
3.2.5 Energy relaxation processes	38
3.2.6 The influence of a time-dependent translational/rotational temperature	41
3.2.7 Time evolution of the laser intensity	44
3.3 Summary of the laser model	44
<b>4 COMPUTER SIMULATIONS OF THE LASER</b>	<b>47</b>
<b>5 DESCRIPTION OF THE EXPERIMENTS</b>	<b>54</b>
5.1 Configurations of the laser experiments	55
5.2 The DF pumping laser	58
5.2.1 Multiline DF laser operation	59
5.2.2 Single-line DF laser operation	60
5.3 Matching between the pumping beam and the TEM <sub>00</sub> resonator mode of the DF→CO <sub>2</sub> transfer laser	62
5.3.1 Mode matching in multiline pumping	63
5.3.2 Mode matching in single-line pumping	64
5.4 Radiation damage at mirrors and Brewster windows	64
5.5 Preparation of gas mixtures	64
5.6 CO <sub>2</sub> laser gain measurements	66

		Page
5.7	Frequency tuning experiments	67
6	EXPERIMENTAL RESULTS	70
6.1	Results of gain measurements	70
6.2	Results of laser experiments performed with the two-mirror CO <sub>2</sub> laser resonator	72
6.2.1	Multiline pumping	73
6.2.2	Single-line pumping	75
6.2.3	Output energies and quantum efficiencies	82
6.3	Results of frequency tuning experiments	84
7	CONCLUSIONS	87
Appendix		
A	Unit conversion scales	90
B	List of symbols	91
C	Energy transfer between harmonic oscillator vibrational modes	93
D	Constants and parameter values used in the computer calculations	94
E	Spectral characteristics of optical components	96
F	The choice of materials in the gas handling system; Gas mixing procedures	97
G	Impurities in the DF gas	101
	References	102

Accession For	
NTIS GRA&I	<input checked="" type="checkbox"/>
DTIC TAB	<input type="checkbox"/>
Unannounced	<input type="checkbox"/>
Justification	
By	
Distribution/	
Availability Codes	
Dist	Avail and/or Special
A	



## CONTINUOUSLY TUNABLE OPTICALLY PUMPED HIGH-PRESSURE DF $\rightarrow$ CO<sub>2</sub> TRANSFER LASER

### SUMMARY

The possibility of operating a continuously tunable high-pressure CO<sub>2</sub> laser by exciting the gas optically with radiation from a pulsed DF laser is studied experimentally and theoretically. The pumping radiation is absorbed by DF in a high-pressure DF/CO<sub>2</sub>/He mixture, and subsequent vibrational energy transfer to the CO<sub>2</sub>  $\nu_3$  mode provides the CO<sub>2</sub> laser population inversion. Continuous tuning of the CO<sub>2</sub> laser frequency between two CO<sub>2</sub> line centres in the R-branch at 10.26  $\mu\text{m}$  is demonstrated at 12 atm laser gas pressure. The operational characteristics of the laser are studied for several gas mixtures at gas pressures up to 19 atm. For a 10 atm gas mixture containing 0.6% DF, 5% CO<sub>2</sub> and 94.4% He the maximum CO<sub>2</sub> laser output energy obtained with a two-mirror CO<sub>2</sub> laser resonator is approximately 6 mJ, corresponding to a total quantum efficiency of 20%. The slope quantum efficiency is then about 35%. The choice of gas mixture is not critical for the laser performance. A maximum output energy of 1 mJ is obtained in the frequency tuning experiments. A theoretical laser model is outlined, and the results of computer simulations based on this model are in reasonable agreement with the experimental results.

### 1 INTRODUCTION

Since laser action was observed for the first time in a Ruby crystal in 1960, new active laser media and new excitation techniques have been intensively studied, and today laser radiation can be generated at practically any wavelength from the vacuum ultraviolet to the far infrared part of the spectrum.

The most outstanding properties of laser radiation are its extremely narrow spectral bandwidth, high degree of directionality and coherence in space and time. The radiation can be continuous-wave or pulsed with pulse lengths as short as fractions of a picosecond and peak powers up to hundreds of terawatts. These unique features have caused a revolution in research areas like high resolution spectroscopy (1), photochemistry (2) and the study of ultrafast phenomena in atoms and molecules (3), and they have given rise to new important research fields such as laser isotope separation (4), nonlinear optics (5) and laser monitoring of pollutants and trace gases in the atmosphere (6).

Since these research areas are all based upon the analysis of interaction between radiation and matter, a common requirement usually arises about coincidence between the laser frequency and energy level spacings in the atoms or molecules under study. Serious limitations occur in many applications because it is difficult to find practical laser sources which satisfy the frequency requirements, and one often has to rely on accidental coincidences between existing laser lines and atomic or molecular energy transitions. The question has therefore naturally been raised about the possibility of continuous tuning of the laser frequency over the spectral regions of interest. Such tunable lasers are invaluable spectroscopic instruments, and the development of these sources is a great challenge to laser physicists. It is our hope to make a contribution in this field with the present work which is an investigation of a new optical excitation concept for a high-pressure carbondioxide laser.

The carbondioxide laser is one of the most powerful lasers in the infrared part of the spectrum, oscillating on a multitude of vibrational/rotational transitions in the 9–11  $\mu\text{m}$  region (7). Operated at gas pressures higher than 8–10 atm CO<sub>2</sub> lasers offer the potential of broad continuous frequency tuning since overlapping between adjacent vibrational/rotational lines then occurs due to the pressure broadening. It is the



purpose of this work to investigate the possibility of operating such a high-pressure CO<sub>2</sub> laser by exciting the gas optically with radiation from a pulsed deuterium fluoride laser.

Apart from its high efficiency, the CO<sub>2</sub> laser is particularly interesting because its wavelength range falls in the middle of the 8–14  $\mu\text{m}$  atmospheric transmission window. Many pollutants, exhaust gases and toxic gases have their absorption frequencies in this region, and remote monitoring of such species in the air is an important application for a tunable CO<sub>2</sub> laser.

Since the possibility of achieving continuous frequency tuning in high-pressure CO<sub>2</sub> lasers was first pointed out in 1971 (8), considerable effort has been put into search for suitable methods for the excitation of such lasers. So far most people have used some kind of pulsed electrical excitation of the gas, including electrical discharge excitation (9), and electron-beam sustained excitation (10). The common problem with electrical discharges is the formation of arcs in the plasma, caused by the strong electric fields that are required to sustain the plasma discharge at such high gas pressures. Electron-beam sustained excitation, on the other hand, is impractical for most purposes because of the large installations required to produce an electron-beam of sufficient power. Although continuous frequency tuning has been demonstrated in a few laboratories using these techniques, practical continuously tunable CO<sub>2</sub> lasers have not yet become available. A promising technique which has been demonstrated recently is that of using a radio-frequency discharge for excitation of a high-pressure CO<sub>2</sub> waveguide laser (11, 12). This concept may result in a more practical tunable laser than the electrical excitation techniques used so far.

As an alternative to electrical excitation, optical excitation with radiation from a high-power laser has long been recognized as a very general method for production of population inversion in various laser media. Above all, it has been used to excite molecular gas lasers for generation of coherent radiation on a large number of new wavelengths in the middle infrared and far infrared parts of the spectrum (13, 14). Optical pumping exhibits a number of important advantages compared with other excitation techniques: First of all, the excitation is inherently selective, and in principle the whole pumping energy may be effective for excitation of the laser molecules to the upper laser level. Conversion efficiencies from pumping photons to laser photons may approach 100% (15). In many cases the absorption of the pumping radiation is also very strong, resulting in extremely high pumping rates. This feature is especially important in a high-pressure laser, since the nonradiative depopulation rate of the upper laser level increases proportionally with pressure and competes seriously with the excitation. Optical pumping has created population inversion between new pairs of energy levels in molecules that would be ineffectively excited or would even dissociate in an electrical discharge. The general problems with discharge instabilities and formation of arcs which are encountered in electrical discharges are all avoided in optical pumping. Also, since negligible dissociation occurs, it is feasible to use rare and expensive molecular isotopes in sealed-off cavities, and the wavelength range of the laser may thus be extended.

Earlier investigators have demonstrated laser actions in CO<sub>2</sub> and N<sub>2</sub>O at multi-atmospheric pressures using either a pulsed HBr laser (16) or pulsed frequency doubled CO<sub>2</sub> laser radiation (17) for excitation. The laser molecules were either excited directly to the upper laser level or via energy transfer from a second molecule which absorbed the pumping radiation. The two schemes are generally referred to as direct optical pumping and optical transfer pumping. A summary of the earlier experiments is given in Table 1.1. It is observed that low output energies and quantum efficiencies have been obtained in these investigations, particularly in the case of HBr laser pumping. The potential of optical pumping as an efficient excitation method for high-pressure gas lasers was obviously not realized. Further development of optically

PUMPING SOURCE	ABSORBING MOLECULE	LASER MOLECULE	MAXIMUM GAS PRESSURE [cm <sup>2</sup> ]	MAXIMUM OUTPUT ENERGY [mJ]	PEAK OUTPUT POWER [kW]	PULSE LENGTH [ns]	QUANTUM EFFICIENCY [%]	REFERENCE
HBr LASER	-	CO <sub>2</sub>	112*	-	-	-	-	(10)
	-	CO <sub>2</sub>	33	-	1	2.2	<0.2	(10)
	-	N <sub>2</sub> O	7.5	-	-	-	-	(10)
	CO <sub>2</sub>	N <sub>2</sub> O	42	-	0.8	7-15	<1	(10)
FREQUENCY DOUBLED CO <sub>2</sub> LASER RADIATION	CO	CO <sub>2</sub>	10*	0.25	-	50	0	(17)

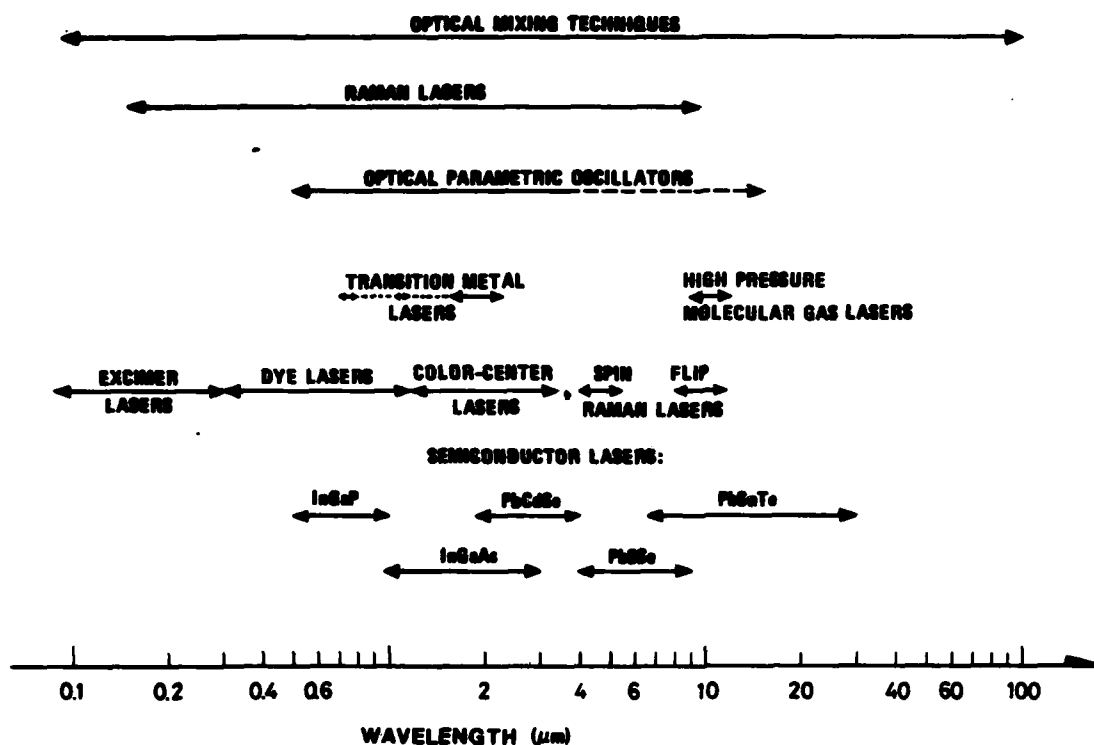
\*Denotes that He has been used as a buffer gas

Table 1.1 Summary of characteristics of optically pumped high-pressure CO<sub>2</sub> and N<sub>2</sub>O lasers

pumped high-pressure lasers into practical, continuously tunable sources has been hindered by the lack of convenient high-power pumping lasers. The HBr laser is the only powerful source with a frequency suitable for direct pumping of CO<sub>2</sub> or N<sub>2</sub>O, but so far this laser seems to be too impractical even for laboratory applications. Optical transfer pumping of CO<sub>2</sub> or N<sub>2</sub>O via CO is possible using frequency doubled CO<sub>2</sub> laser radiation. However, the frequency doubling depends on difficult crystal technology, which has hindered further development.

It is a new optical transfer pumping scheme for high-pressure CO<sub>2</sub> lasers that we investigate in this work. A pulsed DF laser oscillating on several lines in the 3.5 – 4  $\mu$ m region is used for pumping. The pumping radiation is resonantly absorbed by DF in a high-pressure DF/CO<sub>2</sub>/He mixture, and subsequent vibrational to vibrational energy transfer to the CO<sub>2</sub> upper laser level provides the population inversion. We call this a DF  $\rightarrow$  CO<sub>2</sub> transfer laser, and the concept is similar to that used in (20) for excitation of a continuous-wave low-pressure DF  $\rightarrow$  CO<sub>2</sub> transfer laser. DF lasers are powerful, highly developed and commercially available sources which may be better suited for the excitation than the sources mentioned above. It is the purpose of this work to demonstrate the principle of the optically pumped high-pressure DF  $\rightarrow$  CO<sub>2</sub> transfer laser, to investigate its operation characteristics and to evaluate its potential as a continuously tunable high-power infrared laser source.

To place this work into a greater context it is useful to look at the position of the CO<sub>2</sub> laser in relation to existing continuously tunable lasers. Several types of such sources have been developed, and their tuning ranges are indicated in Figure 1.1. The dye laser is by far the most important tunable laser in the visible region, while a number of sources are used in the infrared, including semiconductor lasers, color-center lasers, transition metal lasers, spin-flip Raman lasers, optical parametric oscillators and high-pressure molecular lasers (CO<sub>2</sub> and N<sub>2</sub>O). In addition, various frequency mixing techniques in nonlinear optical media as well as stimulated Raman scattering can be used to shift the frequency of a tunable source to other parts of the spectrum. Most of the 0.1 – 100  $\mu$ m range is covered in this way, and we notice that several sources oscillate in the same region as the CO<sub>2</sub> laser. There is not room here for a discussion of the individual sources, but a general survey with good references



Figur 1.1 Spectral ranges of tunable coherent laser sources (21, 22)

can be found in (21). It is essential to note that these sources differ considerably with respect to operating characteristics, reliability and ease of operation. Some systems are very complex, and in others the short lifetimes of the active media exclude them from practical use outside the laboratory. In general, the various sources are suited for quite different applications due to the large variations in laser parameters, such as output power, pulse energy, pulse length, mode quality, frequency bandwidth and stability. It is often impossible to find a source which combines all the required properties for a specific application, and the search for new tunable lasers is therefore important.

The  $\text{CO}_2$  laser is by far the most powerful coherent source in the 9–11  $\mu\text{m}$  region. Optical pumping provides a particularly simple and efficient excitation of the laser, and it will be shown that continuously tunable high-power  $\text{CO}_2$  laser radiation can be generated with the presented concept. Preliminary results of these investigations were published in (23). Considerable improvements in laser output energies and quantum efficiencies are reported in this work, and a more detailed theoretical model including computer simulations of the laser performance will be presented.

It should be noted that radiation frequencies, spectral line widths and molecular energies will all be given in units of ( $\text{cm}^{-1}$ ) in this text. A diagram showing the correspondence between the units ( $\text{cm}^{-1}$ ), (Hz), (J) and ( $\mu\text{m}$ ) can be found in Appendix A.

A list of symbols used in the text can be found in Appendix B.

## 2 OPTICAL PUMPING AND THE DF→CO<sub>2</sub> TRANSFER LASER CONCEPT

This chapter starts with a general survey of the most fundamental aspects of optical pumping, including pumping schemes and common pumping geometries. The second part of the chapter is an introduction to the DF→CO<sub>2</sub> transfer laser concept, which is the subject of this work. We hope that this brief discussion will facilitate the reading of the next chapters.

### 2.1 The optical excitation technique

As early as in 1960 incoherent light from pulsed flash tubes was used for optical excitation of the first Ruby lasers. Since the emission spectra from such tubes are broad, efficient excitation can only be obtained in laser media with sufficiently broad absorption profiles. Excitation with flash tubes is still successfully used for instance in solid state lasers and dye lasers.

Here we shall however restrict the discussion to the special case of optical pumping with laser radiation. The pumping power may then be concentrated within extremely narrow frequency bands, and this is therefore a far more general and efficient method for the production of population inversion in various laser media. Laser radiation is particularly efficient for excitation of gases where absorption of radiation can only take place on narrow spectral lines.

By using laser radiation it becomes possible to excite the molecules selectively to specific upper states, and this opens the possibility of achieving laser oscillation on a large number of lines that cannot be reached with other excitation techniques. The greatest success of optical pumping has perhaps been obtained in the field of far infrared lasers (14). FIR laser radiation originates from pure rotational transitions in molecules, and optical pumping provides the only efficient way of establishing population inversion between the rotational levels. Altogether optical pumping can be used for excitation of most kinds of laser media, often leading to improved laser performance such as higher output power, improved frequency stability and mode quality, higher operating pressures and broader tuning ranges. Apart from being extremely selective, optical pumping may provide extremely high excitation energy densities when the pumping radiation is focused to a small spotsize in a strongly absorbing medium. This property is of special importance in the present investigation of a high-pressure CO<sub>2</sub> laser. Since the decay rate of the upper laser level increases proportionally with pressure, high pumping energy densities are required to maintain the population inversion.

#### 2.1.1 Optical excitation schemes

In Figure 2.1 two principal energy level schemes for optical excitation of a laser molecule are illustrated. The simplest is direct optical pumping (a) in which the laser molecule is excited directly from its ground state  $g$  to the upper laser level  $u$  by radiation at frequency  $\nu_p$ . Laser oscillation at frequency  $\nu_L$  occurs to a lower level  $\ell$  which is often essentially unpopulated at room temperature. The other possibility is the optical transfer pumping scheme (b) where a mixture of two different molecules is used. The first molecule only acts as an absorber for the pumping radiation, and it is excited to a transfer level  $t$ . Via collisions between the two molecules the energy is transferred to the upper laser level  $u$ , and population inversion with respect to the level  $\ell$  is thereby established. The most important advantage of optical transfer pumping is that it relaxes the requirement of exact matching between the pumping laser frequency and the absorption frequency of the laser molecule. It is even possible to use the same combination of a powerful pumping laser and an absorbing molecule for optical transfer pumping of several different laser molecules or isotopes (17).

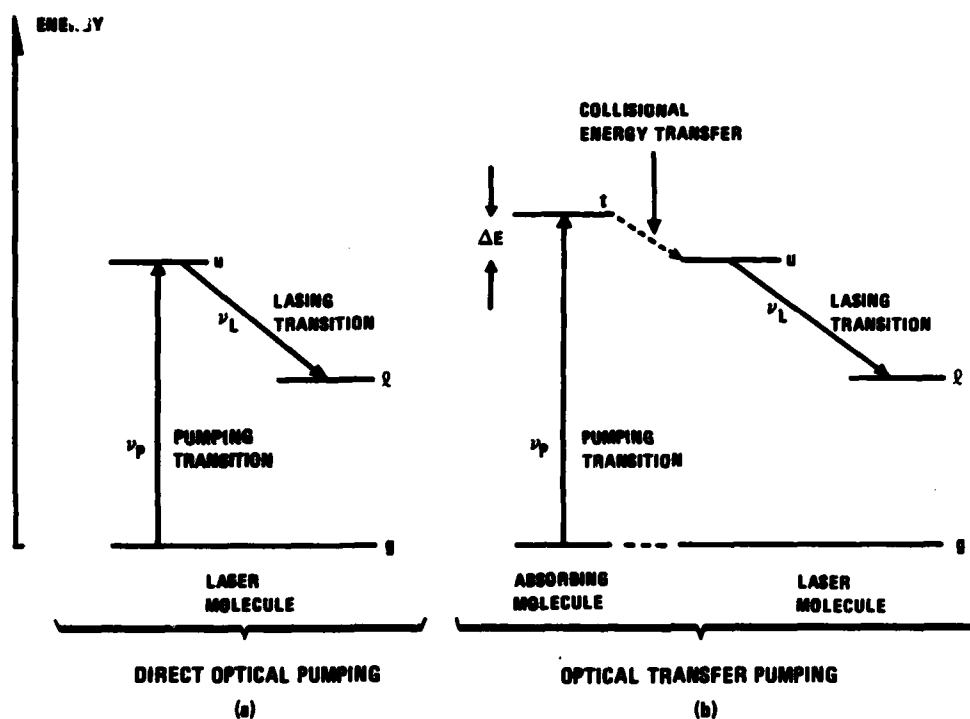


Figure 2.1 Optical excitation schemes

$\nu_p$  — pumping radiation frequency  
 $\nu_L$  — laser radiation frequency

It is the optical transfer pumping scheme that we use in this work, and we shall make some general comments on the transfer process, which is naturally critical for the laser performance. First, it should be remarked that the energy transfer may be very fast even with energy differences  $\Delta E$  of several hundred  $\text{cm}^{-1}$  between the levels  $t$  and  $u$ . The transfer speed is proportional to the partial pressure of the laser gas and may thus be varied. In a favourable situation the energy transfer is much faster than the decay from the two levels. A positive energy difference ( $\Delta E = E_t - E_u > 0$ ) favours population of the  $u$ -level, and an almost complete energy transfer may then occur. This is important with respect to laser gain.

In general the picture is much more complicated than indicated in Figure 2.1, mainly because a large number of energy levels become involved via relaxation processes. In the case of an infrared molecular gas laser the levels shown in Figure 2.1 are actually rotational sublevels within different vibrational states, and fast relaxations induced by collisions occur within the rotational sublevel manifolds as well as among the vibrational levels. A discussion of laser excitation can therefore not be made without considering these relaxations. We shall see in later chapters that the choice of gas mixture is especially important for an optimization of these processes with respect to laser gain and output power.

### 2.1.2 Optical pumping geometries

We shall now consider two principal geometries which can be used in optical pumping. Figure 2.2 shows schematics of the longitudinal (a) and the transverse (b) pumping geometries. The discussion will be concentrated on longitudinal optical pumping,

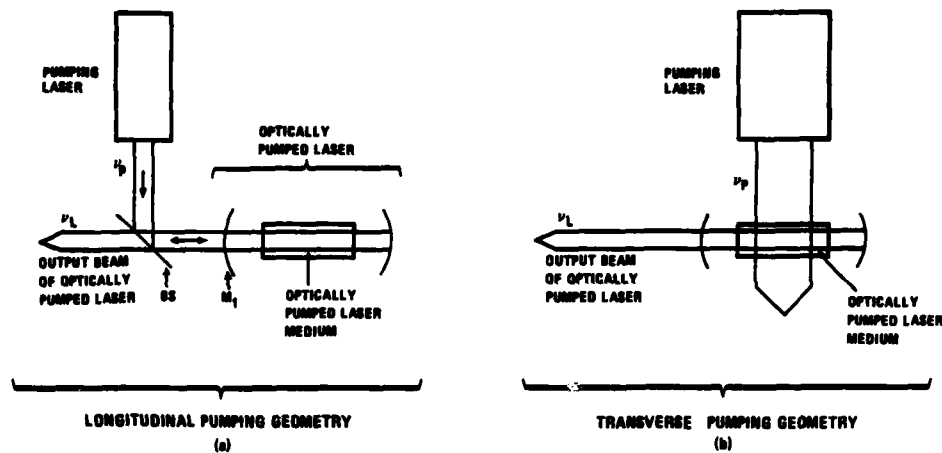


Figure 2.2 Optical pumping geometries

- $\nu_p$  — pumping radiation frequency
- $\nu_L$  — frequency of the radiation from the optically pumped laser
- BS — beamsplitter
- $M_1$  — input mirror at  $\nu_p$  and output coupler at  $\nu_L$

since that geometry is used in this work. The abbreviation OPL is frequently used for "optically pumped laser" in this section.

In the longitudinal pumping geometry the pumping radiation is introduced along the OPL resonator axis. Special spectral characteristics are then required at the beamsplitter (BS) and input mirror ( $M_1$ ). Ideally, the beamsplitter should reflect 100% at  $\nu_p$  and transmit 100% at  $\nu_L$  while the input mirror should transmit 100% at  $\nu_p$  and provide a suitable output coupling at  $\nu_L$ . Such an optimization at two frequencies is not trivial and some reflection or transmission losses must usually be allowed for.

An important consideration is that of spatial matching between the pumping laser beam and the OPL  $TEM_{00}$  resonator mode. To obtain high conversion efficiency and laser beam quality close matching is required. The ideal pumping beam in most situations is a  $TEM_{00}$  fundamental Gaussian beam, but from the theory of Gaussian beams (24) we know that a perfect overlapping with the OPL  $TEM_{00}$  mode is never possible, because  $\nu_p$  and  $\nu_L$  are different frequencies. However, with a suitable focusing of pumping beam and choice of mirror radii in the OPL resonator, it is possible to achieve a reasonable matching in most cases. The problems usually arise when the pumping beam is a multimode rather than a fundamental Gaussian beam. This may lead to excitation of higher-order transverse OPL resonator modes, reducing the spectral purity of the OPL radiation.

The longitudinal pumping geometry is generally applicable, offering the advantage that the OPL cavity length can be adjusted according to the absorption distance of the pumping radiation. There is, however, one fundamental limitation determined by the maximum pumping power or energy densities that are tolerated on mirrors and windows before radiation damage occurs. When the beam from a high power laser is focused to a small spot on the OPL input mirror, the damage threshold is easily exceeded, and this will be a major concern in the present work.

The latter problem is significantly reduced in the transverse pumping geometry shown in Figure 2.2b, with the pumping radiation coming in perpendicular to the OPL resonator axis. The radiation is usually focused onto the axis by a cylinder lens, and the resulting pumping power density on the optical surfaces is generally lower than in the longitudinal pumping geometry. This approach is also simpler because the special spectral characteristics of the beamsplitter and input mirror are no longer needed. The matching between the excited gas volume and the OPL resonator mode may seem to be a problem, but by using an optical waveguide instead of an open OPL resonator, laser oscillation on a single transverse waveguide mode can be obtained. Efficient use of the transverse pumping geometry normally requires that the pumping radiation is absorbed over a distance comparable to the width of the OPL resonator mode. In the present work the absorption distance was substantially longer and a longitudinal pumping geometry was consequently chosen.

## 2.2 The DF→CO<sub>2</sub> transfer laser concept

We shall now turn to a discussion of the particular laser concept that is studied in this work and point out some of its most fundamental features. As explained in the introduction, the purpose is to investigate the possibility of operating an optically excited high-pressure carbondioxide laser, and to evaluate its potential as a continuously tunable laser source. The theory of the CO<sub>2</sub> molecule as an amplifying laser medium will be treated in section 3.1, but at this point it suffices to know that CO<sub>2</sub> lasers exhibit gain on a multitude of vibrational/rotational transitions in the 900–1100 cm<sup>-1</sup> (9–11 μm) region. Conventional CO<sub>2</sub> lasers are operated at gas pressures lower than or equal to one atmosphere, and a typical gain spectrum of a 1 atm CO<sub>2</sub> laser is given by the lower curve of Figure 2.3. We observe that laser oscillation can occur only on discrete lines, and the widths of these lines are typically 10% of the interline spacings. The linewidths increase proportionally with the gas pressure due to collision broadening, and in a 10 atm CO<sub>2</sub> laser the gain spectrum will look like the upper curve in Figure 2.3. Complete overlapping between adjacent vibrational/rotational lines provides a continuous gain profile and the possibility of continuous tuning of the laser frequency is obvious. The notations P-branch and R-branch will be explained in chapter 3.

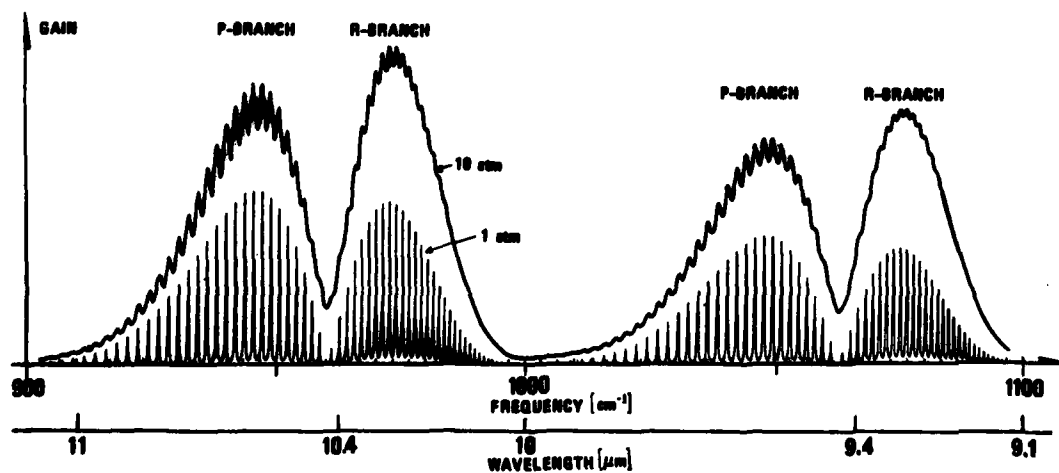


Figure 2.3 CO<sub>2</sub> laser gain spectra (after 25)  
 Lower curve — 1 atm gas pressure  
 Upper curve — 10 atm gas pressure

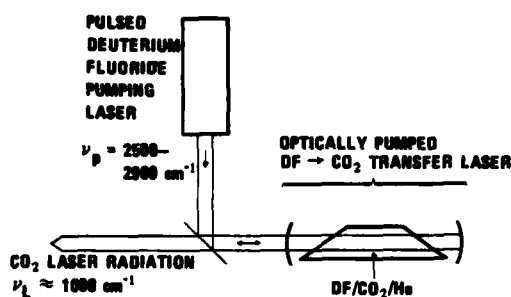


Figure 2.4 Schematic of experimental set-up used for optical pumping of the  $DF \rightarrow CO_2$  transfer laser

A schematic of our experimental arrangement is shown in Figure 2.4, and the longitudinal pumping geometry of Figure 2.2a is recognized. The pumping source is a pulsed deuterium fluoride laser which oscillates on several lines in the  $2500\text{--}2900\text{ cm}^{-1}$  ( $3.5\text{--}4\text{ }\mu\text{m}$ ) region. The radiation is absorbed by DF in a high-pressure  $DF/CO_2/He$  mixture, with subsequent collisional energy transfer from DF to the  $CO_2$  upper laser level. A further discussion about details in the set-up is given in chapter 5.

Our intention is here to give a brief survey of the sequence of processes that are important in the conversion from DF laser pumping photons to

$CO_2$  laser photons. If this picture is kept in mind it should facilitate the reading of the next chapters.

The energy level diagrams of the DF pumping laser and the optically pumped  $DF \rightarrow CO_2$  transfer laser are shown in Figure 2.5. Notice that the vibrational levels are marked with heavy lines, while thin lines indicate rotational sublevels. We shall briefly consider the transitions of the DF laser molecule (Figure 2.5a). Since DF is a two-atomic molecule, it has a single vibrational frequency, and the vibrational levels are marked with quantum numbers  $v = 0, 1, 2, 3 \dots$ . Rotational sublevels with quantum numbers  $J$  and  $J-1$  are also indicated. DF laser oscillation may occur on 25–30 vibrational/rotational transitions, three of which are shown in the figure. These are lines within the  $v = 1 \rightarrow v = 0$ ,  $v = 2 \rightarrow v = 1$  and  $v = 3 \rightarrow v = 2$  vibrational bands, and we shall briefly refer to them as the  $1 \rightarrow 0$ ,  $2 \rightarrow 1$  and  $3 \rightarrow 2$  lines. Depending on the chosen DF laser resonator configuration it is possible to obtain laser oscillation on all these lines simultaneously or on a single line only.

Figure 2.5b shows the relevant energy levels of the  $DF \rightarrow CO_2$  transfer laser, and the principal excitation scheme of Figure 2.1b is recognized. The levels of the DF absorbing molecule are identical to those of Figure 2.5a, while the  $CO_2$  energy level diagram is somewhat more complex. A three-atomic linear molecule like  $CO_2$  has four normal vibrational modes but only three characteristic vibrational frequencies  $\nu_1$ ,  $\nu_2$  and  $\nu_3$ , since the  $\nu_2$ -mode is doubly degenerate. The two first excited vibrational levels of each mode are shown in the figure, and two possible  $CO_2$  laser transitions are also indicated (see chapter 3 for further details).

In the description of the sequence of processes that occur in the laser, it is useful to start with the excitation. One solid and two dashed arrows indicate that the excitation involves just the same transitions in the DF absorbing molecule as those of the DF laser molecule. There is thus an inherent matching between pumping laser frequencies and the absorption frequencies. This is a unique and favourable feature of this laser system. Since practically all the DF molecules are in the vibrational ground state at room temperature, the excitation process can only be initiated by the  $1 \rightarrow 0$  DF laser pumping lines, as indicated by the solid arrow. If a single pumping line is used, this must therefore be one of the  $1 \rightarrow 0$  lines. On the other hand, using a multiline DF laser, the  $2 \rightarrow 1$  and  $3 \rightarrow 2$  lines may also contribute to the excitation as the DF molecules are excited step by step up their vibrational energy ladder. This is indicated by the dashed arrows. An important part of this process is the internal vibrational relaxation which tends to establish a Boltzmann distribution over the DF



vibrational levels. We shall in fact assume in chapter 3 that Boltzmann distributions with characteristic vibrational temperatures are always maintained within each of the four vibrational energy ladders in DF and CO<sub>2</sub>.

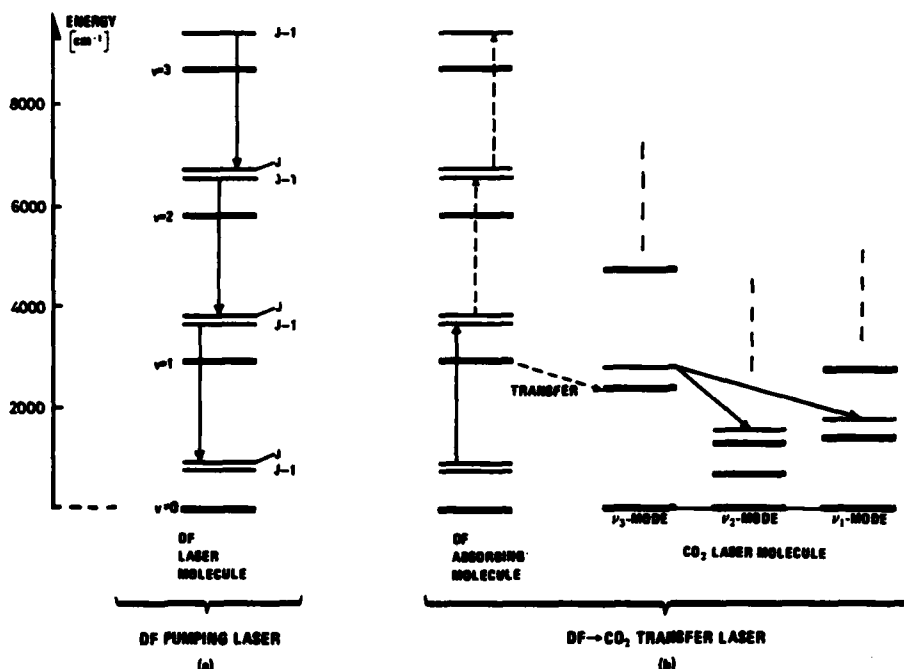


Figure 2.5 Energy level diagrams of the DF pumping laser (a) of the DF  $\rightarrow$  CO<sub>2</sub> transfer laser (b)

Heavy lines — vibrational levels

Thin lines — rotational levels

Laser transitions, pumping transitions and energy transfer are indicated by arrows (see text)

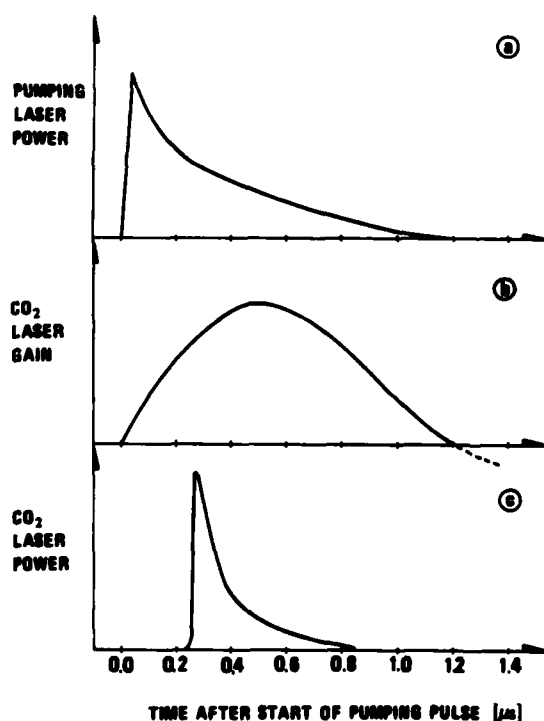
It is indicated in the figure that the energy transfer from DF to CO<sub>2</sub> takes place between the first excited vibrational levels of DF and of the CO<sub>2</sub>  $\nu_3$  mode. A more correct picture, which we shall adapt in chapter 3, is to consider the process as energy transfer between the two vibrational energy ladders. A favourable condition is the fact that the DF vibrational energy quantum is about 550 cm<sup>-1</sup> larger than the CO<sub>2</sub>  $\nu_3$  quantum, which means that almost complete energy transfer to the  $\nu_3$  mode can be obtained (26).

Along with the energy transfer a population inversion is established between the first  $\nu_3$  vibrational level and two lower lying  $\nu_1$  and  $\nu_2$  levels which are essentially unpopulated at room temperature. CO<sub>2</sub> laser oscillation may then occur on a multitude of vibrational/rotational transitions. These are the regular CO<sub>2</sub> laser lines, but we shall see in section 3.1 that the so-called sequence band transitions originating from higher  $\nu_3$  vibrational levels may also play an important role, especially in a high-pressure CO<sub>2</sub> laser where they overlap with the regular laser transitions.

Relaxations from vibrational to translational/rotational energy (V-T/R processes) and exchange of vibrational energy among the CO<sub>2</sub> vibrational modes (V-V processes) are important because they determine whether the population inversion can be maintained. It is intuitively understood that V-T/R processes in DF and in the CO<sub>2</sub>  $\nu_3$  mode as well as V-V transfer from the  $\nu_3$  mode to the  $\nu_1$  and  $\nu_2$  modes are detri-

mental to CO<sub>2</sub> laser gain, while V-T/R relaxation of the  $\nu_1$  and  $\nu_2$  modes should be fast to avoid a bottle-neck and population build-up in the lower laser levels.

We shall now briefly consider how the choice of gas mixture will influence the different processes. The DF partial pressure should obviously be high enough to ensure a reasonable absorption of the pumping radiation. Unfortunately DF is also a serious deactivator for the CO<sub>2</sub>  $\nu_3$  mode, and a compromise has to be made to avoid a too rapid decay of the upper laser level. The amount of CO<sub>2</sub> is primarily important for the energy transfer rate from DF to the CO<sub>2</sub>  $\nu_3$  mode, and already at a CO<sub>2</sub> partial pressure of 0.5 atm this rate is much larger than the decay rate of the  $\nu_3$  mode. To increase the total gas pressure further, it is favourable to use He instead of CO<sub>2</sub>. One reason is that He provides slower decay of the CO<sub>2</sub>  $\nu_3$  mode and faster decay of the  $\nu_1$  and  $\nu_2$  modes than CO<sub>2</sub> does itself. Equally important is the fact that the DF absorption lines are about ten times less broadened by He collisions than by CO<sub>2</sub> collisions, which means that a much stronger absorption of the pumping radiation can be maintained at high total gas pressures. Nevertheless, the broadening of the absorption lines is responsible for increasing the absorption lengths from a few millimeters to several centimeters and this is the reason why a longitudinal pumping geometry was chosen in this work. These aspects will all be discussed in further detail in chapter 3, and we shall only mention here that a typical 10 atm DF/CO<sub>2</sub>/He mixture used in the experiments contains 0.5% DF, 4.5% CO<sub>2</sub> and 95% He.



We end this chapter by giving some typical examples of results that have been obtained in this work. Figure 2.6 shows the relative time evolutions of the DF pumping laser pulse (a), the CO<sub>2</sub> laser small signal gain (b) and the CO<sub>2</sub> laser pulse (c) for a 10 atm laser gas mixture. The CO<sub>2</sub> laser oscillation builds up in a period of about 250 ns, and due to the high gain at the end of this period, the integrated excitation energy in the CO<sub>2</sub>  $\nu_3$  mode is extracted in a short and intensive laser pulse. This phenomenon is called gain-switching. The pulse energy is about 4 mJ which corresponds to a quantum efficiency of 15% measured relative to the number of absorbed pumping photons. The peculiar undershoot in the measured small signal gain requires a closer explanation which will be given later.

**Figure 2.6** Typical time evolution of the DF pumping laser power (a), the CO<sub>2</sub> laser small signal gain (b) and the CO<sub>2</sub> laser power (c). The undershoot in the small signal gain will be explained in chapters 5 and 6 (arbitrary ordinate units)

### 3 THEORY OF THE OPTICALLY PUMPED HIGH-PRESSURE DF $\rightarrow$ CO<sub>2</sub> TRANSFER LASER

The purpose of this chapter is to present a theoretical model which can describe the time evolution of the gain and the laser radiation intensity of the optically pumped high-pressure DF $\rightarrow$ CO<sub>2</sub> transfer laser. This model has been used in computer simulations of the laser characteristics, and the results of such simulations are presented in chapter 4.

While considerable effort has been put into the theoretical modelling of electrically excited CO<sub>2</sub> lasers (27), very few theoretical investigations of optically pumped CO<sub>2</sub> lasers have been reported in the literature. The only theoretical investigation with relevance to our work has been made by Stepanov and coworkers (28), who presented a simplified model of an optically pumped transfer laser. The CO<sub>2</sub> $\rightarrow$ N<sub>2</sub>O transfer laser system was chosen as an example in the calculations, with relevance to an earlier experimental investigation of a high-pressure CO<sub>2</sub> $\rightarrow$ N<sub>2</sub>O transfer laser pumped by a pulsed HBr laser (19). (The latter work was also referred to in chapter 1). Results were presented for the spatial distribution of the laser gain, but no calculations were made of the time evolution of the laser intensity, and a precise comparison with the experimental results of (19) was therefore not possible. Instantaneous energy exchange between the  $\nu_3$  modes of CO<sub>2</sub> and N<sub>2</sub>O was assumed in the model, and several energy relaxation processes were ignored which reduced the validity of the results.

We find that several extensions of the model are required for a correct description of our laser system. Particularly, since it is a high-pressure laser, we have to account for the effects of line overlapping and the contribution to the laser gain from the so-called sequence band transitions (29). These effects were not taken into account in Stepanov's model, but we shall see that they may become very important in a high-pressure CO<sub>2</sub> laser.

To our knowledge the present work is the first where the results of a reasonably comprehensive theoretical model are compared with experimental results for an optically pumped high-pressure CO<sub>2</sub> laser. It has not been possible within the frame of this work to take into account all the effects that are discussed in this chapter in the computer calculations of chapter 4, but effects that are ignored will be discussed as sources of error in the computed results.

Section 3.1 treats the general theory of the amplification of radiation in a high-pressure CO<sub>2</sub> laser, while the special theory of the optically pumped DF $\rightarrow$ CO<sub>2</sub> transfer laser is outlined in section 3.2. The theoretical model with its basic assumptions and simplifications is summarized in section 3.3.

#### 3.1 High-pressure CO<sub>2</sub> gas as an amplifying laser medium

Throughout this text we shall ignore the electronic energy of the molecules, since they will always remain in their electronic ground states. Being a three-particle system, the CO<sub>2</sub> molecule then has nine degrees of freedom. Since CO<sub>2</sub> is also a linear molecule, the motion of the centre of gravity (translation) and the orientation of the molecular axis (rotation) can be specified in terms of five degrees of freedom, leaving the vibrational motion to be described in terms of four normal vibrational modes. The part of the molecular energy that we shall be concerned with is thus split into translational, rotational and vibrational energy. We shall see that the transport of energy among the various degrees of freedom plays an important role in the CO<sub>2</sub> laser gas.

### 3.1.1 Energy levels and regular laser transitions of the CO<sub>2</sub> molecule

A general theory of energy levels and infrared transitions in polyatomic molecules including CO<sub>2</sub> can be found in (30). The four normal modes of vibration of the CO<sub>2</sub> molecule are illustrated in Figure 3.1a. They are the symmetric and asymmetric stretching modes and the two degenerate bending modes, describing bending motions in two perpendicular planes. The respective characteristic vibrational frequencies are called  $\nu_1$ ,  $\nu_3$  and  $\nu_2$ , and the corresponding vibrational energy diagram is shown in Figure 3.1b. (The two bending modes are usually treated as one doubly degenerate mode with characteristic frequency  $\nu_2$ .) The energies of the vibrational levels of mode number  $i$  are approximately given by the harmonic oscillator expression

$$E_i = h\nu_i \left( v_i + \frac{1}{2} \right) \quad (3.1)$$

where

$v_i$  – vibrational quantum number

Due to anharmonicity and coupling between the modes, the energy levels are not exactly equidistant, and small terms may be added in equation (3.1) to account for this. Consequences of such effects will be discussed later.

Only single mode vibrational levels as expressed by equation (3.1) are shown in Figure 3.1b, but a molecule can generally be excited to levels which are superpositions of levels of the three modes. The general vibrational state is denoted by  $(v_1 v_2^l v_3)$ , where  $l$  is an additional quantum number for the doubly degenerate  $\nu_2$  mode, representing the vibrational angular momentum about the molecular axis.  $l$  can take the values  $v_2, v_2-2, v_2-4, \dots, 1$  or 0, and since each level with  $l \neq 0$  is doubly degenerate, there are altogether  $v_2 + 1$  levels belonging to the same  $v_2$ . These levels

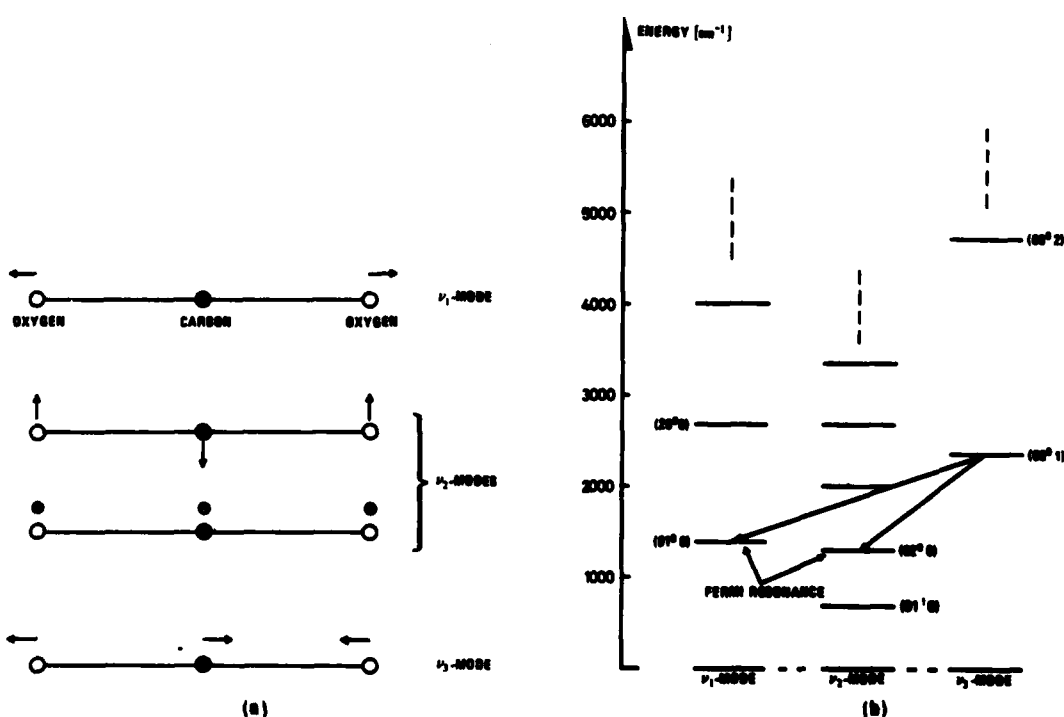


Figure 3.1 The normal modes of vibration of the CO<sub>2</sub> molecule (a) and the corresponding vibrational energy diagram (b)  
The two bending modes are treated as one doubly degenerate mode with characteristic frequency  $\nu_2$

are split due to anharmonicity and perturbations, but in the calculations of populations and partition functions in section 3.1.3, we shall make the approximation that the levels are degenerate.

The two vibrational transitions involved in conventional low-pressure CO<sub>2</sub> lasers are also shown in Figure 3.1b. They both originate from the (00<sup>0</sup>1) upper laser level, and they are called the regular CO<sub>2</sub> laser transitions. The respective frequencies are 961 cm<sup>-1</sup> and 1064 cm<sup>-1</sup> corresponding to 10.4 μm and 9.4 μm wavelengths. It is important to notice that the two lower levels are not pure vibrational levels of the ν<sub>1</sub> and ν<sub>2</sub> modes. The pure (10<sup>0</sup>0) and (02<sup>0</sup>0) levels are accidentally degenerate, differing in energy by only 3 cm<sup>-1</sup>, and interaction between the pure states leads to perturbation of the energy levels. This interaction is usually called Fermi resonance, and the resulting pair of energy levels differ in energy by about 103 cm<sup>-1</sup>. Since the resulting states are mixtures of the two pure states, it is no longer correct to denote them by (10<sup>0</sup>0) and (02<sup>0</sup>0), but for simplicity we shall use this notation also in the following text. A more correct notation which may be found in other texts is (10<sup>0</sup>0, 02<sup>0</sup>0)<sub>I</sub> and (10<sup>0</sup>0, 02<sup>0</sup>0)<sub>II</sub> where I is used for the highest of the two levels. Generally the Fermi resonance occurs within all sets of accidentally degenerate levels of the type

$$(v_1 v_2' v_3), ((v_1-1)(v_2+2)' v_3), ((v_1-2)(v_2+4)' v_3), \dots$$

and some of these are important in high-pressure CO<sub>2</sub> lasers as discussed in sections 3.1.2 and 3.1.5.

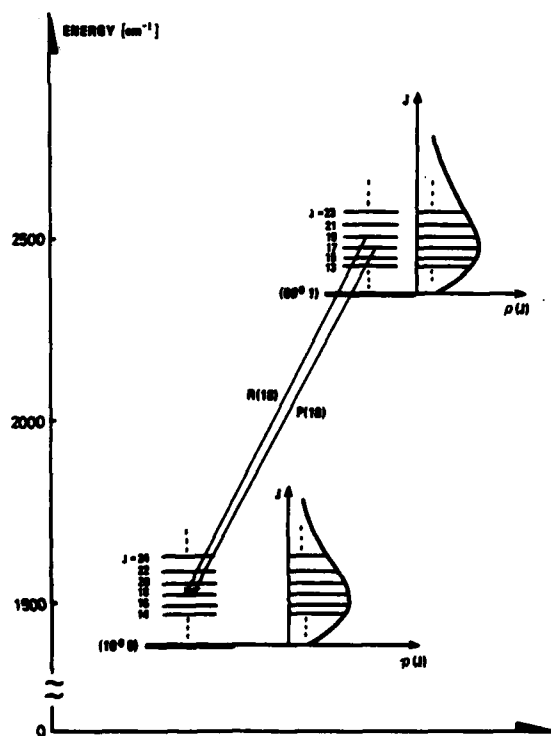


Figure 3.2 Rotational sublevel manifolds of the (00<sup>0</sup>1) and (10<sup>0</sup>0) CO<sub>2</sub> vibrational levels

$\rho(J)$  is the population probability of the rotational sublevels. Two CO<sub>2</sub> laser transitions, P(18) and R(18), are shown.

Each of the vibrational levels is split into a multitude of rotational sublevels, and the rotational energy can be written as

$$E_J = B \cdot J(J+1) - D \cdot J^2 \cdot (J+1)^2 + \dots \quad (3.2)$$

where

$J$  — rotational quantum number

$B$  — rotational constant

$D$  — centrifugal distortion constant

The second term comes in because the molecule is not a perfectly rigid quantum mechanical rotator. Closer examination also shows that  $B$  and  $D$  both depend on the vibrational state of the molecule, which is a result of coupling between rotation and vibration. Figure 3.2 shows the rotational sublevel structure of the (00<sup>0</sup>1) and (10<sup>0</sup>0) vibrational levels, and the population distribution  $\rho(J)$  in the rotational manifold is also indicated. A further discussion of the populations of the various states is made in section 3.1.3.

In the standard isotope  $^{12}\text{C}^{16}\text{O}_2$  alternate rotational levels are missing in the upper and lower vibrational laser levels. This is the case for linear molecules with a centre of symmetry and zero nuclear spin in atoms outside the symmetry centre (30), and the situation is different for some of the other  $\text{CO}_2$  isotopes. We have only used the standard isotope in this work, but use of other isotopes will be an interesting extension of the experiments since overlapping between adjacent  $\text{CO}_2$  laser lines occurs at lower gas pressure in isotopes where all rotational levels are present.

Selection rules for electric dipole transitions only allow

$$\Delta J = J_{\text{Upper}} - J_{\text{Lower}} = 0, \pm 1 \quad (3.3)$$

$\Delta J = 0$  is forbidden if  $\Delta l = l = 0$  (30), which is the case for most of the transitions that are relevant in the  $\text{CO}_2$  laser. The convention is to write P(J) and R(J) for transitions with  $\Delta J = -1$  and  $\Delta J = +1$  respectively, where J is the rotational quantum number of the lower laser level. Two such transitions, R(18) and P(18), are shown in Figure 3.2. The group of P- and R-transitions form the P- and R-branches in the infrared spectrum, and these were shown earlier in the  $\text{CO}_2$  laser gain spectra of Figure 2.3. The interline spacings are smaller in the R-branch. This is a consequence of the centrifugal distortion term in equation (3.2), and it is important in the high-pressure  $\text{CO}_2$  laser because line overlapping occurs at lower gas pressure in the R-branch.

### 3.1.2 Sequence bands and hot bands

Normally the regular  $\text{CO}_2$  laser transitions discussed in section 3.1.1 are the only observed transitions in a  $\text{CO}_2$  laser. It is known however that a number of other transitions originating from higher-lying vibrational levels may contribute to the laser gain and that they are particularly important at high gas pressure (29). The situation is illustrated in Figure 3.3a. Transitions of the type

$$(00^0\nu_3) \rightarrow (10^0(\nu_3-1)) \text{ or } (02^0(\nu_3-1)), \nu_3 \geq 2$$

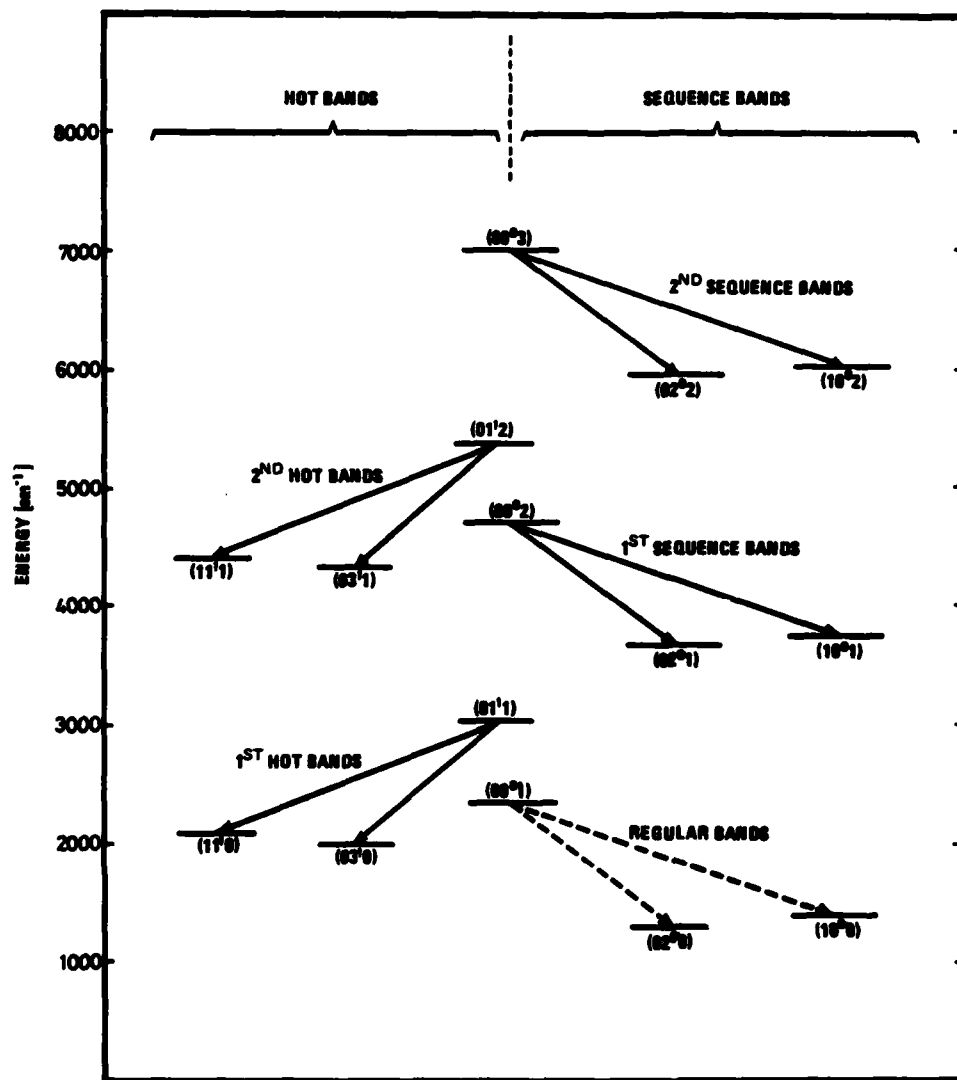
are called sequence band transitions, and these bands become increasingly important with increasing excitation of the  $\nu_3$  mode. Transitions of the type

$$(01^1\nu_3) \rightarrow (11^1(\nu_3-1)) \text{ or } (03^1(\nu_3-1)), \nu_3 \geq 1$$

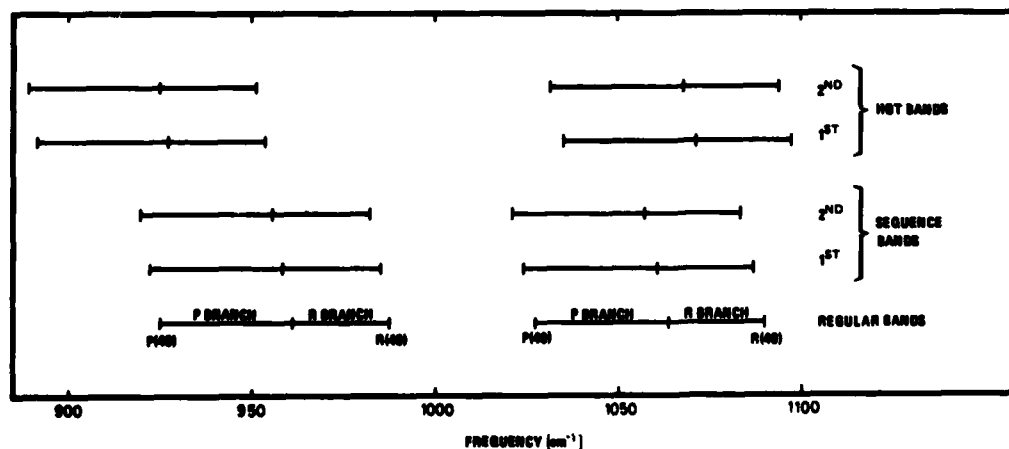
are called hot bands, and these occur because the first excited  $\nu_2$  vibrational level is populated via stimulated emission and relaxation processes in the laser or via thermal excitation.

Figure 3.3b shows that the frequency ranges of the sequence bands coincide very closely with those of the regular bands, and the small shifts of  $2\text{--}3\text{ cm}^{-1}$  per band are explained by anharmonicity and coupling between the vibrational modes. The hot bands are significantly more shifted, mainly because the Fermi resonance coupling gives a larger splitting of the lower hot band levels.

In low pressure  $\text{CO}_2$  lasers the effects of sequence bands and hot bands have been observed in measurements of anomalously high gain coefficients on regular laser lines that are accidentally overlapped by sequence band lines or hot band lines (29). Also by suppressing the regular laser lines, it has been possible to achieve laser oscillation on the sequence and hot bands (31). In high-pressure  $\text{CO}_2$  lasers the line structures merge into continuous gain profiles, and the gain on the sequence and hot bands adds effectively to the regular laser gain without the need for accidental coincidences. Especially the contribution from the sequence bands may be large since these bands are only slightly shifted from the regular bands and because the  $\nu_3$  mode may be very



(a)



(b)

Figure 3.3 Sequence bands and hot bands of the  $\text{CO}_2$  molecule

a) Vibrational energy level diagram showing sequence band transitions and hot band transitions

b) Frequency ranges of sequence bands and hot bands

The regular bands are included in a) and b) for comparison

strongly excited. The hot bands may also contribute significantly in certain frequency regions. This is discussed further in section 3.1.5.

### 3.1.3 Population distributions and the four-temperature model

If the gas is at thermal equilibrium at a temperature  $T$ , the probability  $\rho(n)$  of finding a molecule in a vibrational/rotational energy level  $n$  is given by the Boltzmann distribution

$$\rho(n) = \frac{1}{Q} \cdot \theta_n \cdot e^{-\frac{E_n}{kT}} \quad (3.4)$$

where

$\theta_n$  — degeneracy of the level  $n$

$E_n$  — energy of the level  $n$

$n$  — short notation for the quantum numbers  $(J, v_1 v_2^l v_3)$

and

$$Q = \sum_n \theta_n \cdot e^{-\frac{E_n}{kT}} \quad \text{—vibrational/rotational partition function}$$

By ignoring the small terms in  $E_n$  representing the coupling between vibration and rotation, one can make the separation

$$Q = Q_V \cdot Q_R \quad (3.5)$$

where  $Q_V$  and  $Q_R$  are vibrational and rotational partition functions. One can then calculate the vibrational and rotational population probabilities separately so that

$$\rho(J, v_1 v_2^l v_3) = \rho(J) \cdot \rho(v_1 v_2^l v_3) \quad (3.6)$$

The distribution  $\rho(J)$  has already been indicated in Figure 3.2, and  $\rho(J)$  has a maximum at about  $J = 16$  at room temperature due to the degeneracy  $\theta_J = 2J+1$  of the rotational levels. The expression for the vibrational population probability becomes particularly simple in the harmonic oscillator approximation

$$\rho(v_1 v_2^l v_3) = \frac{1}{Q_V} \cdot e^{-v_1 \frac{h\nu_1}{kT}} \cdot \theta_l \cdot e^{-v_2 \frac{h\nu_2}{kT}} \cdot e^{-v_3 \frac{h\nu_3}{kT}} \quad (3.7a)$$

where

$$Q_V = \left\{ \left(1 - e^{-\frac{h\nu_1}{kT}}\right) \cdot \left(1 - e^{-\frac{h\nu_2}{kT}}\right)^2 \cdot \left(1 - e^{-\frac{h\nu_3}{kT}}\right) \right\}^{-1} \quad (3.7b)$$

and

$$\theta_l = \begin{cases} 2, & l \neq 0 \\ 1, & l = 0 \end{cases}$$

It has in fact been shown (32) that the separation of vibration and rotation and neglect of anharmonicity and Fermi resonance effects lead to errors of only 1–2 per cent in the partition functions, and this accuracy will be sufficient in our laser model.



Having established approximate expressions for the population probabilities at thermal equilibrium, the question is if they can be useful in the description of a CO<sub>2</sub> laser gas where non-equilibrium conditions exist. In the CO<sub>2</sub> laser a large amount of pumping energy is injected into the gas, and a sequence of processes follows which brings the gas back towards thermal equilibrium. We shall see that some basic assumptions about the statistical situation in the gas during these processes will greatly simplify the picture of the laser dynamics. The assumptions are the following:

- a) The translational and rotational degrees of freedom are always in statistical equilibrium at a common temperature  $T$ .
- b) Statistical equilibrium always exists within each of the vibrational modes, and characteristic vibrational temperatures  $T_1$ ,  $T_2$  and  $T_3$  may be associated with the  $\nu_1$ ,  $\nu_2$  and  $\nu_3$  modes.

These assumptions are generally referred to as the four-temperature model (27), and the justifications for this model are the following:

- Energy exchange within the rotational degrees of freedom (R-R exchange) and between the rotational and translational degrees of freedom (R-T exchange) occur fast, the mean time between successive energy exchange events being typically one tenth of that between successive gas kinetic (T-T) collisions (33, 34). In good approximation it may thus be assumed that statistical equilibrium exists between translation and rotation throughout the many processes that involve exchange of vibrational energy. Being in statistical equilibrium, the T/R degrees of freedom may be characterized by a common temperature  $T$ .
- Exchange of vibrational quanta within each vibrational mode is a nearly resonant process which occurs faster than the exchange among different vibrational modes (V-V exchange) and exchange with the T/R degrees of freedom (V-T/R exchange) (35, 36). This fact justifies the assumption that statistical equilibrium is always maintained within each vibrational energy ladder, and characteristic vibrational temperatures  $T_1$ ,  $T_2$  and  $T_3$  may thus be associated with the  $\nu_1$ ,  $\nu_2$  and  $\nu_3$  vibrational modes.

The  $\nu_1$  and  $\nu_2$  modes are strongly coupled through the Fermi resonance, and they are usually assumed to possess a common vibrational temperature  $T_1 = T_2$  (36). Actually, since the  $\nu_1$  and  $\nu_2$  states are mixed in the Fermi resonance, it is no longer meaningful to use different temperatures  $T_1$  and  $T_2$ , which will be discussed in section 3.2.5.

The existence of four characteristic temperatures in the CO<sub>2</sub> laser gas was first proposed by Gordietz *et al* (37) and Moore *et al* (38), and this has been the basic assumption in later CO<sub>2</sub> laser models (27). The great advantage of such an approach is that the large number of rate equations for the populations of individual vibrational levels can be replaced by a few rate equations for the energies stored in each of the vibrational modes.

The validity of the assumptions can only be confirmed by measuring the populations of the various levels under realistic laser operating conditions, and such measurements have recently been made both in continuous-wave (39) and pulsed (36) electrically excited CO<sub>2</sub> lasers. These measurements include the use of regular band, sequence band and hot band lasers for probing of populations in several vibrational levels. Also by using a tunable diode laser for probing, Dang *et al* (40) have been able to probe populations of levels up to (00<sup>0</sup>9) in a cw CO<sub>2</sub> laser discharge. The results seem to confirm the validity of the four-temperature model with the common temperature  $T_1 = T_2$  for the  $\nu_1$  and  $\nu_2$  modes. Deviations from a Boltzmann distribution are

observed for high  $\nu_3$  levels, but since these give small contributions to the gain, the assumption of a Boltzmann distribution can still be maintained.

Knowledge of the time evolution of the characteristic temperatures in this approximate model allows us to calculate the population of any vibrational/rotational level and the gain on any transition as a function of time. The rotational population probabilities  $\rho(J)$  are determined by  $T$ , while the vibrational populations are found by including  $T_1$ ,  $T_2$  and  $T_3$  in the expressions of equation (3.7)

$$\rho(\nu_1 \nu_2 \nu_3) = \frac{1}{Q_V} \cdot e^{-\nu_1 \frac{h\nu_1}{kT_1}} \cdot \theta_l \cdot e^{-\nu_2 \frac{h\nu_2}{kT_2}} \cdot e^{-\nu_3 \frac{h\nu_3}{kT_3}} \quad (3.8a)$$

$$\text{where} \\ Q_V = \left\{ \left(1 - e^{-\frac{h\nu_1}{kT_1}}\right) \cdot \left(1 - e^{-\frac{h\nu_2}{kT_2}}\right)^2 \cdot \left(1 - e^{-\frac{h\nu_3}{kT_3}}\right) \right\}^{-1} \quad (3.8b)$$

We shall rewrite the expressions for later use in our laser model, introducing the quantity  $\bar{N}_i$  which denotes the average number of excited  $\nu_i$  quanta per  $\text{CO}_2$  molecule. It is easily found that

$$\bar{N}_i = \left( e^{\frac{h\nu_i}{kT_i}} - 1 \right)^{-1}, \quad i = 1, 3 \quad (3.9a)$$

and

$$\bar{N}_2 = 2 \left( e^{\frac{h\nu_2}{kT_2}} - 1 \right)^{-1} \quad (3.9b)$$

The equations (3.8) and (3.9) give

$$\rho(\nu_1 \nu_2 \nu_3) = \frac{1}{Q_V} \cdot \left( \frac{\bar{N}_1}{1 + \bar{N}_1} \right)^{\nu_1} \cdot \theta_l \cdot \left( \frac{\bar{N}_2}{2 + \bar{N}_2} \right)^{\nu_2} \cdot \left( \frac{\bar{N}_3}{1 + \bar{N}_3} \right)^{\nu_3} \quad (3.10a)$$

and

$$Q_V = (1 + \bar{N}_1) \cdot \left(1 + \frac{\bar{N}_2}{2}\right)^2 \cdot (1 + \bar{N}_3) \quad (3.10b)$$

It is convenient to use  $\bar{N}_i$  instead of  $T_i$  in the modelling of the energy flow in the gas because  $\bar{N}_i \cdot h\nu_i$  is simply the average vibrational energy per  $\text{CO}_2$  molecule stored in mode  $i$ . The energy flow including V-V and V-T/R processes can be described by a set of rate equations for  $\bar{N}_1$ ,  $\bar{N}_2$  and  $\bar{N}_3$ , and this will greatly simplify the theory of the  $\text{DF} \rightarrow \text{CO}_2$  transfer laser in section 3.2.

### 3.1.4 $\text{CO}_2$ laser gain

When radiation of frequency  $\nu$  travels in the  $z$ -direction through an amplifying laser medium, the radiation intensity  $I(\nu)$  increases according to

$$\frac{dI(\nu)}{dz} = \alpha_L(\nu) \cdot I(\nu) \quad (3.11)$$

where

$\alpha_L(\nu)$  — laser gain coefficient at the frequency  $\nu$

In this section we consider the case where only a single laser transition contributes to the gain. The gain coefficient can then be expressed as (27)

$$\alpha_L(\nu) = \frac{1}{8\pi c \nu^2} \cdot A_{ul} \cdot g(\nu) \cdot \left(N_u - \frac{\theta_u}{\theta_l} \cdot N_l\right) \quad (3.12)^*$$

where

$c$  — speed of light

$A_{ul}$  — spontaneous Einstein coefficient

$g(\nu)$  — line shape factor for the laser transition ( $\int g(\nu) d\nu = 1$ )

$N_u, N_l$  — upper/lower laser level population densities

$\theta_u, \theta_l$  — upper/lower laser level degeneracies

$$\Delta N = N_u - \frac{\theta_u}{\theta_l} \cdot N_l \quad (3.13)$$

is the population inversion.

In high pressure gas lasers the transitions are predominantly collision broadened, giving Lorentzian line shapes

$$g(\nu) = \frac{1}{\pi} \cdot \frac{\gamma_L}{(\nu - \nu_0)^2 + \gamma_L^2} \quad (3.14)$$

where

$\nu_0$  — line centre frequency

$\gamma_L$  — Lorentz half width at half maximum

$\gamma_L$  depends on the gas mixture and is proportional to the gas pressure.

The population inversion  $\Delta N$  on a  $\text{CO}_2$  laser transition can be expressed in terms of the probabilities  $\rho(J)$  and  $\rho(v_1 v_2' v_3)$  which were discussed in section 3.1.3. As an example we may consider an  $R(J)$  transition in the  $(00^01) \rightarrow (10^00)$  regular  $\text{CO}_2$  laser band.  $\Delta N$  is then given by

$$\Delta N = \frac{N_{\text{CO}_2}}{(1+N_1)(1+\frac{N_2}{2})(1+N_3)} \cdot \left\{ \frac{N_3}{1+N_3} \cdot \rho(J+1) - \frac{2J+3}{2J+1} \cdot \frac{N_1}{1+N_1} \cdot \rho(J) \right\} \quad (3.15)$$

where

$N_{\text{CO}_2}$  — density of  $\text{CO}_2$  molecules.

It can be observed that  $\Delta N$  reaches a maximum at  $N_3 = 1$  which corresponds to  $T_3 \approx 4880$  K. Stronger excitation of the  $\nu_3$  mode only leads to increased gain on the sequence bands while the gain on the regular bands decreases.

It is important to note that the gain will be affected by the radiation intensity  $I(\nu)$ , since the molecules are brought from the upper to the lower laser level in the amplification process. This is clearly observed in the build-up of the radiation intensity in a pulsed laser like the one we study in this work. In the first period after the start of the excitation, the intensity increases exponentially according to equation (3.11). After a time  $\tau$  the intensity becomes so high that the stimulated emission rate out of the upper laser level exceeds the pumping rate, and due to the high gain the integrated pumping energy is extracted in a short and intense laser pulse. This pheno-

\*Note that  $\nu$  and  $g(\nu)$  are given in units of  $(\text{cm}^{-1})$  and  $(\text{cm}^{-1})^{-1}$  respectively.

menon is called gain-switching, and the time  $\tau$  before the saturation of the gain sets is called the laser oscillation build-up time.

An example of such a gain-switched pulse was shown earlier in Figure 2.6. Efficient extraction of the stored excitation energy does not start until saturation of the gain sets in, and it is therefore important that the build-up time is shorter than the non-radiative decay time of the upper laser level.

### 3.1.5 High-pressure CO<sub>2</sub> laser gain

The full width at half maximum (FWHM) of collision broadened laser transitions is found from equation (3.14) to be twice the Lorentz half width  $\gamma_L$ . In CO<sub>2</sub> lasers collision broadening is predominant at pressures above 100 torr, and  $2\gamma_L$  increases with 0.12–0.19 cm<sup>-1</sup> per atmosphere depending on the gas mixture (41).  $\gamma_L$  varies slightly for the different transitions, and it depends on temperature. Since the spacings between adjacent CO<sub>2</sub> laser lines are 1–2 cm<sup>-1</sup>, considerable line overlapping is obtained when the pressure is increased to ten atmospheres, making continuous tuning of the laser frequency possible. Figure 3.4 repeats the calculated CO<sub>2</sub> laser gain spectra at

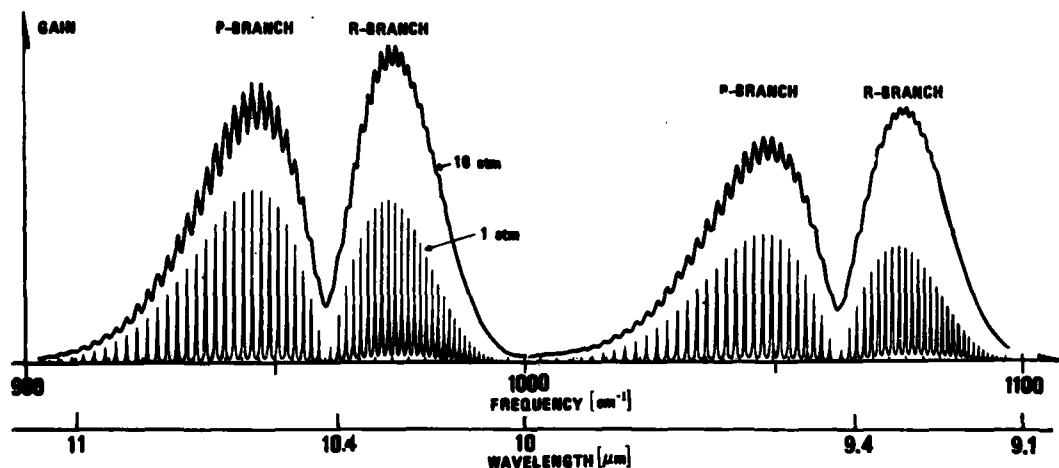


Figure 3.4 CO<sub>2</sub> laser gain spectra (after (25))

Lower curve — 1 atm gas pressure  
Upper curve — 10 atm gas pressure

1 atm and 10 atm pressure that were shown earlier in Figure 2.3. Only regular CO<sub>2</sub> laser transitions are taken into account in the calculation of these spectra. We shall make some comments about the interpretation of the curves and about factors that influence the variation of the gain with gas pressure.

It is useful to look back at the equations (3.12) and (3.14) for the single line gain coefficient  $\alpha_L(\nu)$  and the Lorentz line shape function  $g(\nu)$ . The value of the line shape function at the line centre is given by  $g(\nu_0) = (\pi \cdot \gamma_L)^{-1}$ . We then find that the line centre gain varies according to

$$\alpha_L(\nu_0) \propto \Delta N \cdot \gamma_L^{-1}$$

where  $\Delta N$  is the population inversion.  $\gamma_L$  is proportional to the gas pressure, and if we assume that a constant pumping energy is available,  $\Delta N$  will normally decrease with increasing pressure due to faster relaxation processes. There will thus be a serious reduction in the line centre gain for increasing pressure. However, as soon as the lines start to overlap, the reduction is greatly compensated for as illustrated in Figure 3.4. The pure contribution from line overlapping is here sorted out as the difference between the two curves, by letting  $\Delta N$  be proportional to the pressure in the calculations. It is important to note that the gain increases faster in the R branch than in the P branch due to the closer line spacings. The ratio of the line centre gain including line overlapping to the single line gain will be called  $\kappa$ .

Equally important in a high-pressure  $\text{CO}_2$  laser is the contribution to the gain from the sequence bands. It was shown in Figure 3.3b that the sequence bands were only slightly shifted from the regular bands, and at high gas pressure with continuous gain spectra, the gain on the sequence bands add effectively to the gain on the regular bands. We shall write  $\alpha_n$  for the gain on transitions originating from the  $(00^0n)$  vibrational level, and the ratio  $\alpha_n:\alpha_1$  is approximately given by (29)

$$\frac{\alpha_n}{\alpha_1} = n \cdot e^{-(n-1) \frac{h\nu_3}{kT_3}} \quad (3.16)$$

where the Boltzmann factor comes from the ratio of the upper laser level populations at the vibrational temperature  $T_3$ , and the factor  $n$  is the ratio of the square of the matrix elements calculated in the harmonic oscillator approximation. Deviations from the factor  $n$  will occur because of variations in the Fermi resonance coupling for the different bands. However, data for these corrections are not well known, and we shall make our calculations in the approximation of equation (3.16). Introducing the quantity  $\bar{N}_3$  from section 3.1.3 and summing the contributions from all bands we find that

$$\sum_{n=1}^{\infty} \alpha_n = \alpha_1 \cdot (1 + \bar{N}_3)^2 \quad (3.17)$$

We observe that if there is an average of 0.5 excited  $\nu_3$  quanta per  $\text{CO}_2$  molecule, the total gain exceeds that of the regular band with 125%. This corresponds to a  $T_3$  of 1080 K, which is not unusual in a strongly excited  $\text{CO}_2$  laser. It should be remembered that  $(1 + \bar{N}_3)^2$  is only an approximate factor, which accounts for the average expected contribution from the sequence bands. In reality, each sequence band has its own fine structure like the 10 atm gain curve in Figure 3.4, and it is not easy to predict the real spectral shape of the total gain.

When the factor  $(1 + \bar{N}_3)^2$  and the line overlapping factor  $\kappa$  is included, our final expression for the gain at the line centre of one of the regular laser lines will be

$$L(\nu_0) = \frac{1}{8\pi c \nu_0^2} \cdot A_{ul} \cdot \left( \frac{1}{\pi \cdot \gamma_L} \cdot \kappa \right) \cdot (1 + \bar{N}_3)^2 \cdot \left( N_u - \frac{\theta_u}{\theta_l} \cdot N_l \right) \quad (3.18)^*$$

$\frac{1}{\pi \gamma_L} \cdot \kappa$  is the value of the line shape factor at the line centre corrected for line overlapping.

$N_u - \frac{\theta_u}{\theta_l} \cdot N_l$  is the population inversion of the regular laser transition which can be expressed as in equation (3.15).

\*Note that  $\nu_0$  and  $\gamma_L$  are given in units of  $(\text{cm}^{-1})$ .

Hot bands might have been included in the model in a similar way as the sequence bands. They are however significantly displaced from the regular bands, and in some regions they do not contribute at all. This is the case in the R branch at  $975\text{ cm}^{-1}$  (see Figure 3.3b) where our laser oscillates in all the high-pressure laser experiments, and we have therefore left the hot bands out of the model. (As explained previously, the gain is highest in the R-branches at high gas pressures).

It should be noted that this theory is based on the assumption of pure Lorentz overlapping between independent vibrational/rotational lines. It is however known that line shapes are never exactly Lorentzian, and especially in the case of line overlapping, interaction between adjacent lines tends to distort the line shapes. Theoretical calculations have been carried out for  $\text{CO}_2$  which show that such interaction leads to higher gain (or absorption) on the line centres and lower gain (or absorption) between the lines than what is predicted by simple Lorentz overlap theory (42). The measured absorption on the line centres in a high-pressure  $\text{CO}_2$  gas seems to agree well with this theory (42), but the deviations from Lorentz overlap theory are typically less than 10% for pressures up to 10 atm.

It is probable that such effects will have some influence on the frequency tuning characteristics of a high-pressure  $\text{CO}_2$  laser, but we have not been able to analyse this theoretically within the frame of the present work.

### 3.2 Theory of the optically pumped DF $\rightarrow$ $\text{CO}_2$ transfer laser

Having presented the theoretical background for the calculation of population densities and gain in the high-pressure  $\text{CO}_2$  gas, we are ready to start the discussion of the optically pumped high-pressure DF $\rightarrow$  $\text{CO}_2$  transfer laser. A qualitative discussion of basic principles and features of the laser system was given in section 2.2, and here we shall describe in further detail the various processes that are involved in the conversion of pumping photons into  $\text{CO}_2$  laser photons. The dynamics of the laser system is described by a set of rate equations which will be solved in the computer simulations of chapter 4.

At this point it may be instructive to repeat the energy level diagrams of Figure 2.5 showing the laser transitions of the DF pumping laser and the absorption and laser transitions of the optically pumped DF $\rightarrow$  $\text{CO}_2$  transfer laser. The diagrams are shown in Figure 3.5.

The basic properties of the pumping laser radiation will be summarized in section 3.2.1. In section 3.2.2 we extend the four-temperature model of section 3.1.3, including also characteristic temperatures for the DF absorbing gas, and a simplified block diagram for the energy transport in the laser system is presented. The theory of the different energy exchange processes is then treated in the following sections.

#### 3.2.1 The DF pumping laser

Being a two-atomic molecule, DF has only one vibrational mode, and we denote its vibrational frequency by  $\nu_4$  and its vibrational quantum number by  $v_4$ . We also use the notation  $v_4P(J)$  for the vibrational/rotational transition  $(v_4, J-1) \rightarrow (v_4-1, J)$ . All transitions  $(v_4) \rightarrow (v_4-1)$  are briefly referred to as the  $(v_4 \rightarrow v_4-1)$  transitions or the  $(v_4 \rightarrow v_4-1)$  bands. This notation is used for the DF pumping laser transitions as well as for the absorption transitions of the DF molecules in the optically pumped DF  $\rightarrow$   $\text{CO}_2$  transfer laser.

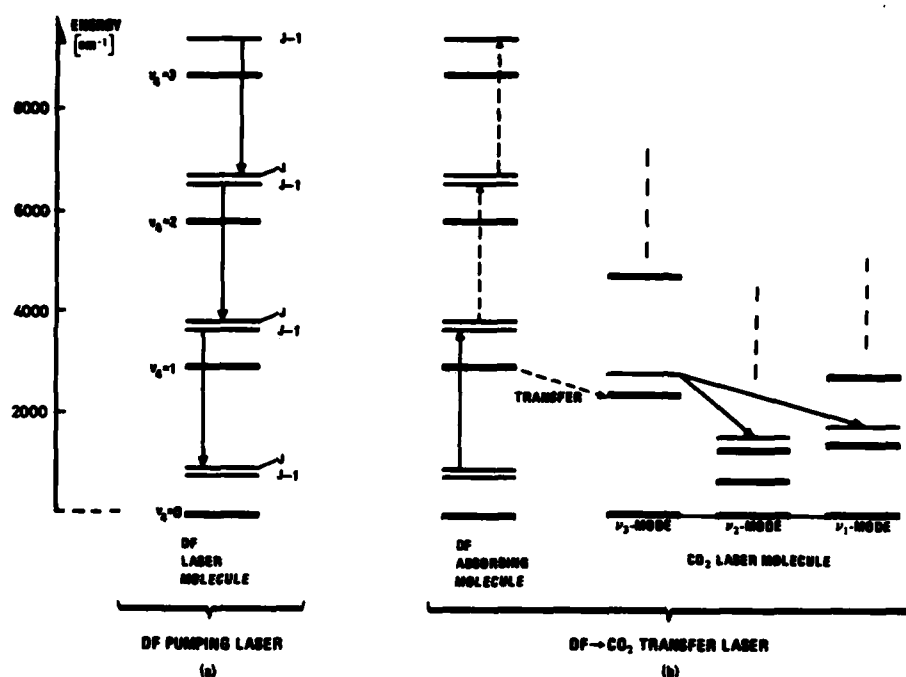


Figure 3.5 Energy level diagrams of the DF pumping laser (a) and of the DF → CO<sub>2</sub> transfer laser (b)

The figure is a repetition of Figure 2.5. The DF vibrational quantum number is here denoted by  $v_4$ .

In section 2.2 it was mentioned that the DF pumping laser can oscillate on about 25 transitions in the (1→0), (2→1) and (3→2) bands. The transitions involved are typically P(4)...P(12) in each band. Using a simple two-mirror DF laser resonator, all these lines will oscillate in the same laser pulse. If one of the laser mirrors is replaced by a diffraction grating, it is possible to obtain laser oscillation on a single line. The maximum pulse energies in multiline and single-line oscillation are about 600 mJ and 80 mJ respectively for the laser used in this work. In either case the pulse width at half maximum is about 400 ns. Details of the two resonator configurations and the laser output characteristics are given in chapter 5.

Both multiline and single-line DF laser pulses have been used in our experiments for pumping of the DF→CO<sub>2</sub> transfer laser, and a qualitative discussion of the pumping process in the two cases will be given in section 3.2.3. However, only single-line pumping will be treated in the further development of a mathematical laser model and in the computer calculations. The modelling in the case of multiline pumping would have required inconveniently long computer processing times, without significantly increasing our insight into the physics of the laser system. In addition, our experiments have revealed that equally high CO<sub>2</sub> laser pulse energies can be obtained with single-line pumping.

The 1P(7) DF laser line at 2743 cm<sup>-1</sup> has been used in all the single line pumping experiments, and the examples of the following sections are given for realistic laser operating conditions using this line for pumping.

### 3.2.2 Extention of the four temperature model

In section 3.1 we saw that the populations in the various  $\text{CO}_2$  energy levels and the  $\text{CO}_2$  laser gain could be expressed in terms of the characteristic temperatures  $T$ ,  $T_1$ ,  $T_2$  and  $T_3$  of the  $\text{CO}_2$  gas. In the modelling of the optically pumped  $\text{DF} \rightarrow \text{CO}_2$  transfer laser we have to know the dynamical behaviour of the absorption coefficient for the pumping radiation, and this requires knowledge of the population probabilities  $\rho(v_4, J)$  of the vibrational/rotational levels of the absorbing DF molecules. Using the same arguments as for  $\text{CO}_2$  it is therefore convenient to associate characteristic temperatures  $T_4$  and  $T$  with the vibrational and rotational/translational degrees of freedom of the DF molecules. We might call this a two-temperature model for the DF gas, and the following comments should be made about the assumptions:

- R-R and R-T energy exchanges occur fast also in DF (43), and we may assume to a good approximation that a common T/R temperature  $T$  is established.  $T$  will then actually be a common T/R temperature for all three gases DF,  $\text{CO}_2$  and He in the high-pressure laser gas mixture.
- The internal V-V relaxation rate constant of  $8.1 \cdot 10^8 \text{ s}^{-1} \cdot \text{atm}^{-1}$  in the DF vibrational mode (44) is an order of magnitude lower than that of  $\text{CO}_2$ . In our experiments the DF partial pressure is only 0.02–0.11 atm, giving internal relaxation rates of  $1.6 \cdot 10^7 - 8.9 \cdot 10^7 \text{ s}^{-1}$ . These are in the same range as the pumping rate into the DF vibrational mode (see chapter 4) and the transfer rate to the  $\text{CO}_2$   $\nu_3$  mode (see section 3.2.4), and we must obviously take into account the possibility of a non-Boltzmann distribution in the DF vibrational energy ladder as a source of error in our model. This effect may be among the explanations for the discrepancies between calculated and observed laser pulses as discussed in chapters 4 and 6.

In analogy with the approximations made for  $\text{CO}_2$  it is assumed that the vibrational and rotational partition functions can be decoupled so that  $\rho(v_4, J) = \rho(v_4)\rho(J)$ .

We also assume that the vibrational motion is strictly harmonic, and we introduce the quantity  $\bar{N}_4$ , denoting the average number of excited vibrational quanta per DF molecule. As in equation (3.9a) the relation between  $\bar{N}_4$  and  $T_4$  is given by

$$\bar{N}_4 = \left( e^{\frac{h\nu_4}{kT_4}} - 1 \right)^{-1} \quad (3.19)$$

We then find the population probabilities  $\rho(v_4)$  for the vibrational levels

$$\rho(v_4) = \frac{1}{1 + \bar{N}_4} \cdot \left( \frac{\bar{N}_4}{1 + \bar{N}_4} \right)^{v_4} \quad (3.20)$$

and the rotational level population probabilities  $\rho(J)$  are calculated at the T/R temperature  $T$  as for  $\text{CO}_2$ .

Having established a simplified model of the laser with statistical equilibrium within each vibrational mode and within the T/R degrees of freedom, the energy transport in the laser system can be illustrated by the block diagram in Figure 3.6. The rectangular blocks represent the energy stored in the various degrees of freedom of the laser gas mixture. Note that  $\bar{N}_i$  uniquely determines the energy of vibrational mode number  $i$ . Statistical equilibrium between the  $\nu_1$  and  $\nu_2$  vibrational modes in  $\text{CO}_2$  is assumed



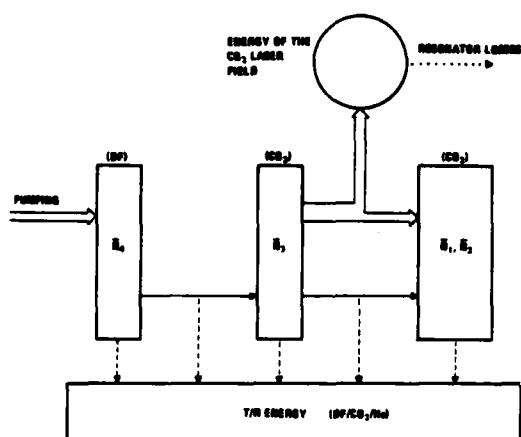


Figure 3.6 Block diagram of the energy transport in the optically pumped  $DF \rightarrow CO_2$  transfer laser  
Refer to comments in the text

because of the strong Fermi resonance, and  $\bar{N}_1$  and  $\bar{N}_2$  are therefore gathered in one block. The circular area represents the electromagnetic energy of the  $CO_2$  laser field in the laser resonator.

Collisional energy exchange occurs among the vibrational modes (solid arrows) or between the vibrational modes and the T/R degrees of freedom (dashed arrows). The open arrows represent energy exchange with the pumping laser field and with the  $CO_2$  laser field. The dotted arrow represents the energy loss of the  $CO_2$  laser resonator field due to output coupling, absorption and scattering in mirrors etc. Note that dashed arrows are connected with the solid arrows between the  $\nu_4$  and  $\nu_3$  modes and between the  $\nu_3$  and  $\nu_1/\nu_2$  modes. These indicate that the energy defects of the V-V processes must be exchanged with the T/R energy.

It should be noted that all the energy exchange processes (except radiation energy losses in the resonator) are influenced by changes in the T/R temperature  $T$ .  $T$  will obviously increase during the laser process, and the effects of such an increase are discussed in section 3.2.6. The time dependence of  $T$  has been found approximately in the computer simulations, but the influence on the different energy exchange processes has not yet been taken into account, and that will be a source of error in the model.

Keeping the picture of Figure 3.6 in mind we proceed with a discussion of the different energy exchange processes.

### 3.2.3 The pumping process

The radiation intensity  $I_p(\nu_p)$  of a DF pumping laser line is absorbed by the DF gas according to

$$\frac{\partial I_p(\nu_p)}{\partial z} + \frac{1}{c} \frac{\partial I_p(\nu_p)}{\partial t} = -\alpha_p(\nu_p) \cdot I_p(\nu_p) \quad (3.21)$$

where the absorption coefficient  $\alpha_p(\nu_p)$  is given by

$$\alpha_p(\nu_p) = \frac{1}{8\pi c \nu_p^2} \cdot g(\nu_p) \cdot A_{ul} \cdot (N_l \frac{\theta_u}{\theta_l} - N_u) \quad (3.22)^*$$

\*Note that  $\nu_p$  and  $g(\nu_p)$  are given in units of  $(cm^{-1})$  and  $(cm^{-1})^{-1}$  respectively.

The expression (3.22) is identical to that of the laser gain coefficient defined by equation (3.12), with the exception of the sign and that all the parameters here relate to a DF absorption line.

Since the absorption transitions are the same as the DF pumping laser transitions, the absorption process is inherently resonant. The total gas pressure in the pumping laser is only 0.04 atm, giving a gain line width which is very narrow compared with the DF absorption line width in the high-pressure gas, and the Lorentz line shape factor  $g(\nu_p)$  may to a good approximation be replaced by its value  $g(\nu_{0p})$  at the absorption line centre

$$g(\nu_p) \approx g(\nu_{0p}) = \frac{1}{\pi\gamma_p} \quad (3.23)$$

$\nu_{0p}$  — absorption line centre frequency

$\gamma_p$  — Lorentz half width at half maximum of the absorption line.

The populations  $N_l$  and  $N_u$  can be expressed in terms of the quantities  $N_4$ ,  $\rho(J)$  and  $\rho(J-1)$  which were discussed in section 3.2.2. At room temperature practically all the DF molecules are in the vibrational ground state ( $N_4 \approx 0$ ), and only the (1→0) pumping lines will be significantly absorbed. The line centre absorption coefficient for a 1P(J) line is

$$\alpha_p(\nu_{0p}) = \frac{1}{8\pi c \nu_{0p}^2} \cdot \frac{1}{\pi\gamma_p} \cdot A_{ul} \cdot \left( \frac{2J-1}{2J+1} \cdot \frac{1}{1+N_4} \cdot \rho(J) - \frac{N_4}{(1+N_4)^2} \rho(J-1) \right) \cdot N_{DF} \quad (3.24)^*$$

$N_{DF}$  — density of DF molecules.

Obviously only (1→0) DF laser lines can be efficient for excitation if a single pumping line is used. In multiline pumping on the other hand, the (2→1) and (3→2) lines may contribute to the excitation through cascade pumping up the DF vibrational energy ladder as was indicated in Figure 3.5. The size of this contribution will depend on the intensity of the (1→0) lines, the absorption coefficients and on the speed of the energy transfer from DF to the CO<sub>2</sub>  $\nu_3$  mode. As explained previously we have not done any modelling of the laser in the case of multiline pumping, but our calculations of excitation with the 1P(7) DF laser line indicate that the population in the first excited DF vibrational level will typically be about 20% of that in the ground vibrational level. This is calculated for a 10 atm gas mixture at the input end of the gas cell and at the time of peak pumping power (see also chapter 4). A lower population in the first vibrational level is expected in the case of multiline pumping because the absorption coefficients for the strongest (1→0) lines are low in that case (see below). It may therefore seem that the contribution to the excitation from the (2→1) and (3→2) lines will be of minor importance.

Einstein coefficients and Lorentz broadening coefficients for the 1P(5)...1P(10) transitions in DF have been reported in (45). This is the only work reporting such data for DF. When these data are used in equation (3.24), the absorption coefficients of Figure 3.7 are found for the Lorentz broadened lines of pure DF at room temperature. These are small signal absorption coefficients ( $N_4 \approx 0$ ), and we observe that the penetration depths will be typically 1–10 mm. The absorption decreases with increasing J for these lines, since the rotational population distribution has a maximum for J=2 in DF at room temperature. For comparison the relative distribution of pulse energies in the (1→0) band of the DF laser is also indicated in Figure 3.7 for the case

\* Note that  $\nu_{0p}$  and  $\gamma_p$  are given in units of (cm<sup>-1</sup>).

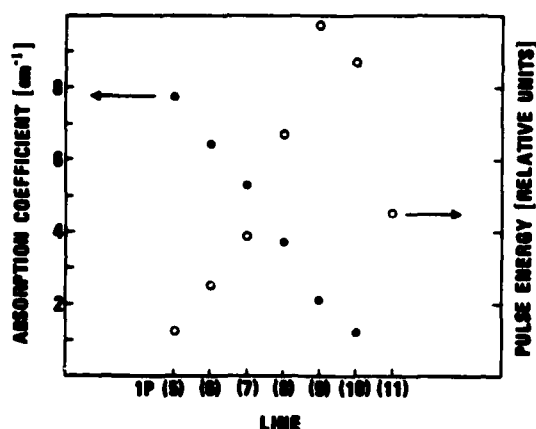


Figure 3.7 Absorption coefficients on the  $(1 \rightarrow 0)$  DF absorption lines (dots), and relative pulse energies on the  $(1 \rightarrow 0)$  DF laser lines in multiline operation (circles)

of multiline DF laser operation. The 1P(9) and 1P(10) lines are strongest, but the relatively low absorption coefficients for these lines reduce their efficiency in the excitation. Using single-line pumping we may choose a pumping laser line which is strongly absorbed. The 1P(7) line represents a good choice since it is reasonably strongly absorbed and because it has a relatively high output energy compared with 1P(9) and 1P(10) in single line operation. This will be discussed further in chapter 5.

In the high-pressure DF $\rightarrow$ CO<sub>2</sub> transfer laser the absorption lengths are considerably larger for two reasons:

First, the absorption coefficients are greatly reduced due to pressure broadening of the DF lines by CO<sub>2</sub> and He. The Lorentz half width at half maximum  $\gamma_p$  for a DF line is

$$\gamma_p = (P_{DF} \gamma_{DF}^0 + P_{CO_2} \gamma_{CO_2}^0 + P_{He} \gamma_{He}^0) \quad (3.25)$$

where

$\gamma_{DF}^0, \gamma_{CO_2}^0, \gamma_{He}^0$  — specific Lorentz broadening coefficients for the absorption line

$P_{DF}, P_{CO_2}, P_{He}$  — partial pressures

Compared with pure DF the line centre absorption coefficient is reduced by the factor

$$\frac{\gamma_p(\text{pure DF})}{\gamma_p} = \frac{P_{DF} \gamma_{DF}^0}{P_{DF} \gamma_{DF}^0 + P_{CO_2} \gamma_{CO_2}^0 + P_{He} \gamma_{He}^0} \quad (3.26)$$

Table 3.1 gives the relative contributions to  $\gamma_p$  for the 1P(7) transition in DF due to collisions with DF, CO<sub>2</sub> and He. The data are calculated for a typical 10 atm laser gas mixture containing 0.5% DF, 5% CO<sub>2</sub> and 94.5% He. Only theoretical values for  $\gamma_{CO_2}^0$  have been reported (46), but the values are in good agreement with rough spectroscopic measurement made by ourselves during this work.  $\gamma_{He}^0$  has been measured for the 1P(8) line (47), and we have only roughly estimated the value for 1P(7) by assuming that  $\gamma_{He}^0 \gamma_{DF}^0$  is the same for 1P(7) as for 1P(8).

It is important to observe that  $\gamma_{He}^0$  is as much as 60 times smaller than  $\gamma_{DF}^0$ . This means that a reasonably strong absorption can be maintained even if  $P_{He}$  exceeds  $P_{DF}$  by a factor of 200. Using the data of Table 3.1 we find that the ratio of

Gas	$P_{10}$ (atm)	$\gamma_{10}^0$ ( $\text{cm}^{-1} \cdot \text{atm}^{-1}$ )	$P_{10} \cdot \gamma_{10}^0$ ( $\text{cm}^{-1}$ )	$\gamma_p$ ( $\text{cm}^{-1}$ )
DF	0.05	0.20	0.010	
CO <sub>2</sub>	0.5	0.06	0.030	
He	0.45	0.006	0.0027	
				0.007

Table 3.1 Contributions from DF-, CO<sub>2</sub>- and He-collisions to the pressure broadened half width at half maximum,  $\gamma_p$  of the 1P(7) DF absorption line (45, 46, 47)

equation (3.26) is approximately 1.6. Similar ratios could have been calculated for the other DF absorption lines, and altogether we find that the absorption lengths increase typically from millimeters to centimeters, due to the broadening of the lines by CO<sub>2</sub> and He.

The other important reason for increased absorption lengths is saturation of the absorption coefficient because of the high pumping power densities. Figure 3.8a shows an example of a computer calculation made of the time behaviour of  $\bar{N}_4$  at the input end of the laser gas cell at 10 atm pressure and using the 1P(7) line

for pumping.  $\bar{N}_4 \approx 0.36$  at the peak of the pumping pulse, and we find from equation (3.24) that  $\alpha_p(\nu_{0p})$  is reduced by a factor of 3 due to saturation. We have then taken into account that  $\rho(J=6) \approx 1.8 \cdot \rho(J=7)$  at  $T = 300$  K. In Figure 3.8b we show the calculated variation of the pumping radiation intensity through the 10 cm gas cell at the peak of the pumping pulse, as well as the corresponding unsaturated absorption curve. In our experiments the saturation effects are observed in a sharpening of the pumping pulse shape through the gas cell, and this will be discussed in chapters 4 and 6. It should be noticed that the energy transfer from DF to CO<sub>2</sub> plays an important role in reducing the saturation of the absorption, and the energy transfer rate increases with increasing CO<sub>2</sub> concentration. Unfortunately CO<sub>2</sub> also severely broadens the DF absorption lines as we can see in Table 3.1 above, and it is therefore not easy to predict how a variation in the CO<sub>2</sub> pressure will influence the amount of absorbed pumping energy.

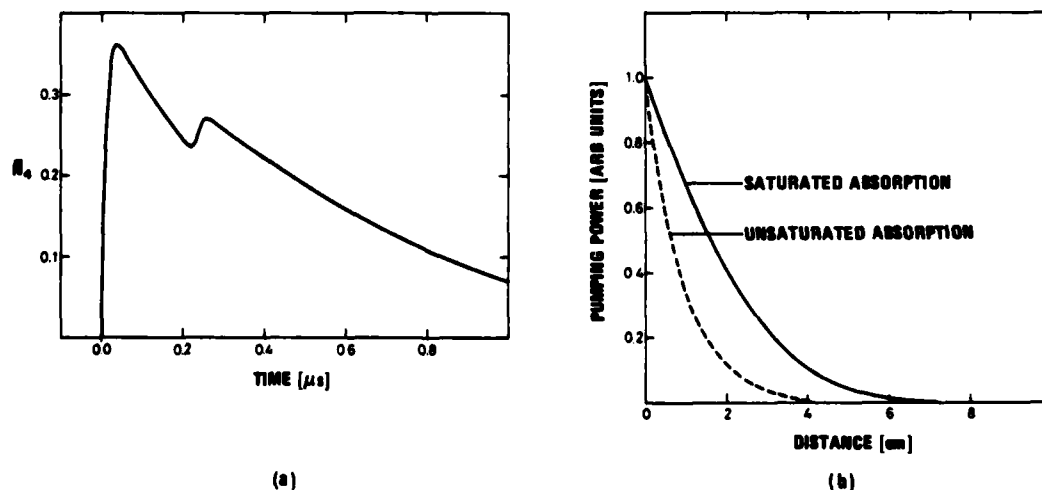


Figure 3.8 Saturation effects in the absorption of the pumping radiation

- The time dependence of the average number of excited vibrational quanta per DF molecule,  $\bar{N}_4$ . The peak of  $\bar{N}_4$  coincides with the peak of the pumping pulse.
- Variation of the peak pumping power as a function of the distance from the input end of the laser gas cell (solid curve). The dashed curve shows the corresponding dependence in the case of unsaturated absorption (small signal absorption).

Further details are given in chapter 4.

The pumping radiation intensity,  $I_p$ , and the average number of excited vibrational quanta per DF molecule,  $\bar{N}_4$ , have been the two important variables of this section. They are both functions of time  $t$  and position  $z$  in the laser gas cell, and the following two differential equations for the two variables go into our mathematical laser model:

$$\frac{\partial I_p}{\partial z} + \frac{1}{c} \frac{\partial I_p}{\partial t} = -\alpha_p \cdot I_p \quad (3.27)$$

$$N_{DF} \cdot \dot{\bar{N}}_4 = \alpha_p \cdot \frac{I_p}{h\nu_p} - k_T \cdot N_{DF} \cdot \bar{N}_4 \quad (3.28)$$

Equation (3.27) is the same as equation (3.21) at the beginning of this section. Remember that  $\alpha_p$  is a function of  $\bar{N}_4$  as can be seen in equation (3.24) above. The last term of equation (3.28) represents the transfer of DF vibrational quanta to the  $\text{CO}_2$   $\nu_3$  mode, and that process will be the subject of section 3.2.4.

It should be noted that we have assumed the pumping laser field to be a plane wave in equation (3.27), and this is one of the simplifications in our model which may lead to significant errors in the calculated results.

#### 3.2.4 Energy transfer from DF to $\text{CO}_2$

The vibrational energy transfer from the DF vibrational mode to the  $\text{CO}_2$   $\nu_3$  mode is obviously a critical process in the laser, and the DF- $\text{CO}_2$  system here possesses two important advantages compared with most other transfer laser systems:

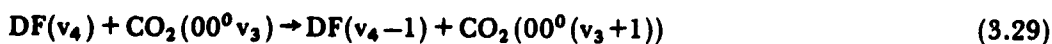
a) The energy transfer occurs extremely fast

and

b) Energy transfer back from  $\text{CO}_2$  is unimportant because the energy defect  $\Delta E = h\nu_4 - h\nu_3$  of the process is  $550 \text{ cm}^{-1}$ , which is 2-3 times larger than  $kT$

The combination of these two properties is surprising because the transfer probability usually becomes small in systems where  $\Delta E$  substantially exceeds  $kT$ , which is about  $200 \text{ cm}^{-1}$  at room temperature. The high transfer rate in the DF- $\text{CO}_2$  system can be explained theoretically by assuming that the energy defect is converted to rotational energy in the DF molecules (46, 48). It is found that multiquantum changes in the rotational energy are highly probable when the strong interaction between the permanent dipole moment of DF and the quadrupole moment of  $\text{CO}_2$  is taken into account. This polar interaction, which successfully explains the favourable DF  $\rightarrow$   $\text{CO}_2$  transfer rate, is also responsible for relatively fast deactivation of the  $\text{CO}_2$   $\nu_3$  mode as discussed in section 3.2.5.

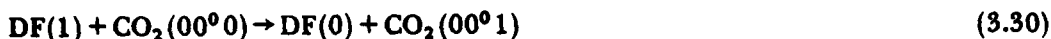
The energy transfer occurs via processes of the following type



where

$$\nu_4 > 1 \text{ and } \nu_3 > 0$$

Measurements of transfer rates have almost exclusively been made for the basic process



We denote the transfer rate constant for this process by  $k_T^0$ , and the average of several reported values yields  $k_T^0 \approx 1.5 \cdot 10^8 \text{ s}^{-1} \cdot \text{atm}^{-1}$  (44, 48). In our laser gas mixtures the  $\text{CO}_2$  partial pressure is typically 0.5 atm. This gives a transfer time of about 13 ns, which is much shorter than the duration of the pumping pulse and the  $\text{CO}_2$  laser oscillation build-up time. This means that practically all the absorbed pumping energy is stored in the  $\text{CO}_2 \nu_3$  mode at any moment in the build-up period, ensuring high laser gain. The rate constant  $k_T^0$  is among the highest that have been reported for V-V energy transfer between two different types of molecules in the gas phase. For comparison it can be mentioned that the well-known  $\text{N}_2 \rightarrow \text{CO}_2$  transfer in electric discharge excited  $\text{CO}_2$  lasers is ten times slower (49).

When the molecules become highly excited, the general processes of equation (3.29) must be taken into account. If the two vibrational modes are regarded as harmonic oscillator modes, it is still possible to describe the transfer process by simple mathematical expressions (27). The relevant equations for the DF- $\text{CO}_2$  system are discussed in Appendix C and it is found that the transfer can be described by the following rate equations in  $\bar{N}_4$  and  $\bar{N}_3$ :

$$\dot{\bar{N}}_4 = -k_T \cdot (\bar{N}_4 - \bar{N}_4^e) \quad (3.31)$$

$$\dot{\bar{N}}_3 = k_T \cdot \frac{P_{\text{DF}}}{P_{\text{CO}_2}} \cdot (\bar{N}_4 - \bar{N}_4^e) \quad (3.32)$$

Here

$$k_T = k_T^0 \cdot (1 + \bar{N}_3) \cdot P_{\text{CO}_2}$$

$$\bar{N}_4^e = \bar{N}_4^e(\Delta E, \bar{N}_3, T)$$

$P_{\text{DF}}, P_{\text{CO}_2}$  — partial pressures

We observe that the process accelerates as  $\bar{N}_3$  increases, and this is a consequence of the fact that the probability of process (3.29) increases with increasing vibrational quantum numbers (27).

Assuming that the energy exchange between the two modes is fast compared with other processes that bring energy into or out of the modes, an equilibrium between the modes can be established for  $\bar{N}_4 = \bar{N}_4^e(\Delta E, T, \bar{N}_3)$ . The equilibrium values of  $\bar{N}_4$  and  $\bar{N}_3$  are related by

$$\frac{\bar{N}_3}{1 + \bar{N}_3} = \frac{\bar{N}_4}{1 + \bar{N}_4} \cdot e^{\frac{\Delta E}{kT}} \quad (3.33)$$

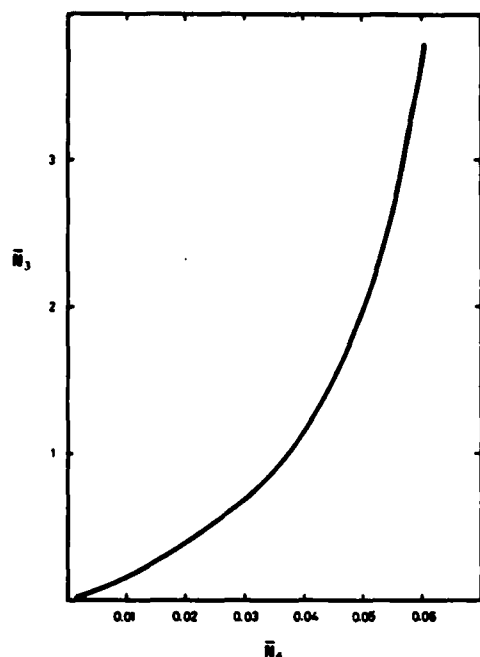


Figure 3.9 Equilibrium values of  $\bar{N}_3$  and  $\bar{N}_4$  in the internal  $V-V$  energy exchange between the DF vibrational mode and the  $\text{CO}_2$   $\nu_3$  mode

The Boltzman factor comes in as the ratio of the forward and reverse transfer probabilities. At  $T = 300$  K the equilibrium value of  $\bar{N}_3$  greatly exceeds that of  $\bar{N}_4$  as illustrated by the curve in Figure 3.9. In fact  $\bar{N}_4$  can never be greater than about 0.08 at equilibrium.

In our laser, equilibrium between  $\bar{N}_3$  and  $\bar{N}_4$  is never established due to the strong pumping of energy into the DF vibrational mode.  $\bar{N}_4$  is then always much greater than  $\bar{N}_4^e$  which can be ignored in the equations. The right side of equation (3.31) then gives the last term of equation (3.28) of the preceding section.

It can be concluded that the extremely high transfer rate and the negligible equilibrium value  $\bar{N}_4^e$  are important factors which ensure high  $\text{CO}_2$  laser gain, making this transfer laser system very attractive for high-pressure operation.

### 3.2.5 Energy relaxation processes

In this section we discuss the various  $V-V$  and  $V-T/R$  relaxation processes that occur in the gas simultaneously with pumping, energy transfer and  $\text{CO}_2$  laser oscillation. The processes were indicated in Figure 3.6, and they are obviously all detrimental to  $\text{CO}_2$  laser action with the exception of the  $V-T/R$  relaxation of the  $\nu_1$  and  $\nu_2$  modes. It should be noted that the relaxation rate  $k_x$  for any of these processes is the sum of contributions from collisions with each of the three gases

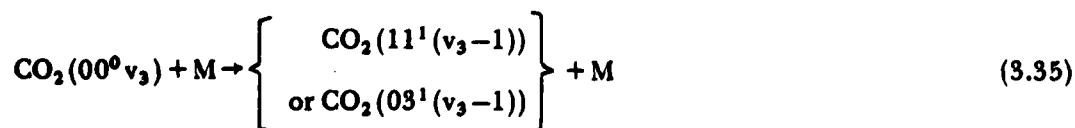
$$k_x = P_{\text{DF}} \cdot k_{x,\text{DF}}^0 + P_{\text{CO}_2} \cdot k_{x,\text{CO}_2}^0 + P_{\text{He}} \cdot k_{x,\text{He}}^0 \quad (3.34)$$

where

$k_{x,M}^0$  — specific rate constant for process  $x$  due to collisions with molecule  $M$

In the following we shall discuss the relaxation kinetics for a typical 10 atm laser gas mixture of 0.5% DF, 5%  $\text{CO}_2$  and 94.5% He.

The  $V-T/R$  relaxation rate of the DF vibrational mode is exceedingly small (44) compared with the transfer rate into the  $\text{CO}_2$   $\nu_3$  mode, and it will therefore be ignored in the model. Likewise, direct  $V-T/R$  relaxation of the  $\text{CO}_2$   $\nu_3$  mode is slow, and it is usually assumed that  $V-V$  transfer to the  $\nu_1$  and  $\nu_2$  modes is responsible for the nonradiative decay of the  $\nu_3$  mode (50). The following decay processes for the  $\text{CO}_2$   $\nu_3$  mode are usually considered as most important:



where

$M = \text{DF, CO}_2 \text{ or He}$

The energy defects of these processes are 300–400  $\text{cm}^{-1}$ . To avoid serious loss of excitation energy during the laser oscillation build-up period the decay time of the  $\nu_3$  mode should be longer than the laser oscillation build-up time.

In a similar way as for the transfer rate  $k_T$  of section 3.2.4 we might have included a dependence of  $\bar{N}_1$  and  $\bar{N}_2$  in the decay rate of the  $\nu_3$  mode (27). However, harmonic oscillator theory must be used in the derivation of the theoretical dependence, and since the levels ( $11^1(\nu_3-1)$ ) and ( $03^1(\nu_3-1)$ ) are actually strongly mixed Fermi resonance levels (see section 3.1.1), we feel that the simple theory becomes questionable. We have therefore chosen to use a fixed decay rate which we denote  $k_{D3}$  in our model.

The contributions to  $k_{D3}$  from collisions with DF,  $\text{CO}_2$  and He for the typical 10 atm laser gas mixture are given in Table 3.2.

M	$P_M$ (atm)	$k_{D3,M}^0$ ( $\text{s}^{-1} \cdot \text{atm}^{-1}$ )	$P_M \cdot k_{D3,M}^0$ ( $\text{s}^{-1}$ )	$k_{D3}$ ( $\text{s}^{-1}$ )
DF	0.05	$1.5 \cdot 10^7$	$7.5 \cdot 10^5$	$1.5 \cdot 10^6$
$\text{CO}_2$	0.5	$2.7 \cdot 10^5$	$1.4 \cdot 10^5$	
He	9.45	$8.5 \cdot 10^4$	$8.1 \cdot 10^5$	

Table 3.2 Contributions from DF-,  $\text{CO}_2$ - and He-collisions to the decay rate  $k_{D3}$  of the  $\text{CO}_2$   $\nu_3$  mode (44, 48, 51)

We observe that DF is a serious source of deactivation, and the explanation for the large rate constant is the same as for the  $\text{DF} \rightarrow \text{CO}_2$  energy transfer: Strong interaction between the permanent dipole moment of DF and the quadrupole moment of  $\text{CO}_2$  allows multiquantum changes in the rotational energy to occur, and this compensates for the energy defect of the process. Even with only 0.5% DF in the gas mixture, collisions with DF contribute with about 50% to the total relaxation rate of the  $\nu_3$  mode. The resulting decay time in the 10 atm mixture is about 670 ns, which is three times longer than the shortest build-up times that we have obtained in our

experiments. There should thus be relatively small decay losses in the build-up period. The advantage of using He as a buffer gas at high operating pressures is noticeable, since the decay rate constant for He collisions is only 1/4 of that for  $\text{CO}_2$  collisions.

A final rate equation for  $\bar{N}_3$  may now be presented which includes the energy transfer from DF, nonradiative decay of the  $\nu_3$  mode and the stimulated emission rate out of the  $\nu_3$  mode due to  $\text{CO}_2$  laser oscillation

$$N_{\text{CO}_2} \cdot \dot{\bar{N}}_3 = k_T \cdot N_{\text{DF}} \cdot \bar{N}_4 - k_{D3} \cdot N_{\text{CO}_2} \cdot \bar{N}_3 - \alpha_L \frac{I_L}{h\nu_L} \quad (3.36)$$

where

$\alpha_L$  —  $\text{CO}_2$  laser gain coefficient

$I_L$  —  $\text{CO}_2$  laser intensity



The gain coefficient  $\alpha_L$  depends on  $\bar{N}_1$ ,  $\bar{N}_2$  and  $\bar{N}_3$  (see section 3.1.4) while  $k_T$  depends on  $\bar{N}_3$  (see section 3.2.4). Note that all  $\bar{N}_i$  are functions of time and of the position in the gas cell. In section 3.2.7 we shall assume that  $I_L$  is a function of time only.

The last of the important relaxation processes in the laser gas is  $V \rightarrow T/R$  decay of the  $\nu_1$  and  $\nu_2$  modes. In some earlier extensive models for electrical discharge excited  $\text{CO}_2$  lasers (27, 52) it has been assumed that a very fast but finite  $V-V$  transfer rate  $k_{12}$  couples the  $\nu_1$  and  $\nu_2$  modes. During this energy exchange process the two modes are assumed to decay with  $V \rightarrow T/R$  rates  $k_{D1}$  and  $k_{D2}$  respectively. In our opinion this gives a questionable picture of the decay processes. As pointed out previously the  $\nu_1$  and  $\nu_2$  modes are strongly coupled through the Fermi resonance, and the resulting energy states are mixtures of the pure states of the two modes. The value that has been used for  $k_{12}$  is based upon measurements of the energy transfer rate between the two mixed levels  $(10^0 0, 02^0 0)_I$  and  $(10^0 0, 02^0 0)_{II}$  (the notation was explained in section 3.1.1). It seems obvious to us that this rate cannot be regarded as a transfer rate between the  $\nu_1$  and  $\nu_2$  modes. In our opinion the only reasonable assumption is that of a common vibrational temperature  $T_1 = T_2$  for the two modes. If this assumption is doubted, we feel that the model with characteristic vibrational temperatures will no longer be valid, and rate equations for the populations in all the involved  $\nu_1$  and  $\nu_2$  levels should be included in the model. As pointed out in section 3.1.3 recent measurements indicate that  $T_1 = T_2$  is a good approximation for electrical discharge excited  $\text{CO}_2$  lasers, and we shall therefore assume an instantaneous Boltzmann distribution at the common temperature in the  $\nu_1/\nu_2$  vibrational manifold.

The separate relaxation rates  $k_{D1}$  and  $k_{D2}$  are not meaningful in this model, and a closer study of the earlier models shows that only  $k_{D2}$  has been measured experimentally. We shall assume that the decay occurs with the rate  $k_{D2}$  via conversion of  $\nu_2$  quanta to  $T/R$  energy.

It is useful to introduce the quantity

$$\bar{N}_{12} = \bar{N}_1 + \frac{\bar{N}_2}{2} \quad (3.37)$$

which denotes the average number of "equivalent" excited  $\nu_1$  quanta stored in the  $\nu_1$  and  $\nu_2$  modes per  $\text{CO}_2$  molecule. We have then used the approximation that  $h\nu_1 = 2h\nu_2$ , so that two  $\nu_2$  quanta are "equivalent" to one  $\nu_1$  quantum. In this approximation and with  $T_1 = T_2$  we find the following relations:

$$\bar{N}_1 = \frac{1}{6} [4\bar{N}_{12} - 1 - (4\bar{N}_{12}^2 + 8\bar{N}_{12} + 1)^{1/2}] \quad (3.38a)$$

$$\bar{N}_2 = \frac{1}{3} [2\bar{N}_{12} - 1 + (4\bar{N}_{12}^2 + 8\bar{N}_{12} + 1)^{1/2}] \quad (3.38b)$$

A single rate equation in  $\bar{N}_{12}$  can now replace two rate equations in  $\bar{N}_1$  and  $\bar{N}_2$ :

$$N_{\text{CO}_2} \cdot \dot{\bar{N}}_{12} = \frac{3}{2} \cdot k_{D3} \cdot N_{\text{CO}_2} \cdot \bar{N}_3 - k_{D2} \cdot N_{\text{CO}_2} \cdot (\bar{N}_{12} - \bar{N}_{12}^e) + \alpha_L \cdot \frac{I_L}{h\nu_L} \quad (3.39)$$

where

$\bar{N}_{12}^e$  — equilibrium value of  $N_{12}$  at the T/R temperature T.

The factor 3/2 in the second terms arises from the fact that 3/2 equivalent excited  $\nu_1$  quanta are produced in the process (3.35). Knowing the time dependence of  $\bar{N}_{12}$ ,  $\bar{N}_1$  and  $\bar{N}_2$  can be calculated from equation (3.38), and these values are in turn used in the calculation of the gain coefficient  $\alpha_L$ .

M	$P_M$ (atm)	$k_{D2, M}^0$ ( $s^{-1} \cdot \text{atm}^{-1}$ )	$P_M \cdot k_{D2, M}^0$ ( $s^{-1}$ )	$k_{D2}$ ( $s^{-1}$ )
DF	0.05	—	—	
CO <sub>2</sub>	0.5	$1.1 \cdot 10^5$	$5.5 \cdot 10^4$	
He	9.45	$2.4 \cdot 10^6$	$2.3 \cdot 10^7$	
				$2.3 \cdot 10^7$

Table 3.3 Contributions from CO<sub>2</sub>- and He-collisions to the decay rate  $k_{D2}$  of the CO<sub>2</sub>  $\nu_1$  and  $\nu_2$  modes (27)

The contribution from DF is not known

The contributions to the relaxation rate  $k_{D2}$  from collisions with CO<sub>2</sub> and He are given in Table 3.3. The contribution from collisions with DF is unknown, and has been neglected in our model. The decay time becomes about 40 ns for the typical 10 atm laser gas mixture, which is about 15 times shorter than the decay time of the  $\nu_3$  mode. The favourable role of He as a deactivator for the  $\nu_1$  and  $\nu_2$  modes should be observed.

### 3.2.6 The influence of a time-dependent translational/rotational temperature

In the preceding sections we have seen that energy is transferred to the T/R degrees of freedom via direct V→T/R relaxations and via energy defects in the V–V exchange processes. An increase in the T/R temperature T must therefore be expected, and this will have significant influence on several parameters in our laser model. At present our computer model has not been extended to account for the influence of an increased T, but approximate time dependences of T are found in the calculations. The result of such a calculation for a typical 10 atm gas mixture at the input end of the gas cell is shown in Figure 3.10. The rapid increase in T from about 250 ns after the start of the pumping pulse coincides with the peak of the CO<sub>2</sub> laser pulse. The molecules are then brought rapidly into the  $\nu_1$  and  $\nu_2$  modes by stimulated emission, and fast V→T/R decay of these modes causes a rapid increase in T. The temperature increase is very modest in the laser oscillation build-up period, while the increase is more than 100 K at the end of the laser process. It will be shown at the end of this section how the approximate time dependence of T is calculated, and further results will be presented in chapter 4.

The most important effects of a temperature increase  $\Delta T$  are the following:

- a) The population probabilities  $\rho(J)$  of the rotational levels depend on  $T$ , and a larger  $T$  favours population of higher  $J$ -levels. An increase of  $\Delta T = 100$  K leads to a 5–15% reduction of  $\rho(J)$  for  $J = 16$ –22 in  $\text{CO}_2$ . The reduction in the gain for the strong  $P(16)$ – $P(22)$   $\text{CO}_2$  laser lines due to this effect is therefore not very serious. On the other hand  $\rho(J=7)$  in DF increases with about 55% for  $\Delta T = 100$  K. This leads to considerably stronger absorption of the  $1P(7)$  DF laser line, which has been used in our single-line pumping experiments.
- b) The specific Lorentz broadening coefficients are proportional to  $T^{-0.5}$  (41), while the gas pressure is proportional to  $T$ , giving a  $T^{0.5}$  dependence of the Lorentz linewidths. The exact influence on the  $\text{CO}_2$  laser gain is difficult to predict due to the complexity of the high-pressure gain spectrum as discussed in section 3.1.5. The value of the line shape factor  $g(\nu_{0p})$  at the DF absorption line centres (see equation (3.23)) is proportional to  $T^{-0.5}$ , and this will reduce the effect of increased population in the rotational levels which was discussed in a) above.
- c) There is generally an inverse temperature dependence in the rates of all the energy exchange processes that we have discussed. The rates  $k_T$ ,  $k_{D3}$  and  $k_{D2}$  decrease with about 30–50% for  $\Delta T = 100$  K (44, 27). Theoretical calculations (35) also show that a reduction of 30% in the internal V–V relaxation rate of the  $\text{CO}_2$   $\nu_3$  mode should be expected. The smaller  $k_T$  should lead to a slightly longer laser oscillation build-up time, but this effect may be compensated for by the slower decay of the  $\nu_3$  mode. Slower energy transfer may also lead to more pronounced saturation effects in the pumping process. A reduced decay rate  $k_{D2}$  will result in higher population in the lower laser level, which leads to lower laser gain.
- d) The equilibrium values  $\bar{N}_4^e$  of the transfer process (equations (3.31) and (3.32)) and  $\bar{N}_{12}^e$  of the decay of the  $\nu_1$  and  $\nu_2$  modes (equation (3.39)) will both increase for higher  $T$ . However, a  $\Delta T$  of 100 K will not affect the equilibrium populations seriously.
- e) A more serious effect than those discussed above may be the occurrence of pressure waves in the gas following the rapid increase in the gas temperature. This may lead to refractive index gradients in the gas and substantial distortions of the laser resonator mode. The speed of sound in the gas will be about 1 mm per  $\mu\text{s}$  at  $T = 300$  K and with 5%  $\text{CO}_2$  and 94.5% He in the mixture. This means that a pressure wave which starts early in the pumping process has travelled a distance of about 1 mm at the end of the pumping pulse which has a total length of more than 1  $\mu\text{s}$ . The width of the laser resonator mode is approximately 1.5 mm in our experiments, and it is therefore clear that the effect of pressure waves may be important. We have not made any further theoretical analysis of this effect, but observations made in our measurements of the laser gain seem to confirm that pressure waves may play a significant role. This will be discussed further in chapter 6. We have also observed that the tails of the measured  $\text{CO}_2$

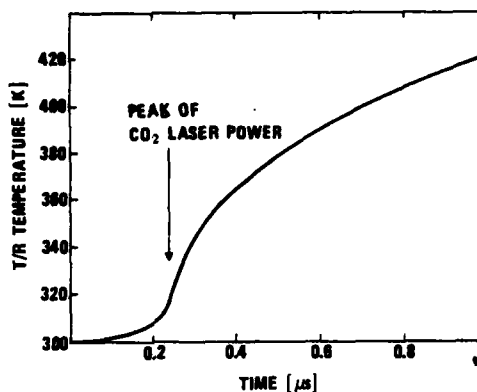


Figure 3.10 Increase in the translational/rotational temperature  $T$  during the laser process. The time of peak  $\text{CO}_2$  laser power is indicated.

laser pulses are shorter than those calculated theoretically, and this may be due to the same effect. A discussion of the importance of pressure waves in pulsed gas lasers can be found in (53).

The total influence on the laser performance from all the effects mentioned above can only be predicted by taking them all into account in the computer model. This has not been done, and it is therefore difficult to draw any further conclusions. An estimate of the importance of the effects a) – d) can be made by performing the calculations at a fixed higher temperature. The result of such a calculation for  $T = 400$  K will be presented in chapter 4. It shows relatively small deviations from the results obtained at  $T = 300$  K except for an increase in the laser oscillation build-up time. The conversion efficiency is not significantly altered. Personally we feel that the occurrence of pressure waves will be the most serious effect of the increased gas temperature.

It should be noted that optical pumping is the excitation method which provides the lowest increase in the gas temperature for a given excitation energy, because the laser molecule can be pumped selectively into the desired levels. In electrical discharge excitation of  $\text{CO}_2$  lasers a substantial part of the energy is pumped directly into the  $\nu_1$  and  $\nu_2$  modes. These modes decay rapidly, resulting in a faster increase in  $T$ .

We will now show how the approximate time dependence of  $T$  was calculated.

The T/R energy density of the gas at the temperature  $T$  is

$$U_{T/R}(T) = \left( \frac{5}{2} N_{DF} + \frac{5}{2} N_{\text{CO}_2} + \frac{3}{2} N_{\text{He}} \right) \cdot kT \quad (3.40)$$

where

$N_{DF}$ ,  $N_{\text{CO}_2}$ ,  $N_{\text{He}}$  – density of molecules/atoms.

Assume that we start at  $T = T_0 = 300$  K. We then have that  $kT_0 \cong 208 \text{ cm}^{-1}$ . The following expression gives the amount of energy  $\Delta U_{T/R}(t)$  that has been transferred to translation/rotation at the time  $t$  (pumping is assumed to start at  $t = 0$ )

$$\begin{aligned} \Delta U_{T/R}(t) \approx \int_0^t kT_0 (2.6 \cdot kT \cdot N_{DF} \cdot \bar{N}_4 + \\ 1.7 \cdot k_{D3} \cdot N_{\text{CO}_2} \cdot \bar{N}_3 + \\ 6.4 \cdot k_{D2} \cdot N_{\text{CO}_2} \cdot (\bar{N}_{12} - \bar{N}_{12}^e)) dt \end{aligned} \quad (3.41)$$

The three factors  $2.6 kT_0$ ,  $1.7 kT_0$  and  $6.4 kT_0$  are the energy defects involved in the energy transfer from DF to  $\text{CO}_2$  and in the decay of the  $\nu_3$  mode and of the  $\nu_1/\nu_2$  modes respectively. We then find the time dependence of  $T$

$$T(t) = T_0 \left( 1 + \frac{\Delta U_{T/R}(t)}{U_{T/R}(T_0)} \right) \quad (3.42)$$

The calculations are only approximate because the temperature dependence of the parameters mentioned under the items a) – d) above has been neglected. Since the speed of the different processes decreases with increasing  $T$ , we believe that the calculated temperature increase is somewhat overestimated.

### 3.2.7 Time evolution of the laser intensity

The rate equation for the time evolution of the CO<sub>2</sub> laser intensity will be the last equation in our laser model. We shall use the picture of Figure 3.11 which shows

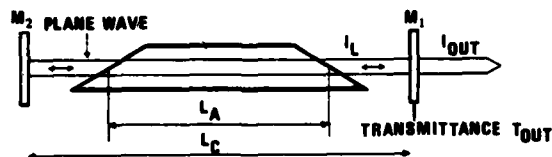


Figure 3.11 CO<sub>2</sub> laser resonator and laser field used in the theoretical model

schematically the laser gas cell and the laser mirrors M<sub>1</sub> and M<sub>2</sub>. M<sub>1</sub> is the output coupler with transmission factor T<sub>OUT</sub> at the CO<sub>2</sub> laser frequency. The cavity length and the gas cell length are L<sub>C</sub> and L<sub>A</sub> respectively. The laser resonator mode will usually be a TEM<sub>00</sub> Gaussian mode, but we simplify the picture by assuming that the laser field consists two plane counter-propagating waves between the cavity mirrors. We

also make the approximation that the laser field is constant along the resonator axis so that it only evolves as a function of time. The equation for the time dependent laser intensity  $I_L(t)$  inside the resonator can then be written as

$$\dot{I}_L(t) = c \cdot \left\{ \bar{\alpha}_L(t) + \frac{1}{2L_C} \cdot \ln(1 - \ell_R) \right\} I_L(t) \quad (3.43)$$

where

$$\bar{\alpha}_L(t) = \frac{1}{L_C} \int_0^{L_A} \alpha_L(z,t) dz \quad - \quad \text{average gain coefficient between } M_1 \text{ and } M_2$$

$$- \frac{1}{2L_C} \cdot \ln(1 - \ell_R) \quad - \quad \text{average loss coefficient}$$

$$\ell_R \quad - \quad \text{loss fraction per cavity round-trip due to output coupling, scattering in mirrors and windows, diffraction losses etc.}$$

The output intensity from the laser is found by multiplying  $I_L(t)$  with half the output coupling  $\frac{T_{OUT}}{2}$

$$I_{OUT} = \frac{T_{OUT}}{2} \cdot I_L \quad (3.44)$$

$\frac{T_{OUT}}{2}$  is used because only one of the two counter-propagating waves is coupled out at the time.

Equation (3.43) completes our mathematical laser model.

### 3.3 Summary of the laser model

In this section we make a summary of the mathematical laser model with its main assumptions and approximations.

The rate equations which describe the energy flow in the optically pumped DF→CO<sub>2</sub> transfer laser are given below. Each term in the equations is marked with a number ① which relates to a process in the energy flow diagram shown in Figure 3.12. The diagram is similar to that of Figure 3.6, but processes which have been ignored in the model are left out in Figure 3.12. The rate equations are the following (the equations are numbered with their original equation numbers in the text):

$$\frac{\partial I_p}{\partial z} + \frac{1}{c} \frac{\partial I_p}{\partial t} = -\alpha_p \cdot I_p \quad (3.27)$$

$$N_{DF} \cdot \dot{\bar{N}}_4 = \underbrace{\alpha_p \cdot \frac{I_p}{h\nu_p}}_{(1)} - \underbrace{k_T \cdot N_{DF} \cdot \bar{N}_4}_{(2)} \quad (3.28)$$

$$N_{CO_2} \cdot \dot{\bar{N}}_3 = \underbrace{k_T \cdot N_{DF} \cdot \bar{N}_4}_{(2)} - \underbrace{k_{D3} \cdot N_{CO_2} \cdot \bar{N}_3}_{(3)} - \underbrace{\alpha_L \cdot \frac{I_L}{h\nu_L}}_{(4)} \quad (3.36)$$

$$N_{CO_2} \cdot \dot{\bar{N}}_{12} = \underbrace{\frac{3}{2} k_{D3} \cdot N_{CO_2} \cdot \bar{N}_3}_{(3)} - \underbrace{k_{D2} \cdot N_{CO_2} \cdot (\bar{N}_{12} - \bar{N}_{12}^e)}_{(5)} + \underbrace{\alpha_L \cdot \frac{I_L}{h\nu_L}}_{(4)} \quad (3.39)$$

$$\dot{I}_L = \underbrace{c \cdot \bar{\alpha}_L \cdot I_L}_{(6)} + \underbrace{\frac{c}{2L_C} \cdot \ln(1 - \ell_R) \cdot I_L}_{(7)} \quad (3.43)$$

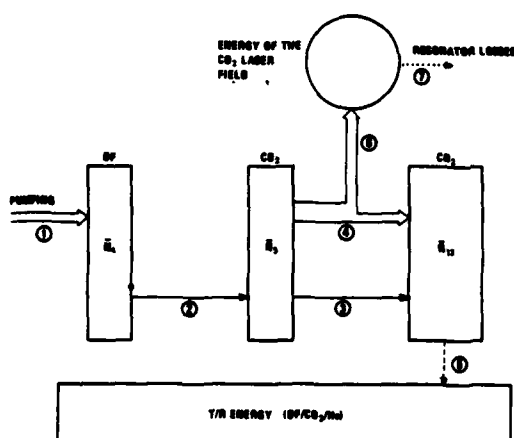


Figure 3.12 The energy flow in the optically pumped DF  $\rightarrow$  CO<sub>2</sub> transfer laser  
The numbers in circles indicate the correspondence with terms in equations (3.27) ... (3.43) in the text

The variables  $I_p$ ,  $\alpha_p$ ,  $\alpha_L$ ,  $\bar{N}_4$ ,  $\bar{N}_3$ ,  $\bar{N}_{12}$ ,  $k_T$  are all functions of  $t$  and  $z$  (position along the resonator axis), while  $I_L$  and  $\bar{\alpha}_L$  are functions of  $t$  only. Remember that  $\alpha_p$ ,  $\alpha_L$  and  $k_T$  are functions of the  $\bar{N}_i$ .  $\bar{N}_{12} = \bar{N}_1 + \bar{N}_2/2$ , and  $\bar{N}_1$  and  $\bar{N}_2$  are explicit functions of  $\bar{N}_{12}$  for a common vibrational temperature  $T_1 = T_2$  of the  $\nu_1$  and  $\nu_2$  CO<sub>2</sub> vibrational modes (see equation (3.38)).

The pumping radiation intensity  $I_p$  ( $z = 0$ ,  $t$ ) at the input end of the gas cell will be used as an input to the equations in the computer calculations. Initial values of all the other variables will be thermal equilibrium values at  $T = 300$  K.

The main assumptions and approximations in the laser model are the following:

- Statistical equilibrium at a common temperature  $T$  always exists within the translational and rotational degrees of freedom in DF, CO<sub>2</sub> and He (see sections 3.1.3 and 3.2.2).
- Statistical equilibrium always exists within each of the vibrational modes in DF and CO<sub>2</sub>, with a characteristic vibrational temperature  $T_i$  for mode number  $i$ . This assumption is questionable with respect to the DF vibrational mode where the internal V-V relaxation rate is in the same order of magnitude as the pumping rate and energy transfer rate to CO<sub>2</sub> (sections 3.1.3 and 3.2.2).

- c)  $T_1 = T_2$  is assumed because of the strong Fermi resonance coupling between the  $\nu_1$  and  $\nu_2$  modes in  $\text{CO}_2$  (sections 3.1.3 and 3.2.5).
- d) Decoupling of the rotational and vibrational partition functions and ideal harmonic oscillator vibrational modes are assumed in the calculation of the population probabilities (sections 3.1.3 and 3.2.2).
- e) Several energy exchange processes which are assumed to be of minor importance are ignored (section 3.2.5).
- f) The influence of a time dependent T/R temperature T on several parameters in the laser model has been discussed, but it is neglected in the computer model. The errors that occur because of this approximation are difficult to predict, but they seem not to be serious (section 3.2.6 and chapter 4).
- g) The influence of pressure waves has not been taken into account in the model, and this may be a serious limitation (section 3.2.6 and chapter 6).
- h) The  $\text{CO}_2$  laser field is assumed to consist of two counter-propagating plane waves which experience an average gain and an average loss per unit time. Variations in the laser intensity along the resonator axis are neglected (section 3.2.7). The pumping laser field is also assumed to be a plane wave (section 3.2.3).
- i) The contributions to the  $\text{CO}_2$  laser gain from line overlapping and from the sequence bands are taken into account in the model (section 3.1.5).
- j) The influence of interactions between overlapping  $\text{CO}_2$  laser lines has not been analysed (section 3.1.5).
- k) The fine structure of the sequence bands is ignored in the calculation of their contribution to the  $\text{CO}_2$  laser gain (section 3.1.5).

The two last effects will be important for the frequency tuning characteristics of the laser. Finally it should be mentioned that only single line pumping is treated in the calculations.

#### 4 COMPUTER SIMULATIONS OF THE LASER

In this chapter some selected results from the computer simulations of the laser will be presented.

A complicating factor in the solution of the equations is the fact that several of the variables depend both on time  $t$  and on position  $z$  in the laser gas cell. The gas cell used in our experiments is 10 cm long, and in the computer calculations the  $z$ -axis has been divided into eleven discrete positions  $z = 0$  cm,  $z = 1$  cm, ...,  $z = 10$  cm in the gas cell ( $z = 0$  at the end where the pumping radiation enters the gas cell). Each variable  $f(z, t)$  is then replaced by eleven new variables  $f(z = 0, t)$ , ...,  $f(z = 10, t)$ , each of which can be described by a differential equation in time only. In this approximation the model contains about 80 differential equations in time, and these have been solved on a Nord 10 computer using Gear's method for the numerical solution. Gear's method is particularly well suited for sets of equations where there are large variations in the coefficients of the equations, which is the case in this problem.

It should be mentioned that the laser model has become far more extensive than we intended when we started to work on it, and it is clear that the small Nord 10 computer is not well suited for the solution of this large system of equations. Several hours of computer processing time is required for each set of input data to the program, and at present the system has only been solved for a few selected choices of laser operating conditions. It is our intention to transfer the computer program to a larger computer, and that will also allow further extensions of the model. It will for instance be possible to take into account the influence of a time dependent  $T/R$  temperature  $T$  on the different parameters in the model as discussed in section 3.2.6.

In all the calculations it has been assumed that the 1P(7) DF laser line is used for pumping, and a pumping pulse shape of the following type has been chosen

$$I_p = I_{0p} \cdot (e^{-k_1 t} - e^{-k_2 t}) \quad (4.1)$$

where

$$k_1 = 2.5 \cdot 10^6 \text{ s}^{-1}$$

$$k_2 = 1.0 \cdot 10^8 \text{ s}^{-1}$$

This pulse shape reproduces the envelope of the experimental pulse fairly well (see section 5.2.2).  $I_{0p}$  is a variable input parameter to the program, and in most of the calculations it has been assumed that  $I_{0p} = 1.4 \cdot 10^{26} \text{ photons} \cdot \text{cm}^{-2} \cdot \text{s}^{-1}$ . This corresponds to a pumping energy of 60 mJ distributed uniformly over a  $0.02 \text{ cm}^2$  cross-section. 60 mJ is a typical value for the pumping energy used in the experiments. The beam cross-section has only been roughly estimated. It should be emphasized that our assumption of a plane pumping wave of uniform intensity may lead to significant errors in the calculated results, but this has not been analyzed further. (See chapter 5 for further details about pumping energies and beam cross-sections.)

All the examples are given for 10 atm  $\text{CO}_2$  laser gas mixtures, assuming that the  $\text{CO}_2$  laser oscillates on the R(18) line at  $975 \text{ cm}^{-1}$ . The values of several parameters in the equations have been given in section 3.2, and these are summarized together with other necessary data in Appendix D. Apart from  $I_{0p}$  the main input parameters to the program are the round trip resonator losses  $\ell_R$ , the output coupling  $T_{\text{OUT}}$  and the partial pressures  $p_{\text{DF}}$ ,  $p_{\text{CO}_2}$  and  $p_{\text{He}}$ .



The following variables are calculated in the simulations:

$I_p(z, t)$	— pumping radiation intensity (photons·cm <sup>-2</sup> ·s <sup>-1</sup> )
$I_L(t)$	— CO <sub>2</sub> laser intensity (photons·cm <sup>-2</sup> ·s <sup>-1</sup> )
$I_{OUT}(t)$	— $\frac{T_{OUT}}{2} \cdot I_L(t)$ (photons·cm <sup>-2</sup> ·s <sup>-1</sup> )
$\bar{N}_i(z, t), i=1, \dots, 4$	— average number of excited $\nu_i$ quanta per molecule
$\alpha(z, t)$	— CO <sub>2</sub> laser gain coefficient (% per cm)
$\bar{\alpha}(t)$	— average gain coefficient (% per cm)
$T(z, t)$	— the T/R temperature (K)
$\eta$	— quantum efficiency ( $\int I_{OUT}(t)dt : \int I_p(t)dt$ )

The intensities are given in units of (photons·cm<sup>-2</sup>·s<sup>-1</sup>) because we then get a direct picture of the quantum efficiency when comparing  $I_p(t)$  and  $I_{OUT}(t)$ .  $T = 300$  K is chosen as initial gas temperature, and initial values of  $\bar{N}_i$  are calculated at this temperature. It is assumed that CO<sub>2</sub> laser oscillation starts from one photon which is emitted spontaneously in the  $z$ -direction of the laser. The initial value  $I_L(0)$  is taken as the intensity of a laser field which has the energy of one CO<sub>2</sub> laser photon distributed uniformly in the laser resonator mode.

In Figure 4.1 we present some examples of the calculated time dependences of the variables. Variables which depend on  $z$  are only given for  $z = 0$  as indicated in the figure. The calculations are made for a 10 atm gas mixture containing 0.6% DF, 5% CO<sub>2</sub> and 94.4% He, and for  $\ell_R = 6\%$ ,  $T_{OUT} = 3.5\%$  and  $I_{0p} = 1.4 \cdot 10^{26}$  photons·cm<sup>-2</sup>·s<sup>-1</sup>. Unless otherwise stated  $\ell_R$ ,  $T_{OUT}$  and  $I_{0p}$  will have the same values for all examples in this chapter.  $T_{OUT} = 3.5\%$  corresponds to the output coupling used in our experiments, and this leaves 2.5% for other resonator losses ( $\ell_R - T_{OUT} = 2.5\%$ ).

It is observed that the build-up time of  $I_{OUT}$  is about 220 ns, and the peak of  $I_{OUT}$  exceeds the peak of  $I_p$  by a factor of 2. The quantum efficiency  $\eta$  is about 46%, and it can be mentioned that most of the reduction in quantum efficiency is due to the loss factor  $\ell_R - T_{OUT} = 2.5\%$ . The maximum possible quantum efficiency  $\eta_{max}$  for a given  $\ell_R$  can be found by multiplying  $\eta$  by the factor  $\ell_R/T_{OUT}$ . This is the quantum efficiency that would be obtained for  $T_{OUT} = \ell_R$ . In this case we find that  $\eta_{max}$  is close to 80%, showing that the decay of the CO<sub>2</sub>  $\nu_3$  mode is not critical for the efficiency.

The CO<sub>2</sub> laser gain  $\alpha$  at  $z = 0$  is as high as 9% per cm just before it is saturated by the CO<sub>2</sub> laser pulse. The round trip gain  $2L_C \bar{\alpha}$  at the same point of time is about 43%, showing that the laser is excited far above threshold. It can be observed that equality between round trip gain and round trip losses ( $2L_C \bar{\alpha} = \ell_R = 6\%$ ) is established during the tail of the laser pulse. The saturation of the population inversion is observed in the rapid decay of  $\alpha$ ,  $2L_C \bar{\alpha}$  and  $\bar{N}_3$  and in the corresponding rise of  $\bar{N}_1$ . For the maximum value of  $\bar{N}_3$  of about 0.6 the laser gain including the contribution from the sequence bands is 2.6 times higher than the gain on the regular laser bands (see equation (3.17)). This demonstrates the importance of including the sequence bands in the theory of the laser. The dip of  $\bar{N}_4$  is due to the fact that rate  $k_T$  for the energy transfer from DF to CO<sub>2</sub> is proportional to  $1 + \bar{N}_3$  (see equation (3.31)). When  $\bar{N}_3$  is depleted by the CO<sub>2</sub> laser pulse, the transfer process slows down, and  $\bar{N}_4$  increases for a short period. A considerable saturation in the absorption of the pumping radiation will obviously occur, since  $\bar{N}_4$  is as large as 0.35 – 0.40 at the maximum (see also section 3.2.3).

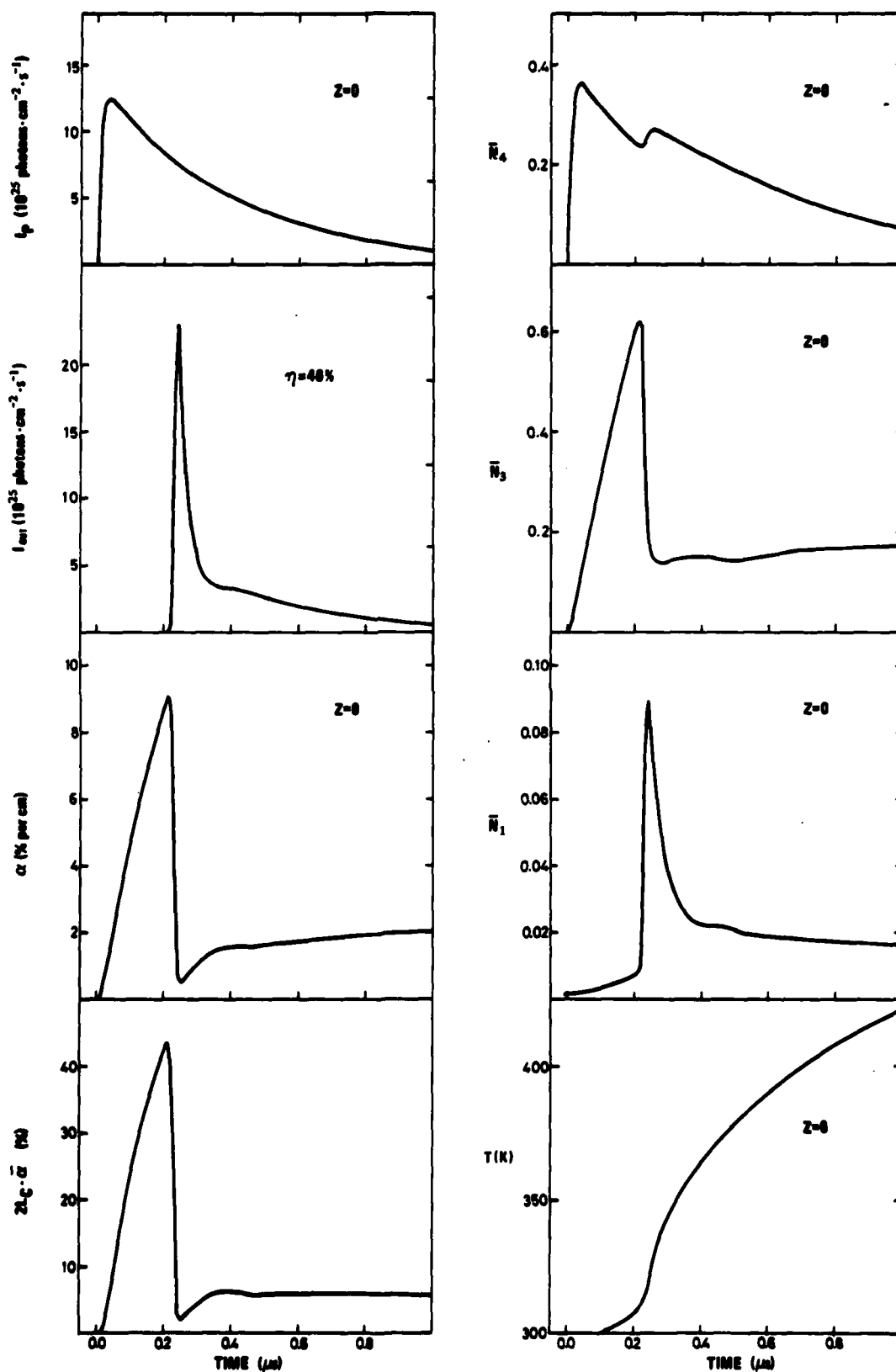


Figure 4.1 Calculated time dependences of variables in the laser model  
(Parameter values used in the calculations are given in the text)

The last variable in Figure 4.1 is the T/R temperature  $T$  which increases by more than 100 K during the laser process. As explained in section 3.2.6 the increase is particularly fast in the period of high  $\text{CO}_2$  laser intensity.

These calculations have been performed for five different 10 atm laser gas mixtures with the given values of  $I_{0P}$ ,  $T_{OUT}$  and  $l_R$ . The mixtures are the following:

- a) —
- b) 0.4% DF, 5.0%  $\text{CO}_2$ , 94.6% He
- c) 0.6% DF, 5.0%  $\text{CO}_2$ , 94.4% He (described above)
- d) 1.1% DF, 5.0%  $\text{CO}_2$ , 93.9% He
- e) 0.6% DF, 2.0%  $\text{CO}_2$ , 97.4% He
- f) 0.6% DF, 13.3%  $\text{CO}_2$ , 86.1% He

The notation a, b ... is identical to the notation used in section 6.2 for the same gas mixtures used in the experiments. No calculated data exist for mixture a of section 6.2. Almost identical  $\text{CO}_2$  laser pulse shapes  $I_{OUT}$  and quantum efficiencies  $\eta$  were calculated for all these mixtures, even though there were large differences in the  $z$ -dependences of some of the variables. The  $z$ -dependences of  $I_P$ ,  $\alpha$  and  $T$  are shown in Figures 4.2, 4.3 and 4.4 for the points of time when they have their maxima.

It can be observed that the pumping radiation is almost entirely absorbed for all the gas mixtures, and the  $z$ -dependence of  $I_P$  is reflected in the dependences of  $\alpha$  and  $T$ . It appears that variations in the  $\text{CO}_2$  partial pressure (c, e, f) have much smaller influence on the variables than variations in the DF partial pressure (b, c, d). This may be explained by the fact that while an increased  $\text{CO}_2$  partial pressure leads to

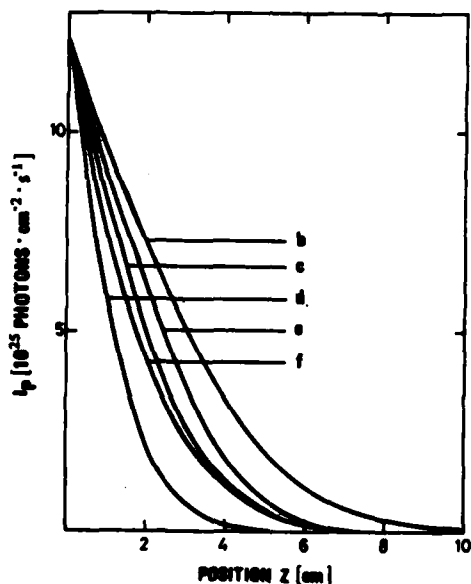


Figure 4.2 Calculated  $z$ -dependences of the pumping radiation intensity  $I_P$  at the time of maximum  $I_P$

The letters b ... f denote different gas mixtures (see text)

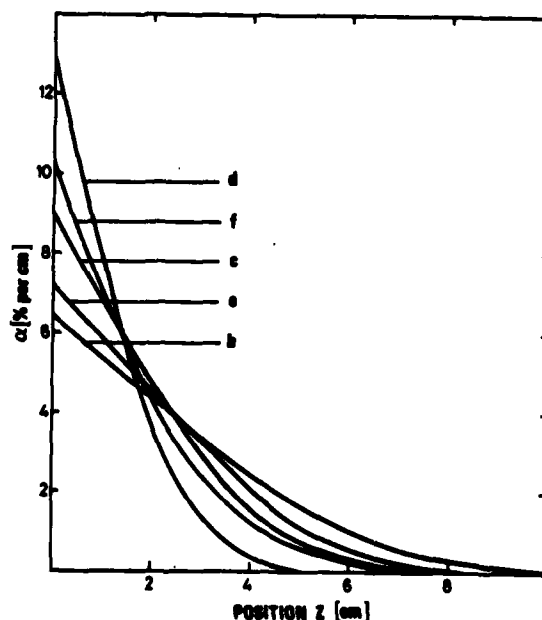


Figure 4.3 Calculated  $z$ -dependences of the laser gain coefficient  $\alpha$  at the time of maximum  $\alpha$

The letters b ... f denote different gas mixtures (see text)

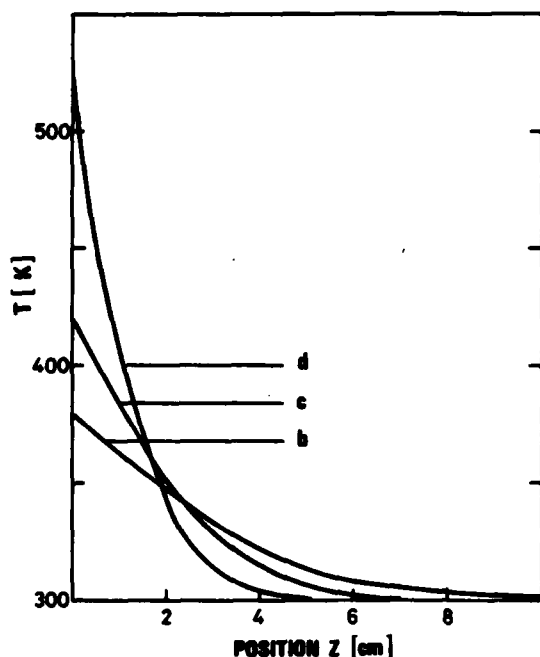


Figure 4.4 Calculated  $z$ -dependences of the T/R temperature  $T$  at  $t = 1 \mu\text{s}$  after the start of pumping

The letters b, c and d denote different gas mixtures (see text).

are identical to those of Figure 4.1, and the laser pulse of Figure 4.1 is shown for comparison (a). It has been pointed out earlier that an increase in the T/R temperature leads to significant changes in several parameters in the laser model. In the calculation leading to the result of Figure 4.5b parameter values for a fixed temperature  $T = 400 \text{ K}$  have been used. We observe a significant increase in the laser oscillation build-up time, but the efficiency is only slightly altered. Considering the temperature evolution in Figure 4.1 it is clear that the assumption of a constant  $T = 400 \text{ K}$  is drastic. In particular,  $T$  increases very slowly in the build-up period, and a significant influence on the build-up time should actually not be expected. It therefore seems that the laser performance will only be slightly affected by changes in the parameters due to an increased temperature. It was mentioned in section 3.2.6 that formation of pressure waves caused by the temperature rise might be more serious, and this will be discussed in chapter 6.

In Figure 4.5c  $I_{0p}$  has been increased by a factor of two to  $2.8 \cdot 10^{26} \text{ photons} \cdot \text{cm}^{-2} \cdot \text{s}^{-1}$ . All other parameters are as in Figure 4.5a. The most important changes from Figure 4.5a are the shorter build-up time and higher concentration of energy in the pulse tail. The quantum efficiency is only slightly increased, because the laser is operated far above the threshold in both cases. It should be noted that the efficiencies and peak intensities could have been increased considerably in these examples by using a higher output coupling  $T_{OUT}$  which could dominate over the other resonator losses. Such an optimization can always be made when the laser is excited far above the threshold.

The resonator losses other than the output coupling ( $\ell_R - T_{OUT}$ ) of our experiments have only been tentatively estimated. Some of the results presented in chapter 6 indicate that the losses used in these calculations are considerably lower than those of our laser. Results of calculations made with higher losses will be presented in chapter 6 in connection with the discussion of the experimental data.

faster energy transfer, it also gives lower absorption coefficients for the pumping radiation through increased broadening of the DF absorption lines (see section 3.2.3). These two effects may to some degree compensate for each other, leading to only small changes in the absorption.

Looking at the  $z$ -dependence of the gain  $\alpha$  we observe that the total single-pass gain is approximately the same for all the mixtures, which is natural since almost the whole pumping energy is absorbed. It is therefore not surprising that approximately the same  $\text{CO}_2$  laser pulse shapes and quantum efficiencies are obtained in all cases. The fact that the quantum efficiencies are negligibly influenced by changes in the gas mixture seems to confirm that decay of the  $\text{CO}_2 \nu_3$  mode plays a secondary role as a loss mechanism in the laser.

In Figure 4.5 it is shown how  $I_{OUT}$  and  $\eta$  is affected by changes in the T/R temperature  $T$  (b) and in  $I_{0p}$  (c). The gas mixture,  $T_{OUT}$  and  $\ell_R$

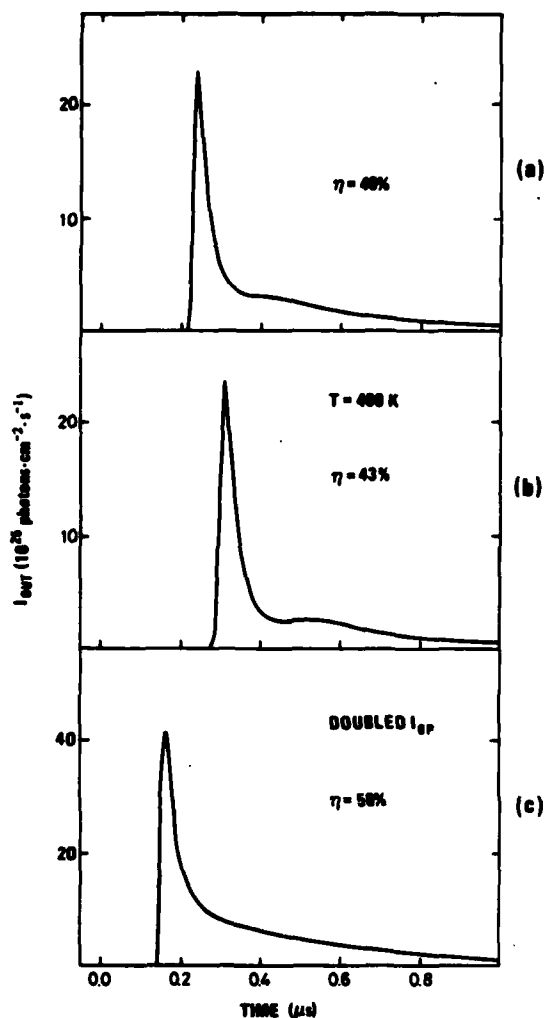


Figure 4.5 Calculated time dependences of the  $\text{CO}_2$  laser output intensity  $I_{\text{OUT}}$

- a) Parameter values as in Figure 4.1 (parameters calculated at  $T = 300 \text{ K}$ ,  $I_{\text{OP}} = 1.4 \cdot 10^{26} \text{ photons} \cdot \text{cm}^{-2} \cdot \text{s}^{-1}$ )
- b) Parameters calculated at  $T = 400 \text{ K}$  (other conditions as in a)
- c)  $I_{\text{OP}} = 2.8 \cdot 10^{26} \text{ photons} \cdot \text{cm}^{-2} \cdot \text{s}^{-1}$  (other conditions as in a)

It has been mentioned earlier in this chapter that saturation will occur in the absorption of the pumping radiation. Figure 4.6 illustrates how the saturation influences the shape of the transmitted pumping pulse in gas mixture c. The incident and transmitted pumping pulses are shown in the figure, and we observe a substantial sharpening in the transmitted pulse. This occurs because the strongest saturation is experienced at the peak of the pulse. Such saturation effects have also been observed in our experiments, and they will be discussed in chapter 6.

The saturation of the absorption may be even stronger than the computer calculations show, because the assumption of a Boltzmann distribution in the DF vibrational ladder becomes questionable for the high pumping radiation intensities that we use. For the gas mixture and  $I_{\text{OP}}$  of Figure 4.6 we find that the characteristic time of change in  $\bar{N}_4$  due to pumping

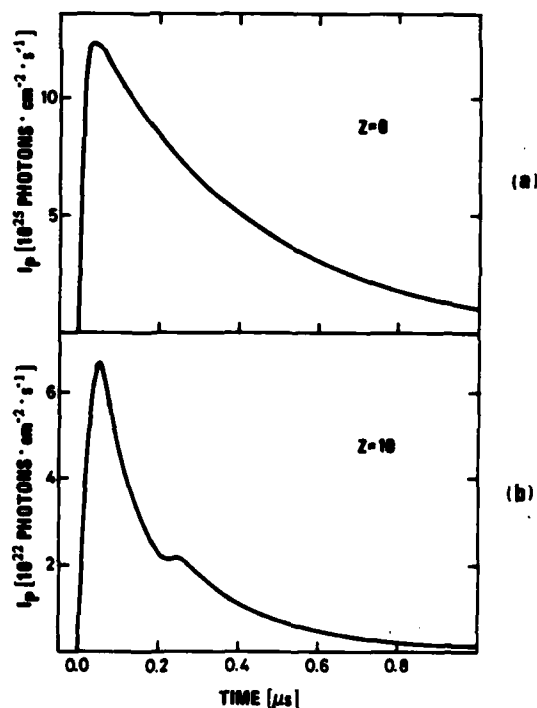


Figure 4.6 Saturation effects in the pumping pulse shape

- a) Incident pumping pulse
- b) Transmitted pumping pulse

will be about 10 ns at the peak of the pumping pulse. The internal relaxation time within the DF vibrational ladder will be in the order of 20 ns according to the rate given in section 3.2.2. It is therefore probable that a deviation from a Boltzmann distribution will occur during a part of the pumping process, which will make the saturation even more pronounced.

## 5 DESCRIPTION OF THE EXPERIMENTS

In this chapter we describe the experimental techniques used for optical pumping of the high-pressure DF $\rightarrow$ CO<sub>2</sub> transfer laser, and the characteristics of the DF pumping laser in single-line and multiline operation are also given. Most of the experiments were performed with a simple two-mirror DF $\rightarrow$ CO<sub>2</sub> transfer laser resonator. Some selected experiments were performed in order to demonstrate continuous tuning of the laser frequency, and a description of the resonator configurations with spectral characteristics of the tuning elements is given in the last section of this chapter.

We shall take the opportunity at this point of making some comments on the development of the experimental work, which are relevant also for the presentation of the results in chapter 6. In retrospect it often appears that a different relative weight on the various types of experiments would have been more logical, and that more extensive measurements and higher accuracy would have been desirable. So it is the case also in this work which gave too little room for experiments with single-line pumping of the DF $\rightarrow$ CO<sub>2</sub> transfer laser.

At the start of the experimental work it was believed that multiline pumping would give the best results because higher pumping energies were available than in single-line pumping. A substantial part of the time was therefore used on multiline pumping experiments. We believed that it was particularly important to find the optimum DF/CO<sub>2</sub>/He gas mixtures at various total gas pressures and pumping energies, and a large number of measurements were made for a variety of gas mixtures. Unfortunately, several difficulties during the work made this optimization very uncertain. First of all, the reactive nature of the DF gas made it difficult to determine the exact DF partial pressures from time to time. Components in the gas mixing system and procedures for preparation of gas mixtures had to be changed several times due to these problems, and results obtained before and after such changes could differ significantly and often unpredictably. Another major concern was damage to the mirrors and Brewster windows in the optically pumped laser due to the high power densities of the pumping laser pulse. It was always difficult to decide whether such damage could be responsible for changes in the laser performance. The multiline DF laser was operated with a stable laser resonator, and the laser then gave a multi-transversal-mode output beam. The irregular mode pattern of this beam increased the problems with radiation damage. Besides, the multimode pumping beam could not be effectively matched to the TEM<sub>00</sub> resonator mode of the optically pumped laser, as we shall see later. For these reasons and reasons to be mentioned later, the experimental uncertainties became too large to allow a definite optimization of the gas mixture. We also found that the interpretation of the results and comparison with theory became extremely difficult in the case of multiline pumping, since as much as 25 pumping lines were involved with highly differing absorption coefficients for the different lines. Low absorption of many of the pumping lines was also unfavourable (refer to Figure 3.7).

Improved transversal mode quality can be obtained by using an unstable DF laser resonator, and it was therefore decided to perform experiments with such a resonator. Single-line operation was chosen in these experiments because that resulted in much stronger absorption of the pumping radiation. The same amount of absorbed pumping energy could be obtained for a much lower input pumping energy, and that reduced the radiation damage problems considerably. The interpretation of the results also became much easier when a single pumping line was used. To our surprise we obtained single-line pumping energies which were twice as high as the energies stated by the manufacturer of the DF laser, and the single-line DF laser thus became a very attractive pumping source.

Since a large period of time had already been spent on the multiline pumping experiments, we decided to concentrate the single-line pumping experiments at 10 atm gas

pressure, which is sufficient for overlapping between adjacent  $\text{CO}_2$  laser lines. The results of these experiments were considerably more reliable since we at that time had learned better how to control the DF partial pressure and because the problems with radiation damage on mirrors and windows were less troublesome.

It would have been preferable to perform a more extensive series of single-line pumping measurements than those presented here, but nevertheless we feel that our results give a good picture of the high-pressure operation characteristics of the  $\text{DF} \rightarrow \text{CO}_2$  transfer laser system. The laser pulses that we have obtained also compare reasonably well with the results of our computer calculations.

We have chosen to put approximately equal weight on the description of the single-line and multiline pumping experiments. The results obtained with multiline pumping have considerably larger uncertainties, and the complexity of the pumping process makes it very difficult to compare the results with theoretical models. Nevertheless, it turned out that multiline pumping produced approximately the same output energies as those obtained with single-line pumping, and we feel that the results may be valuable, because it is not yet clear which of the pumping schemes will be preferred in a practical laser system.

### 5.1 Configurations of the laser experiments

A schematic of the experimental set-up used for the single-line pumping of the  $\text{DF} \rightarrow \text{CO}_2$  transfer laser is shown in Figure 5.1. For illustration we have included typical oscillograms of the single-line pumping pulse and the  $\text{CO}_2$  laser pulse obtained at 10 atm gas pressure. A slightly different set-up was used in most of the multiline pumping experiments, and we shall return to that later in this section. The configurations used in the frequency tuning experiments will be described in section 5.7.

This section briefly describes the various parts of the experimental configuration with the exception of the pumping laser which is treated in section 5.2. For simplicity we shall hereafter use the notation OPL for the optically pumped laser.

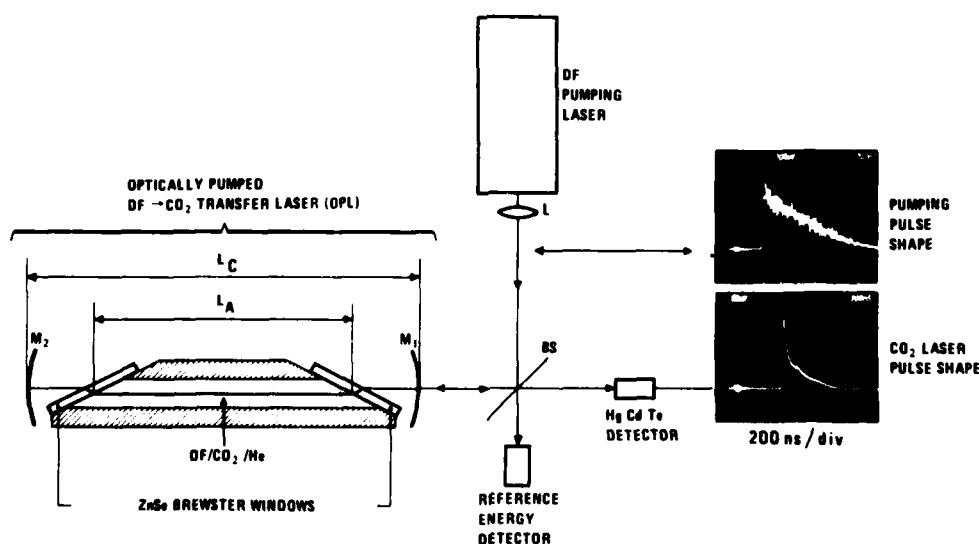


Figure 5.1 Experimental configuration of the optically pumped two-mirror  $\text{DF} \rightarrow \text{CO}_2$  transfer laser (configuration used in single-line pumping experiments).



MIRROR RADII OF CURVATURE	$R_1 = R_2 = 30 \text{ cm}$
INTERNAL GAS CELL LENGTH	$L_A = 10 \text{ cm}$
TOTAL OPTICAL RESONATOR LENGTH	$L_C = 22 \text{ cm}$
SPECTRAL PROPERTIES OF BEAMSPLITTER	$R > 99\% \text{ @ } 2743 \text{ cm}^{-1} \text{ }^{\text{a}}$ $T = 80\% \text{ @ } 975 \text{ cm}^{-1} \text{ }^{\text{aa}}$
SPECTRAL PROPERTIES OF MIRROR $M_1$	$T > 90\% \text{ @ } 2743 \text{ cm}^{-1}$ $T = 3.5\% \text{ @ } 975 \text{ cm}^{-1}$
SPECTRAL PROPERTIES OF MIRROR $M_2$	$T = 1\% \text{ @ } 2743 \text{ cm}^{-1}$ $T = 0.5\% \text{ @ } 975 \text{ cm}^{-1}$

<sup>a</sup> Frequency of the 1P(7) pumping line

<sup>aa</sup> The  $\text{CO}_2$  laser oscillated in the R-branch at  $975 \text{ cm}^{-1}$  at high gas pressure

Tabell 5.1 Data for the laser resonator and the optical components of Figure 5.1

T – transmittance R – reflectivity

The high pressure  $\text{DF}/\text{CO}_2/\text{He}$  mixture is contained in the OPL gas cell which has 10 mm thick ZnSe Brewster windows. The pumping radiation is focused into the gas cell by the lens L via the beamsplitter BS. The  $\text{CO}_2$  laser radiation is coupled out through the laser mirror  $M_1$  and passes through the beamsplitter. Some important data for the optical components and the laser resonator are summarized in Table 5.1.

With equal mirror radii of curvature the beamwaist of the OPL  $\text{TEM}_{00}$  resonator mode falls at the centre of the OPL cavity, and the focus of the pumping beam is placed at the same point. The choice of mirror radii and focal length of the lens L is important with respect to matching between the excited gas volume and the OPL resonator mode, and this will be discussed further in section 5.3.

An internal gas cell length of  $L_A = 10 \text{ cm}$  gave a suitable absorption of the pumping radiation, and this length was used in nearly all the experiments. A 20 cm cell was tested in the multiline pumping experiments for enhancement of the absorption, but due to poorer matching between the pumping beam and the OPL resonator mode, it did not lead to improved results.

The spectral characteristics of the beamsplitter and the input mirror at the pumping laser frequencies and at the  $\text{CO}_2$  laser frequencies satisfy fairly well the general requirements that were stated in section 2.1.2. From the data of Table 5.1 we observe that the loss in pumping power at the input mirror is less than 10%, while about 20% of the  $\text{CO}_2$  laser power is lost at the beamsplitter. The transmission factors for the  $\text{CO}_2$  laser radiation are given at  $975 \text{ cm}^{-1}$  because the  $\text{CO}_2$  laser oscillated in that frequency region in most of our experiments. Detailed spectral curves for the components are given in Appendix E. The input mirrors were coated by Christian Holm in our own coating laboratory, and we are greatly indebted to Christian, because none of the coating companies that we were in contact with were able to produce coatings with the required spectral characteristics.

The rear laser mirror  $M_2$  is primarily intended to serve as a total reflector for the OPL radiation. We also observe that  $M_2$  has a high reflectivity at the pumping laser frequencies, and this means that the pumping energy which is transmitted through the gas cell is reflected back into the gas cell. This is favourable with respect to excitation of the gas, but it makes it more difficult to determine the exact amount of absorbed pumping energy. In the case of multiline pumping the reflected pumping beam is

highly diverging relative to the OPL resonator mode, and we have chosen to ignore the contribution to the excitation from the reflected pumping power. In single-line pumping, on the other hand, almost 100% of the transmitted pumping power is reflected back into a volume which closely matches the OPL resonator mode. In addition 80–95% of the pumping energy is absorbed in the first pass through the cell, and we may therefore assume that all the incident pumping energy contributes effectively to the excitation in this case. The difference between the two cases will become clearer after the discussion of mode matching in section 5.3.

It should be noted that the choice of output coupling at  $M_1$  is important for efficient extraction of  $\text{CO}_2$  laser energy. To avoid reduction in conversion efficiency the output coupling should be the dominating loss factor in the resonator. We estimate that the round trip resonator losses due to absorption and scattering in mirrors and Brewster windows and transmission in the rear mirror  $M_2$  may be of about the same magnitude as the 3.5% output coupling given in Table 5.1. In the calculations of chapter 4 a round trip resonator loss  $\ell_R$  of 6% was assumed, leading to a maximum possible quantum efficiency of about 60%. It was important for us to keep the resonator parameters as constant as possible throughout the many measurements that involved variation in gas mixture, gas pressure and pumping energies, and we therefore did not try to optimize the output coupling for maximum output energies in these experiments. Selected experiments have however been made with increased output coupling, and they showed that increased output energies could be obtained. This will be discussed further in chapter 6. (The results of chapter 6 also indicate that the round trip resonator losses are considerably higher than 6%.)

It was mentioned above that a slightly different experimental configuration was used in most of the multiline pumping experiments, and a schematic of the configuration

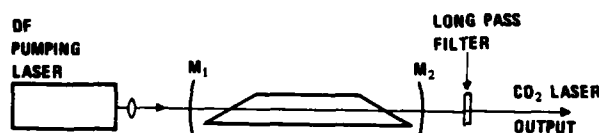


Figure 5.2 Alternative experimental configuration used in most of the multiline pumping experiments

MIRROR $M_1$	{	T > 90% @ 2500 – 2900 $\text{cm}^{-1}$ *
		T = 1.2% @ 975 "
MIRROR $M_2$	{	T = 4–35% @ 2500 – 2900 "
		T = 3.2% @ 975 "
FILTER F	{	T = 0 @ 2500 – 2900 "
		T = 62% @ 975 "

\* Frequency range of the multiline pumping laser

Table 5.2 Data for the laser resonator and the optical components of Figure 5.2

is shown in Figure 5.2. Instead of using a beamsplitter as in Figure 5.1, the  $\text{CO}_2$  laser radiation is coupled out through the mirror  $M_2$ , and it travels in the same direction as the pumping beam. A longpass filter F is then used to block the transmitted DF laser radiation. The spectral characteristics of  $M_1$ ,  $M_2$  and F are summarized in Table 5.2. It can be observed that the total spectral properties of the OPL resonator are only slightly different from those of the set-up in Figure 5.1. The output coupling is approximately the same, but there is about 1% higher transmission loss in  $M_1$  than we had in  $M_2$  in Figure 5.1. We also observe that there is a higher transmission loss in the filter F at  $\text{CO}_2$  laser frequencies than in the beamsplitter of Figure 5.1. The other parameters are identical to those of Figure 5.1.

The equipment used for analysis of the laser performance includes the following instruments:

- a) Two pyroelectric energy detectors are used. One of these is a reference detector which monitors the pumping energy (see Figure 5.1). The other detector measures the CO<sub>2</sub> laser energy.
- b) A HgCdTe detector with rise time less than 1 ns measures the pulse shapes.
- c) A grating spectrometer with 0.08–0.09 cm<sup>-1</sup> resolution at CO<sub>2</sub> laser frequencies is used for spectral analysis of the laser output.
- d) In a short period a pyroelectric vidicon was available for monitoring of the transversal mode patterns of the laser beam.

These instruments have also been used for analysis of the DF pumping laser performance which is the subject of the next section.

The absorbed pumping energy is measured by an energy detector placed in the position of M<sub>2</sub>. The detector signal is then observed with and without the gas cell in the beam, and the difference gives the absorbed energy. In multiline pumping only 20–25% of the total input energy is absorbed in a typical 10 atm mixture. The uncertainty in the measured energies with and without the gas cell in the beam is approximately 5–10%, which gives unacceptable relative uncertainties in absorbed energies and conversion efficiencies. In the presentation of multiline pumping results in chapter 6 we shall therefore give data for CO<sub>2</sub> output energy as a function of the total input pumping energy, and the amount of absorbed energy and the conversion efficiency can only be roughly indicated.

These problems are avoided in single-line pumping where the whole pumping energy is assumed to be absorbed (refer to comments given above).

## 5.2 The DF pumping laser

A pulsed chemical DF laser (model TEA 203 manufactured by Lumonics Research Limited in Canada) is used for the optical pumping. The excitation of this laser is initiated by a transverse electrical discharge in a flowing gas mixture of D<sub>2</sub>, SF<sub>6</sub> and He. Atomic fluorine is liberated by dissociation of SF<sub>6</sub> in the discharge, and vibrationally excited DF is produced in the exothermic chemical reaction (5.1)



where

DF\* – excited DF

This laser is therefore basically chemically pumped. The DF molecules are mainly excited into the three first vibrational levels by reaction (5.1), and lasing therefore occurs in the (1→0), (2→1) and (3→2) vibrational bands, as pointed out earlier.

A rough optimization of the operating conditions for maximum output energy has been made, and the following parameters were used in the experiments:

Gas pressure	0.04 atm
SF <sub>6</sub> : D <sub>2</sub> : He mixing ratio	8:1:1
Total gas flow	500 normal litres per hour
Pulse repetition rate	0.2 Hz
Discharge voltage	37 kV

The optimum gas pressure and mixing ratio agree reasonably well with data reported in the literature for pulsed DF lasers (55).

The required gas flow depends on the chosen pulse repetition rate. Variation in the discharge voltage from 35 kV to 40 kV did not lead to great changes in output energy.

We then pass on to a description of the operating characteristics of the laser in multiline and single-line operation. Some data for similar types of DF lasers operated in other optical configurations are found in the literature (55, 56) but the information that is really relevant for our experiments has not been reported.

### 5.2.1 Multiline DF laser operation

Operated with a two-mirror stable resonator the DF laser oscillates on about 25 transitions simultaneously in the  $(1 \rightarrow 0)$ ,  $(2 \rightarrow 1)$  and  $(3 \rightarrow 2)$  vibrational bands. The total pulse energy is approximately 0.6 J. The measured relative energy contents of the different lines is shown in Figure 5.3. Remember that the  $(1 \rightarrow 0)$  laser lines (marked by solid lines) are most efficient for excitation of the  $\text{DF} \rightarrow \text{CO}_2$  transfer laser. About 30% of the pulse energy is contained in these lines, while the  $(2 \rightarrow 1)$  lines and  $(3 \rightarrow 2)$  lines contain 40% and 30%, respectively. We observe that successive vibrational bands are shifted about  $90 \text{ cm}^{-1}$  due to anharmonicity in the vibration. The energy distribution of Figure 5.3 represents average values, and the energy of individual lines could vary as much as  $\pm 25\%$  from pulse to pulse. The pulse to pulse variation of the total pulse energy was not more than  $\pm 5\text{--}10\%$ . The large relative variations for the individual lines may give a substantial contribution to the uncertainties in the multiline pumping experiments.

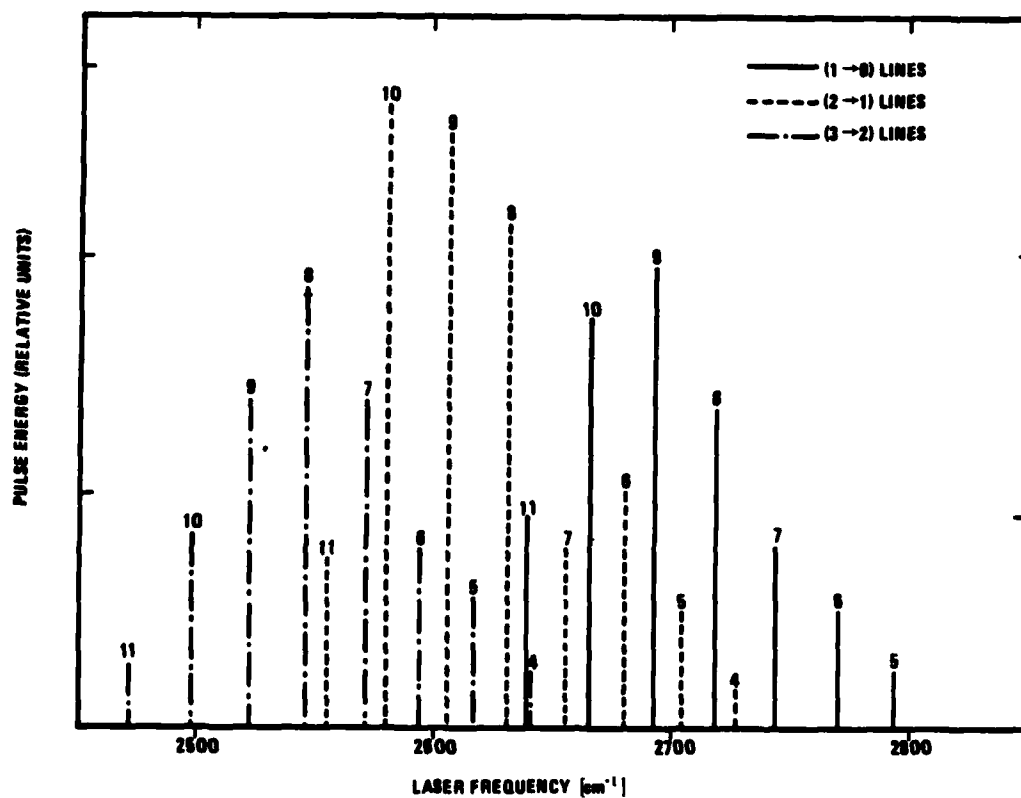


Figure 5.3 Relative energy distribution on the different lines of the multiline DF laser

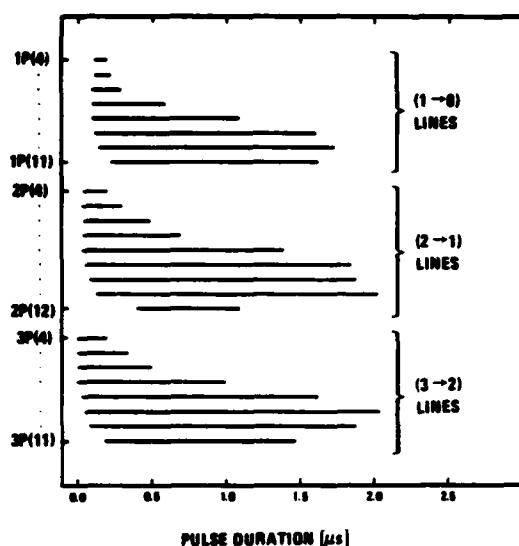


Figure 5.4 Duration of the laser oscillation on the different lines of the multiline DF laser

The total duration of the laser oscillation on the individual DF laser lines is shown in Figure 5.4. It can be observed that the build-up times are longest for the  $(1 \rightarrow 0)$  lines. This is disadvantageous with respect to pumping of the  $\text{DF} \rightarrow \text{CO}_2$  transfer laser, since absorption of the  $(2 \rightarrow 1)$  and  $(3 \rightarrow 2)$  lines cannot take place until the  $(1 \rightarrow 0)$  lines have produced a considerable excitation in the vibrational ladder of the DF absorbing molecules (see section 3.2.3).

Oscillograms of the pulse shapes of the  $(1 \rightarrow 0)$  lines and of the total laser pulse are shown in Figure 5.5. It will be noticed that the large pulse energies of the 1P(9) and 1P(10) lines may be attributed to longer pulse durations rather than higher peak powers. The spiking phenomena observed in all lines are probably due to a combination of longitudinal mode beating and repumping of the laser levels induced by laser

oscillation on lines in higher or lower vibrational bands (56). The spiking phenomena are always much less pronounced in the total laser pulse where the individual lines are superimposed. The start of the  $(1 \rightarrow 0)$  lines coincides with the peak of the total laser pulse, which has a 400 ns full width at half maximum and  $2 \mu\text{s}$  total length.

When it is operated with a stable resonator, the multiline DF laser has a multi-transversal-mode output beam with a beam divergence of about 3 mrad. The beam diameter is 30–35 mm, and the beam pattern has a noncircular symmetry which is probably imposed by the transverse electrode configuration of the laser. It contains several small areas of higher intensity which are usually called "hot spots". These are particularly troublesome because they may cause radiation damage on mirrors and Brewster windows in the optically pumped laser.

Due to the large beam divergence, the spot diameter of the focused multiline pumping beam is about 20 times larger than the diffraction limit. We shall see in section 5.3 that the matching of this beam to the  $\text{TEM}_{00}$  mode of the optically pumped laser resonator becomes poor.

### 5.2.2 Single-line DF laser operation

DF laser oscillation on a single laser line is obtained when a reflection grating and an unstable resonator output coupler form the laser resonator. According to theory (57) the unstable resonator configuration should lead to laser oscillation in a single transversal mode, and diffraction limited focusing of the laser beam should be possible.

The grating used in our experiments is gold coated with 300 grooves per millimeter and an efficiency of about 95% at DF laser frequencies. The unstable resonator output coupler is made of  $\text{CaF}_2$ , and it has a 15 mm diameter circular reflecting gold coated area on the convex side facing into the resonator. The laser radiation is coupled out in a doughnut mode around this area. A focused unstable resonator mode should merge into a single spot over a certain distance at both sides of the focus. The spot size should be diffraction limited with an actual intensity distribution determined by the outer and inner diameters of the doughnut mode at the focusing lens (58).

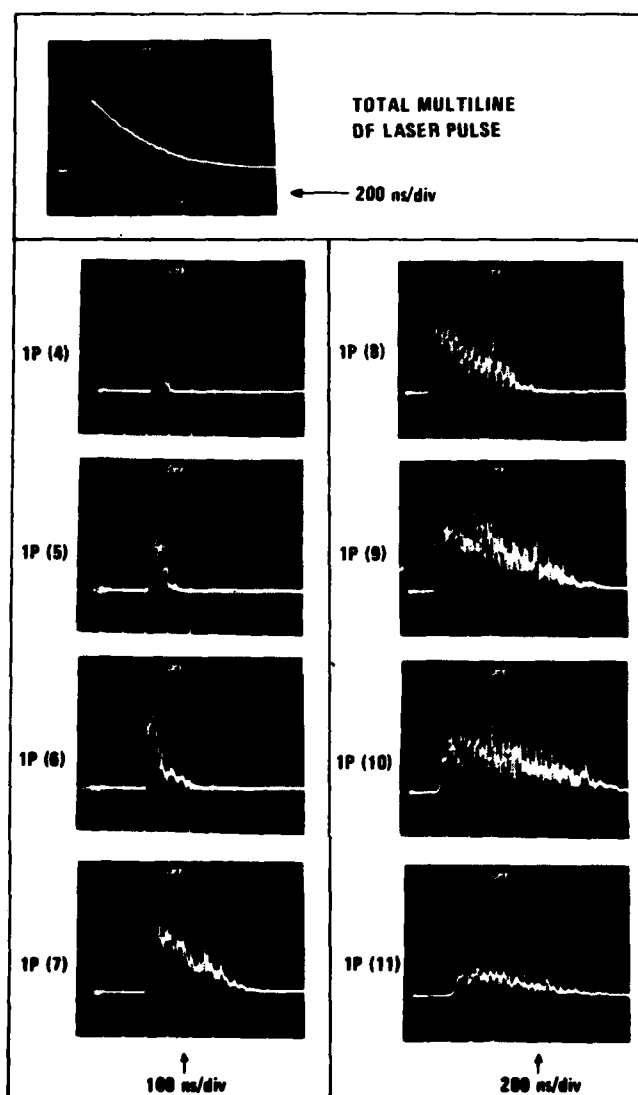


Figure 5.5 Pulse shapes of the individual lines and of the total DF laser pulse in multiline operation

As explained previously, only  $(1 \rightarrow 0)$  DF laser lines can be used in single-line pumping, and the 1P(7) line is chosen in our experiments. The reason for this choice is that the 1P(7) line is strongly absorbed by the DF in the  $\text{DF} \rightarrow \text{CO}_2$  transfer laser (see Figure 3.7), and a favourably high pulse energy can also be extracted on this line. Only 10% higher pulse energy is obtained on the strongest line 1P(9) in contrast to what we observed in Figure 5.3 for multiline operation. In Figure 5.3 we can observe that strong  $(2 \rightarrow 1)$  lines fall between the  $(1 \rightarrow 0)$  lines 1P(7) – 1P(11), and it turns out that it is difficult to avoid simultaneous oscillation on neighbouring  $(2 \rightarrow 1)$  lines when the grating is positioned for a  $(1 \rightarrow 0)$  line. This effect is particularly evident for the lines 1P(8) – 1P(11), and it also results in irregularities in the doughnut mode patterns. The choice of 1P(7) for single-line pumping is therefore natural.

The focused beam of the 1P(7) laser line contains about 30% of rapidly diverging radiation outside the central spot. We assume that this part of the radiation may contain contributions from neighbouring lines, but spectral analysis of the radiation has not yet confirmed this. An aperture with diameter slightly larger than the doughnut mode is inserted in the beam in front of the focus to block as much as possible

of the undesired radiation. The resulting focused spot diameter is then approximately four times larger than the diffraction limit. This deviation from the theory has not been examined further. We shall see in section 5.3.2 that reasonably good matching is obtained between the single line beam and the OPL TEM<sub>00</sub> resonator mode.

The maximum pulse energy obtained on the 1P(7) line in this configuration is about 80 mJ, which is about twice as high as the figure stated by the manufacturer. The pulse to pulse variation in the pulse energy is as large as  $\pm 20\%$ , which is similar to our observations for the individual laser lines in multiline operation. The reason for this

large variation has not been examined, but we assume that instabilities in the plasma discharge and changes in the laser resonator length may be responsible.

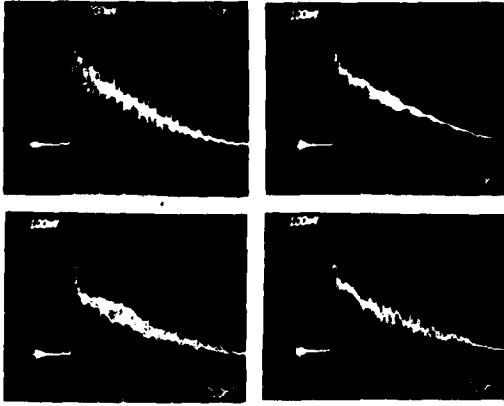


Figure 5.6 Single-line DF laser pulse shapes

Oscillograms of the 1P(7) laser line pulse shapes are shown in Figure 5.6. We observe pronounced longitudinal mode beating which changes from pulse to pulse, indicating variations in the resonator length. The pulses have a 400 ns full width at half maximum. This is approximately the same as the width of the total laser pulse in multiline operation, but the width is more than twice as large as that of the individual 1P(7) line in multiline operation (see Figure 5.5).

### 5.3 Matching between the pumping beam and the TEM<sub>00</sub> resonator mode of the DF $\rightarrow$ CO<sub>2</sub> transfer laser

Laser oscillation in the fundamental Gaussian TEM<sub>00</sub> transversal mode is usually desirable, because oscillation in higher order modes degrades the spectral purity of the laser radiation and leads to larger beam divergence. It is therefore important to achieve good overlapping between the excited gas volume and the TEM<sub>00</sub> resonator mode.

The beam radius  $\omega$  of a TEM<sub>00</sub> Gaussian beam is given by (24)

$$\omega(z) = \omega_0 \cdot \left(1 + \left(\frac{z}{z_0}\right)^2\right)^{1/2} \quad (5.2)$$

where

- $\omega_0$  — beam radius at the beamwaist
- $z$  — distance from the beamwaist
- $z_0$  —  $\pi \cdot \omega_0^2 \cdot \lambda^{-1}$  — Rayleigh distance
- $\lambda$  — radiation wavelength

At  $z=z_0$  the beam radius has increased by  $\sqrt{2}$  over the value  $\omega_0$  at the waist.

Since the DF laser wavelength  $\lambda_p$  is shorter than the CO<sub>2</sub> laser wavelength  $\lambda_L$ , we find that perfect matching between the pumping beam and the TEM<sub>00</sub> resonator mode cannot be obtained, even if the pumping beam were a TEM<sub>00</sub> Gaussian beam. However, assuming only Gaussian beams, the matching in the gas cell may become

extremely good, provided that the two beamwaists are matched with equal  $\omega_0$  at the cell centre, and that the Rayleigh distances  $z_0(\lambda_p)$  and  $z_0(\lambda_L)$  are greater than half the cell length.

The resonator parameters given in section 5.1 were:

$$\begin{aligned} R_1 = R_2 &= 30 \text{ cm (mirror radii of curvature)} \\ L_C &= 22 \text{ cm (resonator length)} \\ L_A &= 10 \text{ cm (length of gas cell)} \end{aligned}$$

Assuming matching at the cell centre we find:

$$\begin{aligned} \omega_0 &= 0.68 \text{ mm} \\ z_0(\lambda_L) &= 14.5 \text{ cm} \\ z_0(\lambda_p) &= 39 \text{ cm} \end{aligned}$$

We observe that  $z_0(\lambda_L), z_0(\lambda_p) \gg L_A/2$ , and the matching would therefore be straightforward for TEM<sub>00</sub> Gaussian modes.

In section 5.2 we have seen that the DF laser does not produce a fundamental Gaussian beam, and this causes complications as discussed below for multiline and single-line pumping.

### 5.3.1 Mode matching in multiline pumping

The geometries of the multiline pumping beam and the TEM<sub>00</sub> resonator mode inside the gas cell are indicated in Figure 5.7 for the actual focusing used in our experiments. The diameters are matched at the centre of the cell, but we observe that the diameter of the pumping beam greatly exceeds that of the resonator mode at each end of the cell. This is caused by the large divergence of the pumping beam which makes it impossible to obtain a smaller beam diameter over the 10 cm cell length. The geometry in the figure is obtained by focusing the pumping beam with a 40 cm focal length lens, and it gives approximately the smallest possible excited gas volume, which is important for obtaining a high CO<sub>2</sub> laser gain. The ratio of the geometrical volumes of the pumping beam and the resonator mode inside the cell is approximately 6:1. It should be noted that the effective overlapping of the two volumes is determined by the actual distribution of the excitation energy in the gas. This distribution is complex because of the multimode characteristics of the pumping beam, but the excitation is obviously strongest near the resonator axis. We may therefore assume that the effective overlapping is somewhat better than the 1:6 ratio given above.

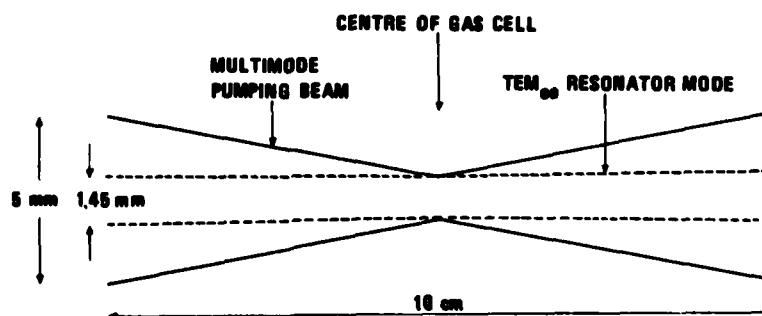


Figure 5.7 Approximate geometries of the multiline DF laser pumping beam and the CO<sub>2</sub> laser TEM<sub>00</sub> resonator mode in the 10 cm long laser gas cell



### 5.3.2 Mode matching in single-line pumping

In single-line pumping we are able to obtain a reasonably good mode matching even though the pumping beam spot size is not diffraction limited. Using a lens with 2 m focal length for focusing of the pumping beam, we obtain a beam diameter of about 1.6 mm at the centre of the cell and 1.8 mm at the ends. These diameters are only 0.25 – 0.35 mm greater than those of the  $TEM_{00}$  resonator mode, and they are comparable with the uncertainties in the alignment in our laser experiments.

### 5.4 Radiation damage at mirrors and Brewster windows

It is known that electrical breakdown will occur in optical materials if they are exposed to radiation densities higher than certain maximum limits. The damage thresholds depend on type of material, type of coating, cleanliness of surface, radiation wavelength and pulse length. We use ZnSe components in our experiments, and the damage threshold should be approximately  $10 \text{ J/cm}^2$  for a  $1 \mu\text{s}$  pulse at  $10 \mu\text{m}$  (59). No data exist for DF laser wavelengths, and we must only assume that the threshold will be similar to that at  $10 \mu\text{m}$ .

The average energy densities over the beam cross-section at the input mirror and at the Brewster windows in our experiments were in the order of  $1 \text{ J/cm}^2$  in single-line pumping and  $0.5 - 0.6 \text{ J/cm}^2$  in multiline pumping. The tilt angle of the Brewster windows has then been taken into account. These values are much smaller than the damage threshold for ZnSe, particularly in the multiline pumping experiments where the pumping beam cross-section at the mirrors and Brewster windows greatly exceeded that of the resonator mode (see Figure 5.7). Nevertheless, the damage problems were most severe in multiline pumping due to the hot spot pattern of the pumping beam. For this reason we could only use  $0.3 \text{ J}$  multiline pumping energy, which is about 50% of the total available energy. Even with this reduced input energy, damage occurred from time to time, and this may have some influence on our results in multiline pumping.

Ideally, we would have preferred to exchange an optical component as soon as any damage occurred, but this was not possible due to our limited stock of components suited for the experiments. It was our experience that small visible pits on the optical surfaces did not seriously alter the laser performance, and components were therefore only changed if the measurements indicated that damage affected the  $\text{CO}_2$  laser output. It was not always easy to distinguish damage effects from other effects that influenced the laser performance, such as imperfect optical alignment and variations in the gas mixture (see section 5.5).

Radiation damage was not a serious problem in single-line pumping, even if the average energy density was twice as high as in multiline pumping. The reason is apparently that the cross-section of the single-line beam is more uniform without the hot spot pattern. All the single-line pumping experiments could therefore be performed with the same input mirror, and it is therefore easier to interpret these results.

### 5.5 Preparation of gas mixtures

The preparation of laser gas mixtures should normally be trivial, but this was one of the major problems in our experiments due to the corrosive nature of the DF gas. A considerable amount of time was spent on investigating how the DF gas reacted with the different parts of the gas handling system, such as tubes, valves, pressure gauges, gas cell walls and cell windows. Many confusing observations have been made during the investigations, and we must admit that our choice of materials and procedures for

gas handling is based more on experience than on knowledge about what kind of reactions that are going on between DF and the different surfaces. It should be mentioned that the testing of components was performed parallel with and as a part of the multiline pumping experiments. Materials and components were changed several times during this period, and it was not until we started the single-line pumping experiments that a fixed system and fixed procedures were chosen. We feel that this may explain some of the confusing results obtained with multiline pumping.

A detailed discussion of the choice of materials and gas mixing procedures is given in Appendix F. The importance of paying attention to these problems should be noticed by anyone who intends to build a laser of this kind, and we believe that the information found in Appendix F may be valuable. Here we shall only list the most important conclusions.

- a) DF seems to react with the gas handling system by a combination of a chemical reaction and surface adsorption. The adsorption causes the DF pressure to decrease rapidly after gas filling, and good saturation of the laser gas cell is necessary to achieve a constant DF pressure during an experiment.
- b) The presence of water vapour in the system should be avoided since deuterium is rapidly exchanged with hydrogen in the water.
- c) Teflon, stainless steel and monel have been tested as gas cell materials. Teflon seems to be most favourable with respect to surface adsorption and corrosion, but it is not well suited for high-pressure gas cells. Stainless steel gave a reasonably slow surface adsorption after saturation, and a stainless steel gas cell was used in the single-line pumping experiments. Monel has excellent corrosion resistance, but the surface adsorption of DF on monel seems to occur very fast. A monel gas cell was used in the multiline pumping experiments, but the rapid surface adsorption was a serious problem.
- d) The ZnSe windows used in our gas cells have good resistance to chemical attack by DF, and the same windows have been used for one year without visible degradation.
- e) Coated gas cell windows have been tested, but the coatings were seriously attacked by DF.

Another major concern during this work was the presence of a significant amount of HF in the DF gas. Our best estimates from spectroscopic measurements showed that the DF gas contained about 20% HF. DF gas with better purity was not available to us in this work. A discussion of our observations of the HF impurity and the determination of the HF contents is given in Appendix G.

The presence of HF in our laser is unfavourable because HF deactivates the  $\text{CO}_2$   $\nu_3$  mode even faster than DF does (48). With 20% HF in the DF gas the HF will contribute with about 20% to the relaxation rate of the  $\text{CO}_2$   $\nu_3$  mode for a typical 10 atm laser gas mixture containing 0.5% DF, 5%  $\text{CO}_2$  and 94.5% He (refer to section 3.2.5). According to our theoretical calculations this increase in the relaxation rate should however not significantly influence the laser performance. Another negative effect might be transfer of vibrational energy into the HF vibrational mode, but the rate of this process seems to be too low to play a significant role (60). This can of course only be finally confirmed by repeating the experiments with DF gas which is free of impurities.

## 5.6 CO<sub>2</sub> laser gain measurements

Measurement of the time dependence of the CO<sub>2</sub> laser gain may give important information about the behaviour of the laser system. A simple experimental set-up that we have used for gain measurements is shown in Figure 5.8. A probing beam from a continuous-wave CO<sub>2</sub> laser is directed through the gas cell of the optically pumped laser where the laser mirrors have been removed. The beam is focused for the best possible matching with the pumping beam which comes in the opposite direction. The probing power is monitored by a high-speed HgCdTe detector, and the relative increase in the detector signal subsequent to the absorption of the pumping radiation gives the CO<sub>2</sub> laser gain in one pass through the gas cell. The probing power is sufficiently low not to cause significant perturbation of the CO<sub>2</sub> population inversion.

A typical example of the time dependence of the detector signal is shown in the figure, and the pumping pulse shape is shown for comparison in the same time scale. The gain first increases when the pumping power is integrated as excitation energy in the CO<sub>2</sub>  $\nu_3$  mode. The time of peak gain is expected to occur at the end of the pumping pulse when the relaxation rate of the CO<sub>2</sub>  $\nu_3$  mode starts to dominate over the pumping rate. We observe however that the measured gain starts to decay very early, and there is even a substantial undershoot in the tail. Further results will be presented in chapter 6, and we shall only mention here that the rapid decay and the undershoot seem to be caused by refractive index gradients which occur in the gas as the pumping energy is converted to thermal energy. The index gradients seem to cause so strong defocusing that a fraction of the probing beam no longer hits the detector area.

The lens  $L_D$  has 50 mm focal length, and it focuses the probing beam to a 0.5 mm diameter spot on the 1 mm diameter detector surface. From these figures it is clear that the defocusing is substantial, and this may have significant influence on the performance of the laser as discussed in chapter 6.

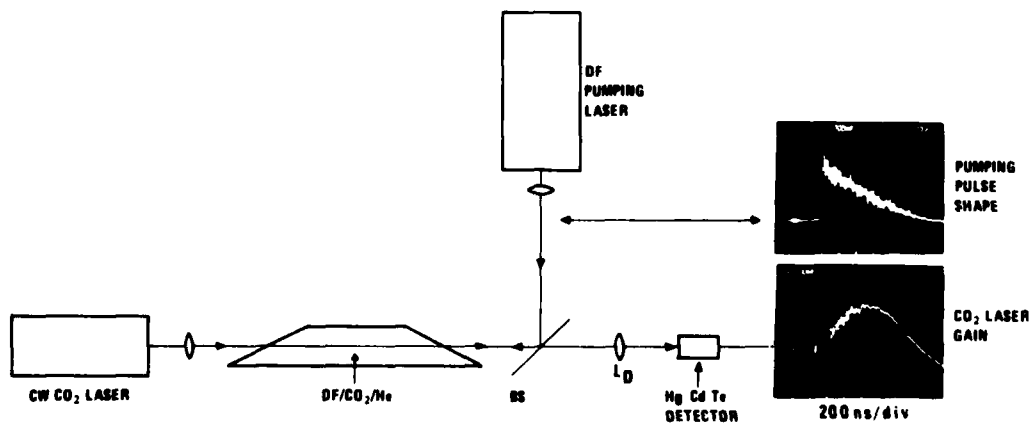


Figure 5.8 Experimental configuration used in the gain measurements  
The units of the ordinates in the oscillograms are arbitrary.

### 5.7 Frequency tuning experiments

There was not room in this work for a final development of the frequency tuning techniques. However, selected frequency tuning experiments have shown that continuous tuning of the laser frequency between two adjacent CO<sub>2</sub> line centres can be obtained. The tuning experiments have been performed in the CO<sub>2</sub> laser R-branch at about 975 cm<sup>-1</sup>.

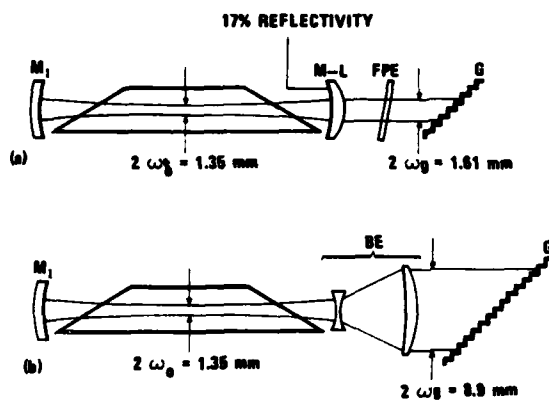


Figure 5.9 Resonator configurations used in the frequency tuning experiments

M-L	—	combined mirror-lens
FPE	—	Fabry-Perot etalon
G	—	grating
BE	—	beam-expander

Two different resonator configurations have been used in these experiments, and they are illustrated in Figure 5.9. The basic frequency selective elements are a diffraction grating G and a Fabry-Perot etalon FPE. In configuration a) a combined mirror-lens M-L is placed in front of the grating, and the Fabry-Perot etalon is inserted between these elements for fine tuning of the laser frequency. This configuration requires a closer explanation, and we shall return to that later. In configuration b) a beam expander is used to obtain a larger resonator mode diameter at the grating for better frequency resolution. In both cases the resonator elements are arranged in such a way that the TEM<sub>00</sub> mode has a beamwaist with diameter  $2\omega_0 = 1.35$  mm at the centre of the gas cell. The resonator

mode in the gas cell is then identical to the resonator mode of the two-mirror laser experiments described in section 5.1. This ensures the best possible matching with the pumping beam as discussed in section 5.3.

The frequency resolution bandwidth  $\Delta\nu_g$  of the pure grating is given by

$$\Delta\nu_g = \frac{\nu}{N} \quad (5.3)$$

where

$\nu$  — radiation frequency

$N$  — number of grating grooves illuminated by the resonator mode

The beamwaist diameters  $2\omega_g$  at the grating are given in Figure 5.9. The grating groove density is 135 grooves per mm, and the following resolution bandwidths at 975 cm<sup>-1</sup> are then obtained for the pure grating

Configuration a) —  $\Delta\nu_g = 3.2$  cm<sup>-1</sup>

Configuration b) —  $\Delta\nu_g = 0.6$  cm<sup>-1</sup>

These values can be compared with the frequency spacings between adjacent CO<sub>2</sub> line centres which are 1.2–1.4 cm<sup>-1</sup> in the R-branch. The resolution in b) is high enough to allow tuning of the laser frequency between two line centres as will be shown in chapter 6.

We will now discuss configuration a) in more detail, and to start with we disregard the FPE. M-L is a ZnSe lens with one uncoated side facing against the input mirror  $M_1$ . The reflectivity of this side is 17%. The purpose of M-L is two-fold. First, it serves as a lens which makes it possible to obtain resonator mode beamwaists both at the cell centre and at the grating. Second, the combination of the reflecting surface and the grating gives a higher reflectivity than that of the pure grating. The reflecting surface is matched to the wavefront of the resonator mode, and together with the grating it forms what we call a mirror-grating "etalon", MGE. The MGE has reflection maxima and minima, just as an ordinary etalon. In this case we wish to operate at one of the reflection maxima of the MGE. For a general etalon with surface reflectivities  $R_1$  and  $R_2$  the reflectivity at the maxima is given by

$$R_{\max} = \left( \frac{\sqrt{R_1} + \sqrt{R_2}}{1 + \sqrt{R_1 \cdot R_2}} \right)^2 \quad (5.4)$$

Suppose that  $R_1$  is the 17% reflectivity of the M-L and that  $R_2$  is the frequency dependent reflectivity of the grating. We then find that the MGE will have a spectral reflection characteristic like that shown in Figure 5.10a. The regions of high reflectivity

( $R_{\max}$  given by equation (5.4)) are interrupted by narrow regions with high loss which are the "transmission" peaks of the MGE. The spectral reflectivity of the pure grating is also given in Figure 5.10a. We have assumed that the reflectivity is centred at the R(18)  $\text{CO}_2$  laser line as indicated in the figure. We observe that the maximum reflectivity of the MGE is about 98%, while the grating used in our experiments has a maximum reflectivity of about 95%. The increase in reflectivity is obtained at the expense of a broader spectral resolution bandwidth. The increased reflectivity may be important because the use of frequency selective elements leads to high resonator losses and marginal net gain in the laser.

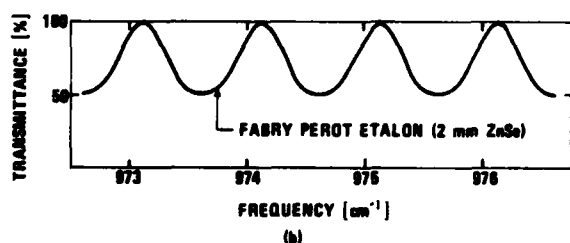
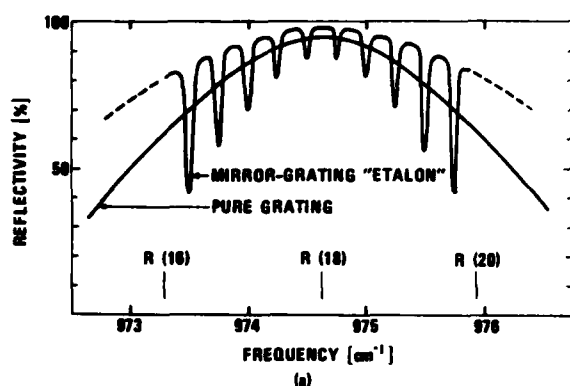


Figure 5.10 Theoretical spectral characteristics of the frequency selective elements

losses in the etalon the actual transmission at the peaks was only 95–96%. The resulting spectral reflectivity after inserting the etalon between M-L and the grating becomes complex, and it is not shown here. Laser oscillation will in general occur at one of the transmission peaks of the etalon, and the frequency can be tuned by tilting the etalon.

The spectral resolutions of the MGE and of the pure grating are both too low to allow continuous frequency tuning between the  $\text{CO}_2$  line centres, and an additional Fabry-Perot etalon has to be used for this purpose. A 2 mm uncoated ZnSe etalon was used in the experiments, and the theoretical spectral transmittance of this etalon is shown in Figure 5.10b. Due to

The configurations a) and b) were tested in the multiline and single-line pumping experiments respectively. The results will be presented in chapter 6, and we shall only mention that CO<sub>2</sub> laser oscillation between two adjacent CO<sub>2</sub> line centres was obtained with both configurations. It is not yet clear which of the configurations that will be preferred in a practical laser system. The complex spectral reflectivity of the MGE is obviously a drawback, and to obtain continuous frequency tuning it is necessary to control the positions of the reflection minima of Figure 5.10a. On the other hand, the maximum reflectivity of the frequency selective elements can become very high in this configuration. In configuration b) the frequency tuning can be performed by merely tilting the grating. Relatively high total losses in the beam-expander and the grating may be an objection to this solution. Very careful optical alignment is required with a beam expander in the resonator, and this may be a practical problem.

## EXPERIMENTAL RESULTS

In this chapter we present the results of the experimental investigations of the optically pumped DF→CO<sub>2</sub> transfer laser. Results are given for gain measurements (section 6.1), measurements of CO<sub>2</sub> laser output energies, pulse shapes and quantum efficiencies (section 6.2) and for frequency tuning measurements (section 6.3). The results will be discussed parallel with the presentation.

All the DF partial pressures given in this chapter include about 20% HF which was present in the DF gas (see section 5.5).

### 6.1 Results of gain measurements

The experimental procedure used in the gain measurements has been described in section 5.6. Gain measurements for high-pressure gas mixtures were only performed in the case of single-line pumping, and a typical 10 atm gas mixture containing 0.6% DF, 5% CO<sub>2</sub> and 94.4% He was chosen in the experiments. This example will demonstrate that the effect of gas heating and subsequent formation of pressure waves may influence the laser performance significantly.

Oscillograms of the time evolution of the measured single pass gain for different pumping pulse energies are shown in Figure 6.1. The pumping pulse shape is shown for comparison in the same time scale. The single pass gain is the relative amplification of the cw probing laser power in one pass through the 30 cm laser gas cell. The probing laser here oscillates on R(18) at 974.6 cm<sup>-1</sup>. We observe that the gain reaches a maximum approximately 500 ns after the start of the pumping pulse, and at 3 mJ pumping energy the peak gain is about 25%. The noise at the start of each trace is picked up from electric fields that were present in the laboratory subsequent to the plasma discharge of the DF pumping laser. A characteristic feature in the time evolution of the gain is the rapid decay which becomes more pronounced for increasing pumping energies. This is illustrated further in Figure 6.2a where oscillograms are shown in longer time scales. Those traces were all recorded for pumping energies of about 75 mJ. We observe that "negative gain" is measured from about 1.2 μs after the start of pumping, and the undershoot period

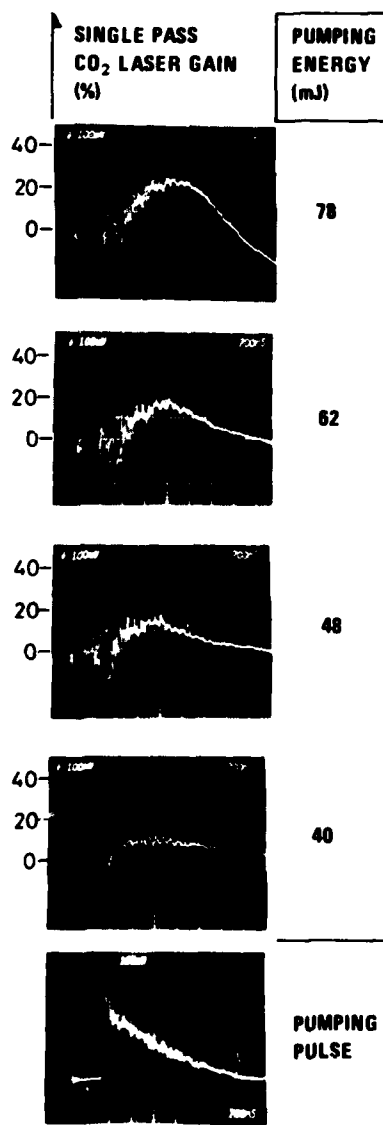


Figure 6.1 Time evolution of the single pass CO<sub>2</sub> laser gain for a 10 atm gas mixture containing 0.6% DF, 5% CO<sub>2</sub> and 94.4% He

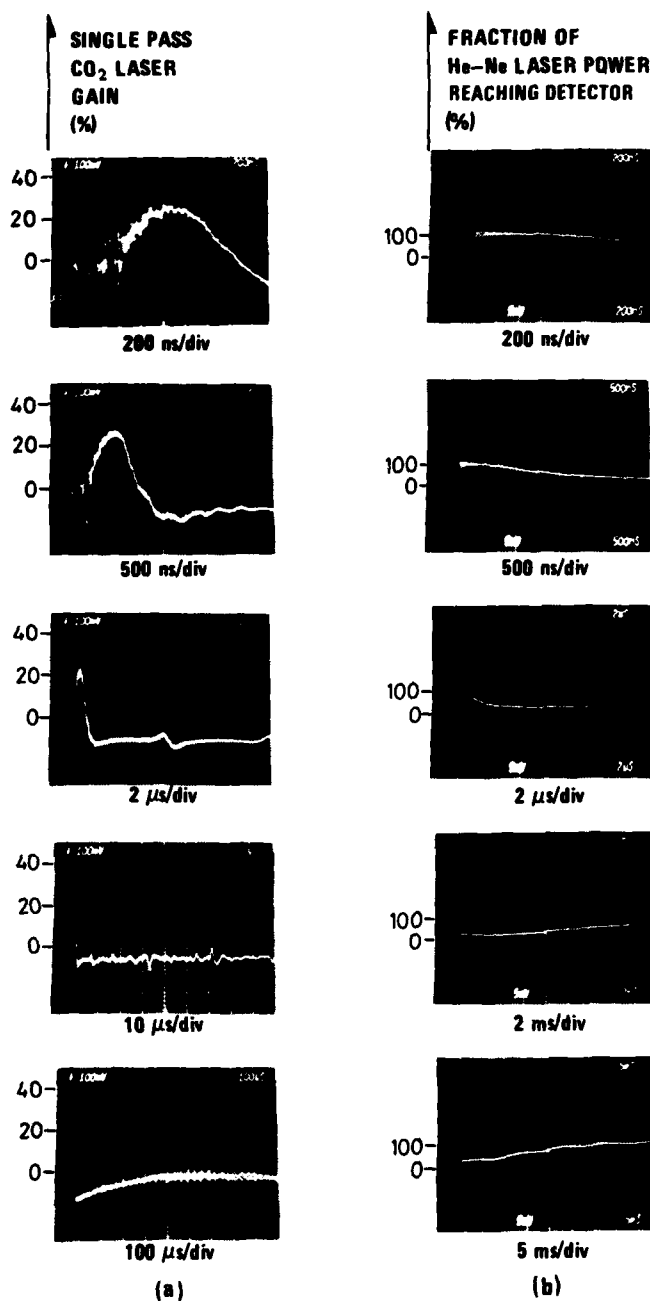


Figure 6.2 The effects of pressure wave formation on the measured  $\text{CO}_2$  laser gain (a), and on the He-Ne laser power reaching the detector after passage through the pumped gas volume (b)

lasts for 300–400  $\mu\text{s}$ . In this period less probing power hits the detector area than before the pumping started. The most natural explanation for the phenomenon is that the probing beam is strongly defocused by refractive index gradients which occur in the gas as a result of gas heating. The ripple that is observed in the trace in the undershoot period seems to be due to pressure waves which are bouncing back and forth in the gas cell. The ripple is not strictly periodic, but a period of about 10  $\mu\text{s}$  seems to exist. Since the velocity of sound in this gas mixture is about 1 mm/ $\mu\text{s}$ , the 10  $\mu\text{s}$  period agrees well with the time of one pass across the 10 mm internal cell width. The pumping beam was not centred along the axis of the gas cell, and this probably explains why the ripple is not strictly periodic.



To check the assumptions a He-Ne laser beam was directed through the pumped gas volume and onto a detector. The time dependence of the He-Ne laser power reaching the detector is shown in Figure 6.2b. The results confirm that strong defocusing of the beam is responsible for the undershoot in the detector signal. In this case we were even able to observe the defocusing by eye. The detector signal starts to decrease about 500 ns after the start of pumping, and this is in accordance with our observations of the CO<sub>2</sub> laser gain. In 500 ns a pressure wave travels about 0.5 mm, and since the diameters of the pumping and probing beams are 1.6 – 1.8 mm, it seems natural that defocusing will occur in that timescale. We observe that only 10–20% of the He-Ne laser power hits the detector in the undershoot period which lasts as long as 20 ms. In these experiments the He-Ne laser beam was guided into a screened room over a distance of about 15 m to eliminate the noise from the DF laser discharge. Due to the long distance between the gas cell and the detector, the undershoot in the detector signal is much larger than in the gain measurements, and this also explains the long duration of the undershoot. The characteristic ripple in the detector signal cannot be observed in Figure 6.2b because the ripple is only about 5% of the total probing beam signal (see Figure 6.2a), and the remaining signal is here only 0.1 – 0.2 divisions in the oscillogram. The ripple has however been observed in other measurements when the probing beam signal was larger.

It seems that the effects observed here may have significant influence on the performance of the optically pumped laser. The defocusing effect starts to be important in a time interval which coincides with the tail of the CO<sub>2</sub> laser pulse, as will be seen in section 6.2. It is however difficult to predict how serious this effect will be in the laser. The laser resonator mode will probably be distorted, but it is not obvious that the gain of the resonator mode will be so seriously influenced as these measurements of the gain might indicate. The measured time dependences in Figures 6.1 and 6.2 obviously depend on the size of the detector area. A larger detector would measure a higher gain and a smaller undershoot, since a larger part of the defocused probing radiation would then hit the detector surface. A detailed theoretical analysis would be required to find out from the results of the gain measurements how the laser performance is affected. We have not made such an analysis, and we shall only keep these effects in mind when discussing the results of the laser experiments.

A large number of gain measurements were also performed in the case of multiline pumping at the beginning of this work. They were all performed at gas pressures lower than 1 atm, and the results were qualitatively the same as those presented above. At such gas pressures one would expect the gas heating to be more serious, but in multiline pumping the pumping energy is absorbed in a considerably larger gas volume (see section 5.3.1), and the measured detector signals had a time dependence similar to those of Figures 6.1 and 6.2a. In general, higher pumping energies resulted in faster decay of the gain as in Figure 6.1. A faster decay was also observed for increasing DF partial pressures, due to enhanced absorption of the pumping radiation.

It should be noted that the effects described in this section will be even more pronounced in the case of CO<sub>2</sub> laser oscillation, since the CO<sub>2</sub> laser oscillation leads to a faster increase in the T/R temperature as explained in section 3.2.6 (see Figure 3.10).

## 6.2 Results of laser experiments performed with the two-mirror CO<sub>2</sub> laser resonator

The results obtained with multiline and single-line pumping of the DF→CO<sub>2</sub> transfer laser will be presented in sections 6.2.1 and 6.2.2 respectively. A comparison of the maximum pulse energies and quantum efficiencies obtained with multiline and single-line pumping will be made in section 6.2.3.

### 6.2.1 Multiline pumping

Most of the multiline pumping experiments were performed with the experimental configuration that was shown in Figure 5.2. The highest  $\text{CO}_2$  laser pulse energies were not obtained in this configuration, but the results of these experiments give the most complete picture of the laser operation characteristics obtained with multiline pumping, since data were taken for several combinations of gas mixture, total gas pressure and pumping energy.

The results are summarized in Figure 6.3 where the  $\text{CO}_2$  laser pulse energy is plotted as a function of the total multiline pumping energy for four different total gas pressures. The DF partial pressure has been varied from 0.02 atm to 0.06 atm while  $\text{CO}_2$  partial pressures of about 0.5 atm and 1.0 atm have been used. The plotted output energies have been corrected for the transmission loss in the filter F shown in Figure 5.2. The relatively large uncertainties in the results of the multiline pumping experiments have been pointed out in chapter 5. Radiation damage at the input mirror and Brewster windows as well as uncertainties in the determination of the DF

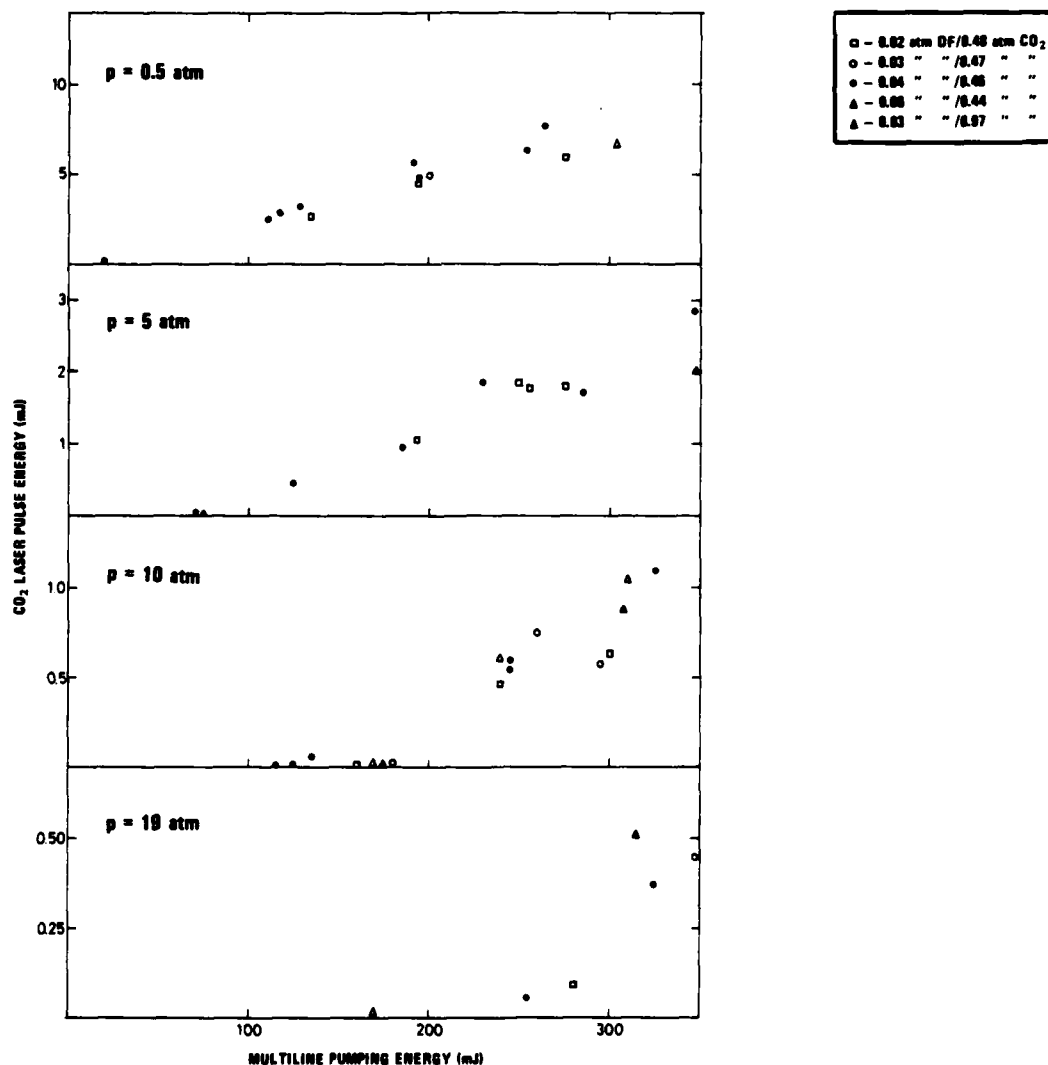


Figure 6.3  $\text{CO}_2$  laser pulse energies obtained with multiline pumping at different gas pressures

partial pressure are the most important sources of experimental errors. It is observed in Figure 6.3 that the choice of gas mixture seems not to be critical with respect to the  $\text{CO}_2$  laser output energies. The scattering in the data points for the same gas mixture is in many cases greater than the variations for the different gas mixtures, and a definite conclusion about the choice of optimum gas mixtures is difficult to make. It seems however that the highest DF partial pressures give the best results at high total gas pressure. This is particularly evident at 19 atm gas pressure, but it should be noted that only few data exist at that pressure. A variation in the  $\text{CO}_2$  partial pressure by a factor of two seems not to result in significant changes, but only few data have been taken. It can furthermore be noticed that the threshold pumping energy for the onset of  $\text{CO}_2$  laser oscillation increases with increasing gas pressure, and there is a corresponding decrease in the output energies.

The  $\text{CO}_2$  laser output energies are low compared with the total pumping energies, but it should be noted that only a low fraction of the multiline pumping energy is absorbed by the gas, and we must also account for the fact that the energy of a pumping photon is almost three times larger than that of a  $\text{CO}_2$  laser photon. It was explained in section 5.1 that the determination of the absorbed multiline pumping energy became very uncertain. The amounts of absorbed pumping energy that were measured for different 10 atm gas mixtures are plotted in Figure 6.4. It is actually surprising that the data are as consistent as the figure shows. Even if there are a few large inconsistencies, it should be possible to determine the absorbed energies with an accuracy better than  $\pm 15\%$  for the highest pumping energies. We observe that less than 25% of the highest pumping energies is absorbed, and there seems to be a general trend of saturation in the absorption at high pumping energies. It has been pointed out earlier that the  $(1 \rightarrow 0)$  pumping laser lines are most strongly absorbed. These contain about 30% of the pulse energy (see section 5.2.1). It is clear that a significant part of this energy is also transmitted through the cell. We have observed that particularly the 1P(10) and 1P(11) lines are transmitted, but an exact determination of the transmittance became difficult because of the large pulse to pulse variations of the energies of the individual lines. For the same reason we were not either able to determine whether the  $(2 \rightarrow 1)$  or  $(3 \rightarrow 2)$  lines were significantly absorbed, but it seems to us that their contribution to the excitation in our experiments is of minor importance.

The apparent advantage of using higher DF partial pressures at high total gas pressures can be explained by the fact that a substantial enhancement in the absorption of the pumping radiation is obtained by increasing the DF partial pressure, as can be seen in Figure 6.4. The increased absorption more than compensates for the faster deactiva-

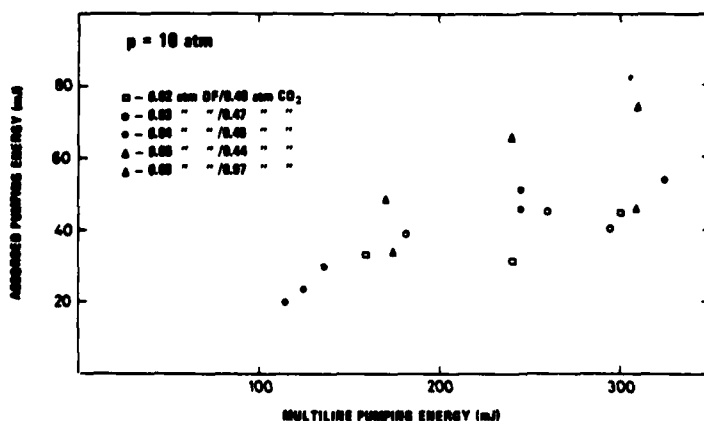


Figure 6.4 Absorbed multiline pumping energies at 10 atm gas pressure

tion of the  $\text{CO}_2$   $\nu_3$  mode which occurs at high DF partial pressures (refer to the discussion of section 3.2.5).

A few measurements were made with the configuration of Figure 5.1 at the end of the multiline pumping experiments. This is the configuration that was used in all the single-line pumping experiments. We shall present the best results from these measurements in section 6.2.3 where they will be compared with the corresponding results obtained with single-line pumping. Approximate quantum efficiencies will also be given, and these are calculated from the absorption data of Figure 6.4. The output energies obtained with this configuration were considerably higher than those of Figure 6.3, and we believe that this may be explained by lower absorption or scattering losses in the mirrors that were used in this case.

The  $\text{CO}_2$  laser pulse shapes obtained with multiline pumping were not essentially different from those obtained with single-line pumping, and they are difficult to discuss since no theoretical calculations have been performed for this case. The reader is therefore referred to the presentation and discussion of pulse shapes in the case of single-line pumping in section 6.2.2.

### 6.2.2 Single-line pumping

The single-line pumping experiments were concentrated on measurements with 10 atm laser gas mixtures, and the 1P(7) DF laser line was used for pumping in all cases. The gas mixing procedure described in Appendix F was used in these experiments, and this reduced the experimental uncertainties considerably. No significant radiation damage was observed in these experiments, and we believe that the experimental conditions have been reasonably constant during the measurements. The experimental configuration has been shown in Figure 5.1.

Curves of  $\text{CO}_2$  laser output energy as a function of the single-line pumping energy are shown in Figure 6.5 for different 10 atm gas mixtures. The coding a, b, c... for the gas mixtures is the same as the coding used in chapter 4, and it will be used also in

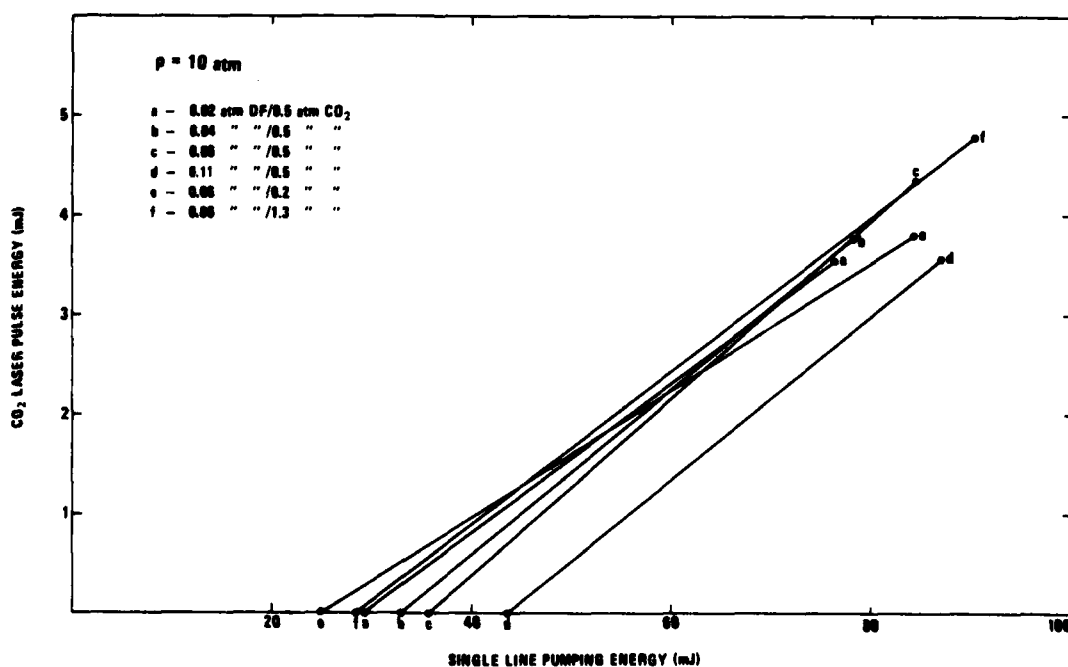


Figure 6.5  $\text{CO}_2$  laser pulse energy as a function of single-line pumping energy at 10 atm gas pressure

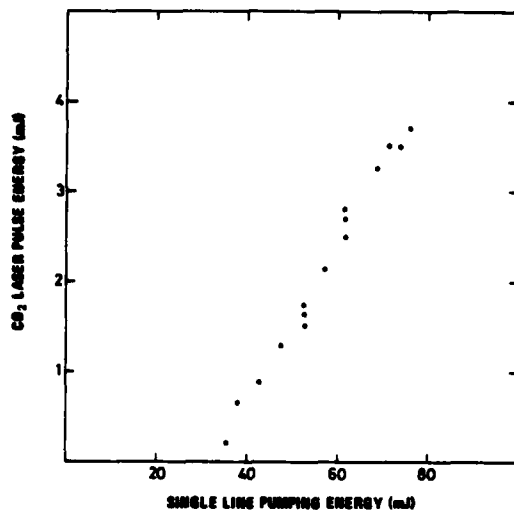


Figure 6.6 Recorded data points leading to curve b in Figure 6.5

later figures in this section. The results are corrected for the transmission loss in the beamsplitter BS of Figure 5.1. Each curve is the best fit of a straight line to 15–20 data points. A typical example of the recorded data points is shown in Figure 6.6. These are the data that gave curve b in Figure 6.5. The output energy seems to increase linearly with the pumping energy for pumping energies above the threshold. Some of the deviations from a straight line may be explained by small variations in the pumping pulse shapes (see Figure 5.6).

We observe from Figure 6.5 that the  $\text{CO}_2$  laser output energy is not critically dependent on the choice of gas mixture, and this agrees well with the results of the multiline pumping experiments. It should here be remembered that our theoretical calculations in chapter 4 gave almost identical quan-

tum efficiencies and pulse shapes for all the gas mixtures b, c, d, e and f. The differences observed in Figure 6.5 and in the experimental pulse shapes shown later are thus not explained by our theoretical model.

The results of Figure 6.5 indicate a slight increase in the threshold pumping energy for increasing DF partial pressure (curves a, b, c, d). We observe that curve d for the highest DF partial pressure is significantly displaced from the other curves, but it is interesting to note that the slope of that curve is about the same as for the others. With the possible exception of curve e the differences in the slopes of the curves are within our experimental uncertainties, and this may indicate that the slope quantum efficiency is mainly determined by the ratio between the output coupling  $T_{\text{OUT}}$  and the round trip resonator loss  $\ell_R$ . We shall see in section 6.2.3 that the round trip resonator loss calculated from the measured slope quantum efficiencies is considerably higher than the value of 6% used in our theoretical calculations of chapter 4. This seems to explain why the experimental quantum efficiencies presented in the next section are lower than the calculated values of chapter 4. The apparent increase in the pumping threshold with increasing DF pressure may be caused by a stronger formation of pressure waves, and we shall also comment on this later in the discussion of the  $\text{CO}_2$  laser pulse shapes.

Apart from the lower quantum efficiencies (see section 6.2.3) the results of Figure 6.5 are in reasonable agreement with the theoretical results of chapter 4 which showed very small changes in the output energies with gas mixture. Curve d seems however to be significantly displaced from the others. It should be mentioned that the experiment with gas mixture c was repeated three times, and the differences in the measured threshold and slope were not more than 10%. The other gas mixtures were only tested once.

The measured  $\text{CO}_2$  laser pulse shapes for the different gas mixtures are shown in Figure 6.7. The oscillograms are identified by the letters a–f that were used in Figure 6.5. The vertical scales of the oscillograms are not comparable. All the pulse shapes are measured for a pumping energy of approximately 75 mJ. The pumping pulse is shown in the same time scale for comparison, and the calculated pulse shape of chapter 4 is also shown at the bottom. Note that almost identical theoretical pulse shapes were calculated for all the gas mixtures in chapter 4.

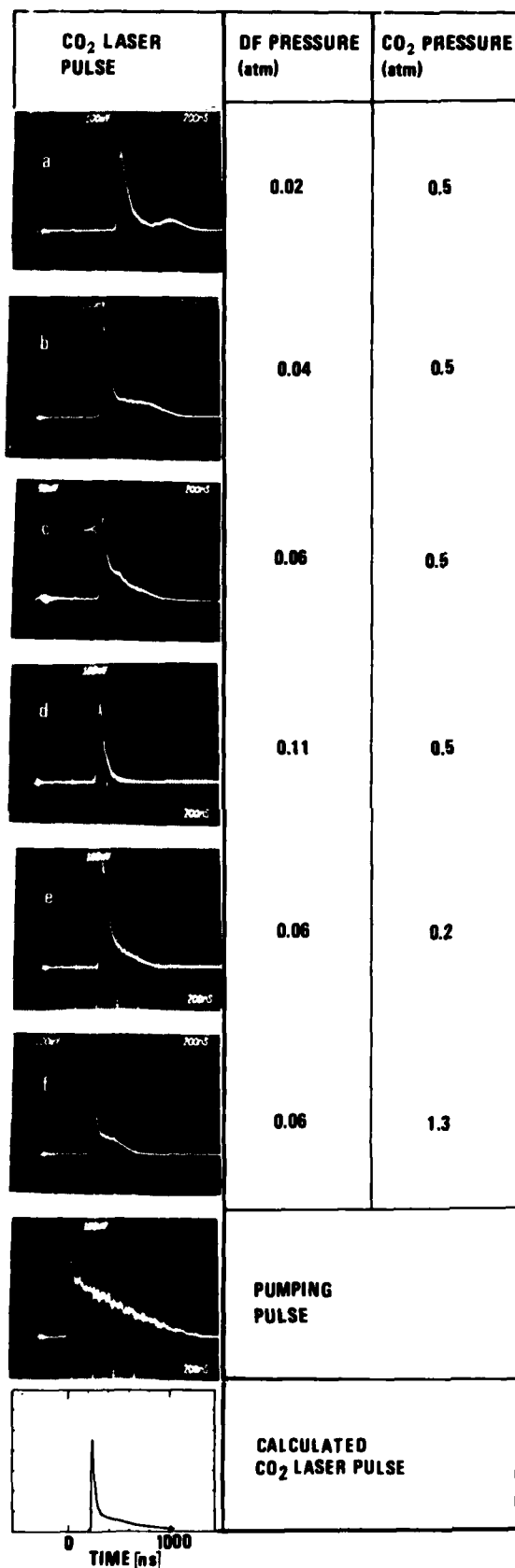


Figure 6.7 CO<sub>2</sub> laser pulse shapes obtained with different 10 atm gas mixtures for approximately 75 mJ single-line pumping energy

Significant differences are observed in the experimental pulse shapes for the different gas mixtures. Above all it appears that the laser oscillation build-up time increases with decreasing DF partial pressure and decreases with increasing CO<sub>2</sub> partial pressure. The latter effect might be explained by a shorter energy transfer time at high CO<sub>2</sub> pressures, but according to the computer calculations the effect should not be significant. We shall see below that as much as 20% of the pumping energy is transmitted through the gas cell at the lowest DF partial pressure, but that energy is reflected back into the resonator mode by the rear laser mirror, and this should therefore not lead to reduced gain and longer build-up time. Pressure waves should be of minor importance in the build-up period, and they are not likely to explain the differences. It therefore seems that effects in the laser dynamics which are not known to us at present may play a significant role. Nevertheless it should be noted that the differences in build-up time are only about  $\pm 60$  ns for the mixtures b–f, and the agreement with the calculated build-up time is reasonable.

The full width at half maximum of the measured pulses is 60–100 ns, while that of the calculated pulses is about 40 ns. Significant differences are also observed in the pulse tails. While the pulse tail for mixture a lasts almost as long as the tail of the pumping pulse, the pulse tail lacks completely at the highest DF partial pressure, d. We observed in the gain measurements (section 6.1) that pressure waves seem to become important in a time interval which coincides with the tails of the CO<sub>2</sub> laser pulses. Formation of pressure waves will be most serious at high DF partial pressures, and this may be the reason why the laser oscillation in the pulse tail is quenched for mixture d.

Even if pressure wave formation may explain some of the deviations

that are observed in the results obtained with the different gas mixtures, it should be noted that assumptions and simplifications made in the theoretical model may also lead to significant errors in the calculated results. Most questionable is probably the assumption of a plane pumping laser field and a plane CO<sub>2</sub> laser field. The distribution of the excitation energy and gain along the resonator axis will differ considerably for the different gas mixtures (see Figures 4.2 and 4.3), and it is possible that the different axial distributions combined with a varying mode diameter along the axis may explain some of the observed effects. It should be noted that the pumping laser intensity  $I_p$  used in the calculations is only a rough estimate, and the fine structure of the experimental pumping pulse has been neglected. The choice of round trip resonator losses  $\ell_R$  also influences the calculated pulse shapes. The parameters can be adjusted for better agreement between experimental and theoretical pulse shapes, but this has not been studied in detail. It seems however that the calculated pulse widths will be smaller than the experimental pulse widths for all reasonable choices of parameters. It should be mentioned that we have assumed CO<sub>2</sub> laser oscillation to occur at the R(18) line centre at  $974.6 \text{ cm}^{-1}$  in the theoretical calculations, while the laser oscillated at 2–4 line centres simultaneously in the experiments. It is possible that small differences in the build-up times of the different laser lines will lead to a larger pulse width, but this has not been analyzed further.

When comparing the results of Figures 6.5 and 6.7 it is observed that the output energies differ negligibly even if there are significant differences in build-up times and pulse shapes. The only exception is gas mixture d, where strong formation of pressure waves has been suggested as an explanation of the deviation.

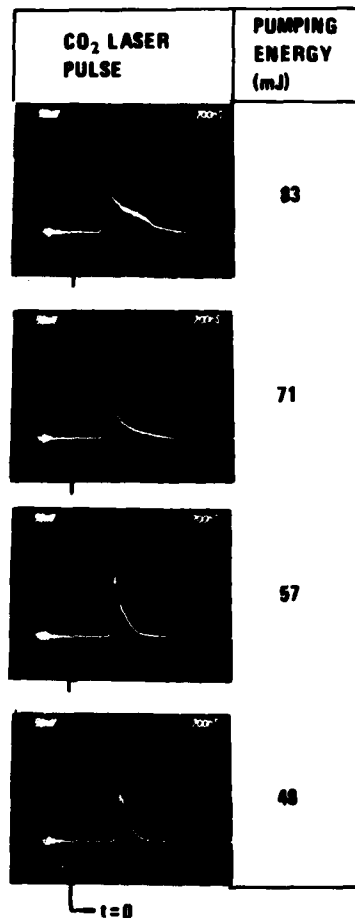


Figure 6.8 CO<sub>2</sub> laser pulse shapes obtained with gas mixture c of Figure 6.5 for different single-line pumping energies.

$t = 0$  at the start of the pumping pulse.

In Figure 6.8 the CO<sub>2</sub> laser pulse shapes are shown for different pumping energies using gas mixture c of Figure 6.5. The build-up time increases from about 240 ns to 400 ns for a reduction in the pumping energy from 83 mJ to 48 mJ. The vertical scales are comparable for these oscillograms, and the relative dependence of the pulse area on the pumping energy agrees reasonably well with the results of Figure 6.5. 48 mJ is only 12–13 mJ above the threshold pumping energy, and the pulse width is larger than for higher pumping energies due to lower gain and slower gain switching.

We have studied the pumping radiation that is transmitted through the gas cell for the gas mixtures a...f. The transmitted pumping energy as a function of the incident pumping energy is plotted in Figure 6.9. It can be seen that the transmitted fraction is lower than 10% except for mixture a with the lowest DF partial pressure, where 20–25% is transmitted. The dependence of the transmittance on the gas mixture is qualitatively in agreement with our calculations, but the calculated transmittance is lower than 1% for all the mixtures b...f which have been studied theoretically. There may be several reasons for these dis-

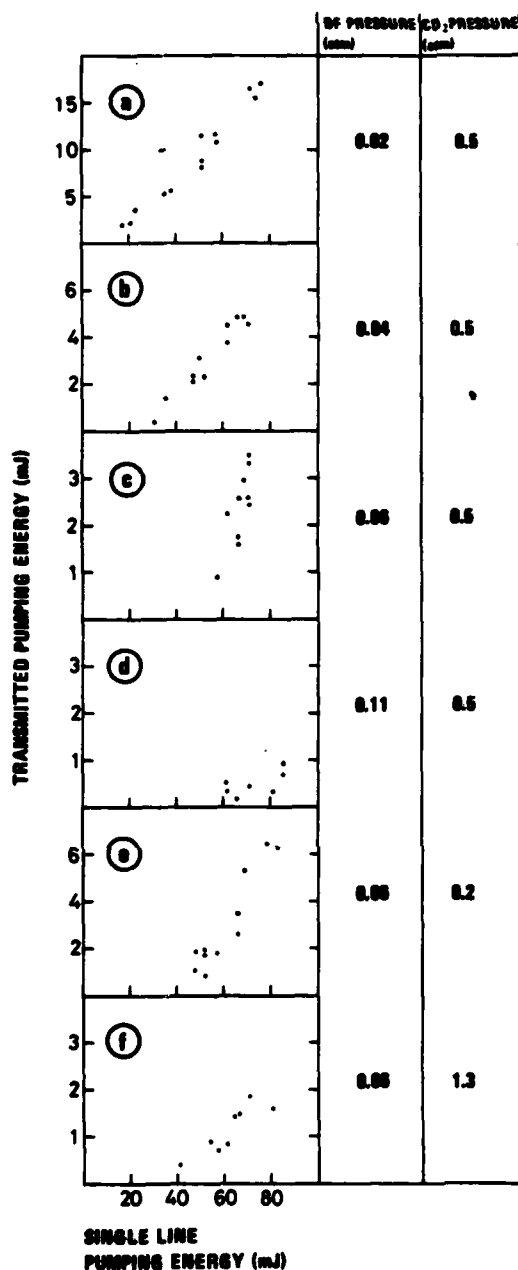


Figure 6.9 Transmitted single-line pumping energies for different 10 atm gas mixtures

saturation is the most probable explanation of the observed pulse shapes. It should be remembered that a smooth pumping pulse has been assumed in the computer calculations, and it may be that the spiking phenomena in the pumping pulse lead to other effects than those observed in the computed results. There is a particularly high spike in the leading edge of most of the pumping pulses, and it is possible that this spike will lead to a sharp transmitted pulse.

crepancies. First, our estimates of the pumping radiation intensity may be too low, so that a stronger saturation of the absorption occurs during the excitation. It was also pointed out in section 3.2.2 and in chapter 4 that our assumption of a Boltzmann distribution at temperature  $T_4$  in the DF vibrational energy ladder is questionable, since the pumping rate is of about the same magnitude as the internal V-V relaxation rate in DF. This may lead to a stronger saturation of the absorption than predicted by our model. We also feel that uncertainties in the reported values of the Lorentz broadening coefficients and Einstein coefficient for the DF absorption transition may lead to significant errors in the absorption coefficient. Saturation of the absorption for pumping energies larger than certain thresholds is clearly observed in Figure 6.9. The threshold increases for increasing DF partial pressure as expected.

The pulse shapes of the transmitted pumping pulses are shown in Figure 6.10 for four of the gas mixtures, and for a pumping energy of about 75 mJ. The saturation of the absorption is clearly observed, but the pulse sharpening is much more pronounced than in the calculated transmitted pulses (see Figure 4.6). Only a sharp spike at the leading edge of the pumping pulse is transmitted for the highest DF partial pressure, while a tail is observed for the lowest DF pressure. The extreme sharpness of the pulses might indicate that effects other than pure saturation are involved. Strong defocusing of the pumping beam caused by pressure waves might be one possible reason. However, the oscillograms in Figure 6.10 were recorded by reflecting the radiation diffusely onto the detector, and defocusing effects should therefore not influence the measured pulse shape. It therefore seems that

In Figure 6.11 curves are shown for the  $\text{CO}_2$  laser pulse energy as a function of the pumping energy for different total gas pressures. This dependence was only measured



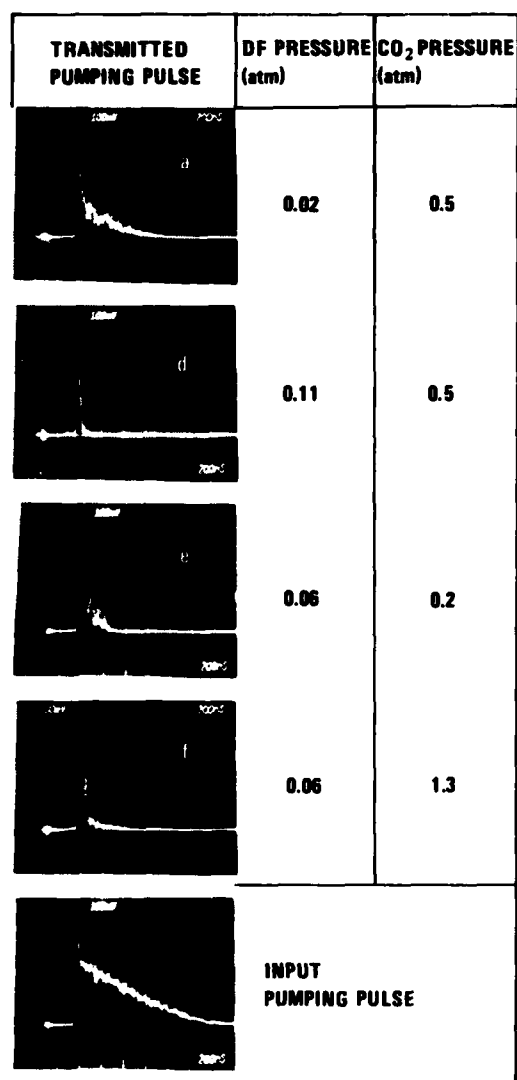


Figure 6.10 Transmitted single-line pumping pulse shapes for different 10 atm gas mixtures  
The incident pumping pulse energy is approximately 75 mJ.

for gas mixtures containing 0.06 atm DF and 0.5 atm CO<sub>2</sub>. The curves are the best fits of straight lines to data points like those that were shown in Figure 6.6. The lines are dashed for regions where data points are missing. Most striking are the small differences observed in the results for 5, 10 and 18.5 atm pressure. The results may be explained as follows: At 0.56 atm pressure the gain is so high that only a small threshold pumping energy is required to start the laser oscillation. When the pressure is increased to 5 atm, the gain decreases considerably due to the pressure broadening of the CO<sub>2</sub> laser lines, and the pumping threshold at 5 atm is therefore much higher. For a further increase in the gas pressure the CO<sub>2</sub> laser lines start to overlap, and there is no further reduction in the gain due to the pressure broadening. One would still expect an increase in the pumping threshold because of an increasing decay rate of the CO<sub>2</sub>  $\nu_3$  mode, but it seems that faster decay is of small importance. It should here be remarked that He only contributes with about 60% to the decay rate of the CO<sub>2</sub>  $\nu_3$  mode even at 18.5 atm total pressure (see section 3.2.5), which means that the decay rate increases only by a factor of 2.5 when the pressure is raised from 0.56 atm to 18.5 atm. It is also possible that reduced influence from pressure waves at high pressures may compensate for increased decay rates.

The fact that the CO<sub>2</sub> laser pulse energy seems to increase linearly with the pumping energy in Figure 6.11 as well as in Figure 6.5 may contradict our assumption of the importance of pressure waves. The influence of pressure waves would be expected to in-

crease for increasing pumping energy, which could lead to a saturation in the CO<sub>2</sub> laser output energies. Since this is not observed, it may be that we have overestimated this effect.

The CO<sub>2</sub> laser pulse shapes at the different total gas pressures are shown in Figure 6.12 for pumping energies of about 75 mJ. The observed pulse shapes seem to fit well into the picture of Figure 6.11 except perhaps for the relatively large difference in the pulse shapes at 10 and 18.5 atm gas pressure.

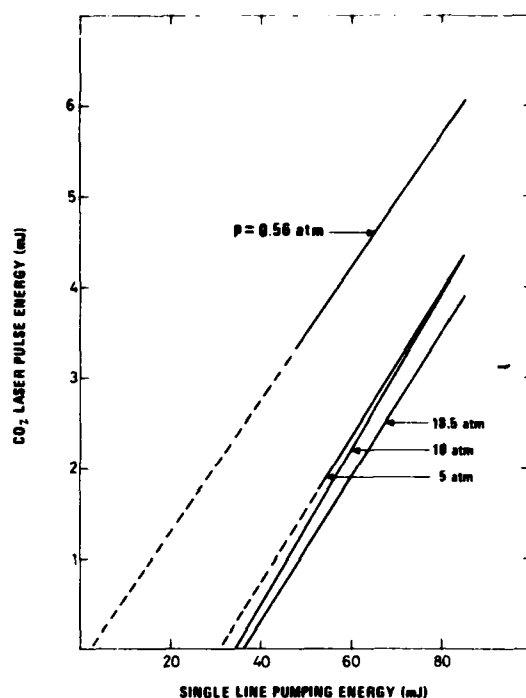


Figure 6.11  $\text{CO}_2$  laser output energy as a function of the single-line pumping energy at different gas pressures

All gas mixtures contain 0.06 atm DF and 0.5 atm  $\text{CO}_2$ .

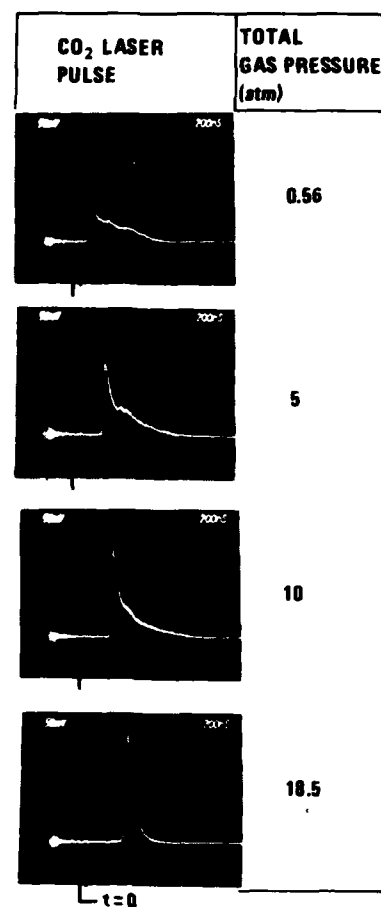


Figure 6.12  $\text{CO}_2$  laser pulse shapes obtained at different gas pressures for 75 mJ single-line pumping energy

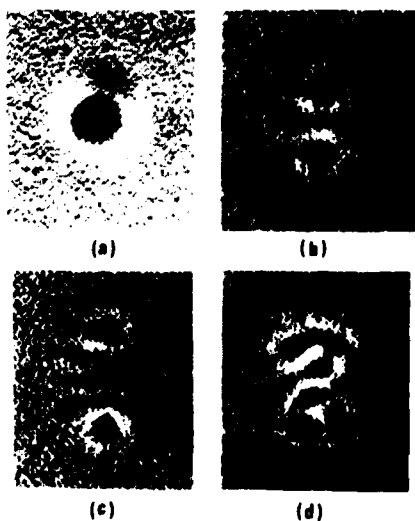


Figure 6.13 Transversal mode patterns of the  $\text{CO}_2$  laser beams

(a) - Good alignment of the laser resonator  
(b), (c), (d) - Misaligned laser resonator

In Figure 6.13 we give some examples of transversal mode patterns of the  $\text{CO}_2$  laser beam that have been recorded with a pyroelectric vidicon. The experiments are made with a 10 atm gas mixture containing 0.6% DF, 5%  $\text{CO}_2$  and 94.4% He. The mode pattern (a) was obtained for good alignment of the laser resonator relative to the pumping beam, and the mode diameter agrees well with that of a  $\text{TEM}_{00}$  resonator mode. The higher order transversal mode patterns (b), (c) and (d) were obtained with misaligned laser mirrors. Pattern (a) was obtained after the resonator was aligned with a He-Ne laser beam, and further adjustments did not lead to significant improvements in the mode quality or in the output energies. The vidicon was only available to us for a short period of time, and no such

recordings exist for other gas mixtures or for multiline pumping.

Before ending this section we shall mention that the  $\text{CO}_2$  laser oscillated on several lines simultaneously when the two-mirror resonator was used. At 10 atm it oscillated typically on the R(12) – R(18) lines in the  $975\text{ cm}^{-1}$  region, and this is consistent with the theory which predicts highest gain in the R-branch at high gas pressure (see Figure 3.4).

### 6.2.3 Output energies and quantum efficiencies

In this section we summarize the best results that have been obtained with multiline and single-line pumping with respect to  $\text{CO}_2$  laser output energies and quantum efficiencies.

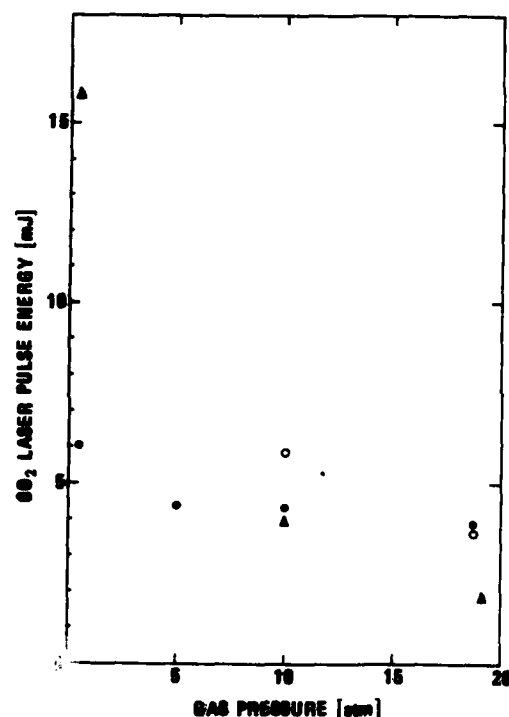


Figure 6.14 Maximum  $\text{CO}_2$  laser pulse energies obtained with multiline and single-line pumping

Filled triangles – multiline pumping, 3.5% output coupling  
 Filled circles – single-line pumping, " " "  
 Open circles – single-line pumping, 7% " "

The corresponding quantum efficiencies are shown in Figure 6.15. Two kinds of quantum efficiencies are plotted. The ratio between the number of generated  $\text{CO}_2$  laser photons and the number of absorbed pumping photons is called the total quantum efficiency. The slope quantum efficiency is calculated by dividing the number of  $\text{CO}_2$  laser photons by the number of absorbed pumping photons that exceed the threshold for onset of  $\text{CO}_2$  laser oscillation. The slope efficiency is often the most relevant quantity because it gives the efficiency that can be obtained when the laser is operated far above the threshold. The efficiencies obtained with multiline pumping have been calculated from the pulse energies of Figure 6.14 and absorption data like those of Figure 6.4. No results are given for slope efficiency in the case of multiline pumping because of the large uncertainties in the measured pumping thresholds. The results are all obtained with gas mixtures containing 0.06 atm DF and 0.5 atm  $\text{CO}_2$ .

The maximum pulse energies obtained at different gas pressures are plotted in Figure 6.14. As mentioned in section 6.2.1 the configuration of Figure 5.1 gave the best results also in the case of multiline pumping. A 3.5% output coupler was then used as in the single-line pumping experiments, and the maximum pulse energies are shown by the filled triangles in Figure 6.14. The maximum pulse energies obtained with the same configuration using single line pumping are shown by filled circles. These data are taken from Figure 6.11. In single-line pumping a 7% output coupler was also tested, and the open circles show the pulse energies that were obtained using that output coupler.

The corresponding quantum efficiencies are shown in Figure 6.15. Two kinds of quantum efficiencies are plotted. The ratio between the number of generated  $\text{CO}_2$  laser photons and the number of absorbed pumping photons is called the total quantum efficiency. The slope quantum

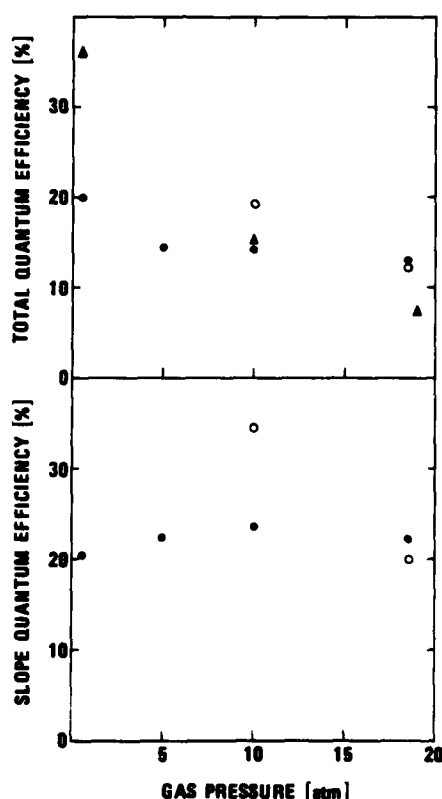


Figure 6.15 Total quantum efficiencies and slope quantum efficiencies obtained with multiline pumping and single-line pumping  
The coding was explained in the text of Figure 6.14.

The results of the multiline pumping experiments show that the  $\text{CO}_2$  laser output energy as well as the quantum efficiency decreases substantially for increasing total gas pressure, contrary to what we observe in the case of single-line pumping. The decrease in the output energies is partly owing to reduced absorption of the pumping radiation. We also assume that laser oscillation in higher order transversal modes may occur at low gas pressures. This will compensate for the large mismatch between the excited gas volume and the  $\text{TEM}_{00}$  resonator mode and lead to high output energies and quantum efficiencies. The number of oscillating transversal modes will probably decrease for increasing pressure, but we have not studied this experimentally. It is more difficult to explain why higher output energies and quantum efficiencies can be obtained with multiline pumping than with single-line pumping at gas pressures up to 10 atm. One possible reason is that the influence of pressure waves is smaller in multiline pumping since the excitation energy is distributed in a larger gas volume. We would however expect that the large mismatch with the  $\text{TEM}_{00}$  resonator mode would lead to considerably lower quantum efficiency at 10 atm pressure. The uncertainties in our measurements of the absorbed multiline pumping energies are not either likely to give a full explanation of these results. Another possibility is that reflected multiline

pumping energy from the rear laser mirror  $M_2$  may contribute more significantly to the excitation than we have assumed (see section 5.1). Altogether the quantum efficiencies presented for the case of multiline pumping should only be regarded as rough indications, and it may seem that they are too high compared with the results obtained with single-line pumping.

We observe in Figures 6.14 and 6.15 that the pulse energy and quantum efficiency obtained with single-line pumping at 10 atm gas pressure become considerably higher when the output coupling is increased from 3.5% to 7%. This illustrates the fact that the output coupling is not the dominating part of the round trip resonator losses. With higher output coupling the other resonator losses become less important, and the efficiency can be increased. The slope efficiencies obtained with the 3.5% output coupler are in the range of 20–24% for all the gas pressures in Figure 6.15, and efficiencies in the same range can be found from the curves in Figure 6.5 for the different 10 atm laser gas mixtures. The fact that the slope efficiency remains approximately unchanged for all choices of gas pressure and gas mixture strongly indicates that the slope efficiency is determined by the ratio between the output coupling  $T_{\text{OUT}}$  and the round trip resonator losses  $\ell_R$ . This means that  $\ell_R$  will be in the range of 14–18%, which is far above the value of 6% used in the calculations of chapter 4. We are unable to explain how the losses can become so high, but if this is correct, it means that great improvements in the quantum efficiencies could be ob-

tained with a low-loss laser resonator. Theoretical calculations have been performed for gas mixture c of Figure 6.5, using a round trip loss of  $\ell_R = 15\%$  and output coupling  $T_{OUT} = 3.5\%$ . The calculations gave a slope quantum efficiency of about 20% which confirms that the slope efficiency is approximately given by the ratio  $T_{OUT} / \ell_R$ . The calculated total quantum efficiency also then compared well with the value of 14% found in Figure 6.15, in contrast to the value of 45% calculated in chapter 4. The calculated build-up time was 280 ns, which is about 40 ns longer than the experimental value of Figure 6.7.

The slope quantum efficiency obtained with the 7% output coupler at 10 atm gas pressure is about 35% (see Figure 6.15), which indicates that  $\ell_R \approx 20\%$ . This agrees well with the  $\ell_R$  of 14–18% found from the results obtained with the 3.5% output coupler. The result obtained at 18.5 atm gas pressure with the 7% output coupler is somewhat confusing, and it should be mentioned that the result is based on a single experiment only. A further investigation will be necessary before definite conclusions can be drawn.

The output energies and quantum efficiencies obtained in this work are considerably higher than those reported previously for optically pumped high-pressure  $\text{CO}_2$  lasers. In particular, comparing with the results listed in Table 1.1, it can be seen that the output energies obtained with the present excitation scheme are more than an order of magnitude higher than previously reported values.

The peak power of the  $\text{CO}_2$  laser pulses has not been measured directly in these experiments, but from the measured pulse energies and pulse shapes we have estimated that the peak power obtained with the 7% output coupler at 10 atm gas pressure is in the order of 40 kW.

### 5.3 Results of frequency tuning experiments

As pointed out in section 5.7, the main purpose of the frequency tuning experiments was to demonstrate the feasibility of continuous tuning of the laser frequency. A further refinement of the techniques for narrow-band continuous tuning could not be done within the frame of this work. The  $\text{CO}_2$  laser R-branch at about  $975 \text{ cm}^{-1}$  was chosen as an example in these experiments, since the highest gain and the best line overlapping is obtained in the R-branches.

The resonator configuration used for frequency tuning in the case of multiline pumping was discussed in section 5.7 (see Figures 5.9a and 5.10). A 10 atm gas mixture containing 0.6% DF, 4.4%  $\text{CO}_2$  and 95% He was used. Without the Fabry-Perot etalon in the resonator the laser oscillated at 2–3  $\text{CO}_2$  line centres simultaneously due to the broad frequency bandwidth of the mirror-grating "etalon". Using the 2 mm uncoated ZnSe etalon in addition, we were able to obtain lasing in the frequency regions shown in Figure 6.16. Since the free spectral range of the etalon was only

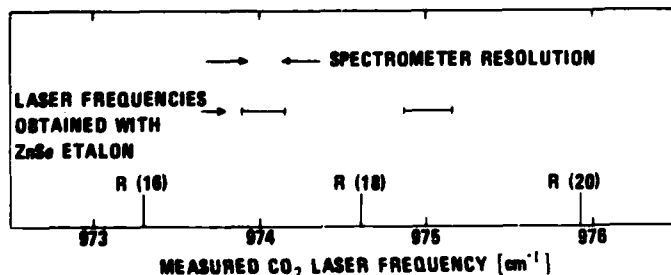
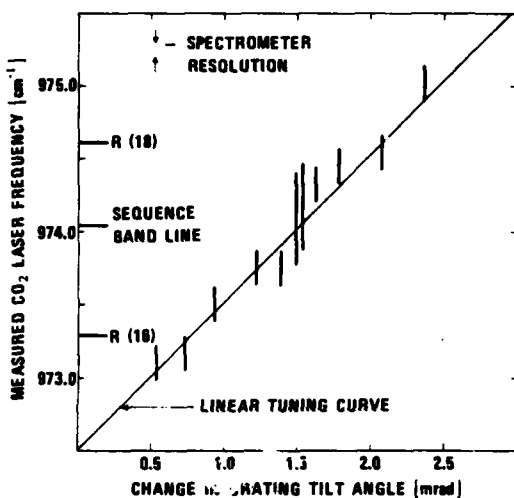


Figure 6.16 Results of frequency tuning experiment in the case of multiline pumping  $\text{CO}_2$  laser oscillation occurs at two transmission maxima of the 2 mm ZnSe etalon (see explanation in the text).

about  $1 \text{ cm}^{-1}$ , laser oscillation occurred simultaneously at two transmission peaks of the etalon, but the feasibility of using such a resonator configuration was clearly demonstrated. Etalons with larger free spectral ranges were not available for our experiments at that time, and further frequency tuning experiments with that configuration were not performed.

In the single-line pumping experiments a beam-expander was used to achieve a larger resonator mode beamwaist at the grating as it was shown in Figure 5.9b. The frequency resolution bandwidth of the grating then became so narrow that continuous tuning of the laser frequency between two  $\text{CO}_2$  line centres could be demonstrated without using an additional etalon. The measured laser frequencies as a function of the change in the grating tilt angle are shown in Figure 6.17. A 12 atm gas mixture containing 0.5% DF, 4.2%  $\text{CO}_2$  and 95.3% He was used in this case. We observe that the frequency region between R(16) and R(18) is completely covered. Ignoring the spectral fine structure of the laser gain in the frequency tuning region, the laser frequency would be expected to change linearly with small changes in the grating tilt angle. This is indicated by the linear tuning curve in Figure 6.17. Actually we know that the laser gain will have a complex spectral structure. First, the interaction between overlapping vibrational/rotational lines (see section 3.1.5) will modify the spectrum obtained in the simple theory of independent overlapping of Lorentzian lines and the contribution to the gain from the sequence band lines will further complicate the picture. In particular a line in the first sequence band falls approximately midway between the R(16) and R(18) regular line centres as shown in Figure 6.17. A detailed theoretical analysis of the gain spectrum and the resolution spectrum of the frequency selective elements would be required to find the expected frequency tuning characteristics of the laser, and such an analysis is beyond the scope of this work. The results of Figure 6.17 are also influenced by a backlash in the grating tilt mechanism which we believe is responsible for most of the deviations from the linear tuning curve. It is not possible to draw definite conclusions from these data about the influence of the spectral structure of the gain on the tuning characteristics. We observe, however, that lasing occurs erratically in a broad frequency region when the grating is positioned for laser oscillation midway between the line centres, and this is probably caused by the spectral gain structure. We assume that this effect might have been avoided with carefully positioned apertures in the resonator.



*Figure 6.17 Results of frequency tuning experiments in the case of single-line pumping*  
The vertical line segments represent measured  $\text{CO}_2$  laser oscillation frequency ranges.

frequency tuning characteristics of the laser, and such an analysis is beyond the scope of this work. The results of Figure 6.17 are also influenced by a backlash in the grating tilt mechanism which we believe is responsible for most of the deviations from the linear tuning curve. It is not possible to draw definite conclusions from these data about the influence of the spectral structure of the gain on the tuning characteristics. We observe, however, that lasing occurs erratically in a broad frequency region when the grating is positioned for laser oscillation midway between the line centres, and this is probably caused by the spectral gain structure. We assume that this effect might have been avoided with carefully positioned apertures in the resonator.

The measured laser frequency bandwidth is larger than  $0.2 \text{ cm}^{-1}$  for all positions of the grating. Even if the spectral resolution of our spectrometer contributes with nearly  $0.1 \text{ cm}^{-1}$  to the bandwidth, it is clear that further refinements of the technique are required for narrowband tuning of the laser frequency. An additional etalon might reduce the bandwidth considerably, but since the laser was operated only slightly above the threshold in this experiment, we could not afford the extra resonator losses

that would be introduced by using an etalon. It is possible that a configuration similar to that used in the multiline pumping experiments will be the best practical solution, because lower resonator losses can be obtained in that way. That solution is however inherently more complicated because one has to take into account the complex spectral reflectivity of the mirror-grating "etalon" (see Figure 5.10). Further experiments must be performed to find out which of the configurations that should be preferred.

The  $\text{CO}_2$  laser pulse energies obtained with the grating positioned at the R(18) line centre are plotted as a function of the pumping energy in Figure 6.18. The maximum pulse energy is about 1 mJ, and the pumping threshold is considerably higher than what we measured with the two-mirror resonator in section 6.2.2. Midway between the two line centres the maximum pulse energy was approximately a factor of two lower.

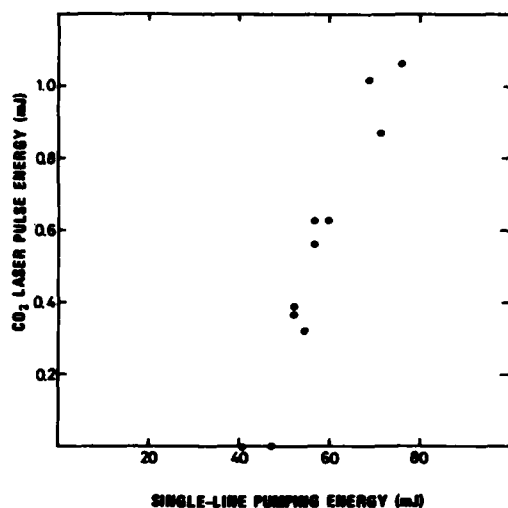


Figure 6.18  $\text{CO}_2$  laser output energy as a function of single-line pumping energy in the frequency tuning experiments. The  $\text{CO}_2$  laser here oscillates at the R(18) line centre at  $974.6 \text{ cm}^{-1}$ .

To our knowledge this is the first time that sufficiently high gain has been obtained in an optically pumped high-pressure  $\text{CO}_2$  laser, to allow the use of frequency selective elements such as a grating and an etalon in the laser resonator. Continuous tuning of the laser frequency over approximately  $5 \text{ cm}^{-1}$  has been demonstrated previously in an optically pumped  $\text{N}_2\text{O}$  laser (61). The tuning was then performed by simply tuning the resonator length of a two-mirror laser resonator, but the oscillation frequency was inherently confined to a narrow spectral region at the peak of the gain spectrum. With the present concept continuous tuning of the laser frequency over broader spectral regions should be possible.

## 7 CONCLUSIONS

In the present work it has been shown that the radiation from a pulsed DF laser can be used for efficient optical excitation of a high-pressure DF $\rightarrow$ CO<sub>2</sub> transfer laser for generation of continuously tunable CO<sub>2</sub> laser radiation. A theoretical model of the optically pumped high-pressure DF $\rightarrow$ CO<sub>2</sub> transfer laser has been developed, and the results of computer calculations based on this model are in reasonable agreement with the experimental results.

The DF laser is a commercially available pumping source in contrast to laser sources that have been used previously for optical pumping of high-pressure CO<sub>2</sub> lasers, and this may lead to a practical use of optical pumping for generation of continuously tunable CO<sub>2</sub> laser radiation.

The experiments have been concentrated on measurements with 10 atm laser gas mixtures, since 10 atm gas pressure is sufficient for complete overlapping between adjacent CO<sub>2</sub> laser lines making continuous tuning of the laser frequency possible. Using single-line DF laser radiation for pumping and a 7% CO<sub>2</sub> laser output coupler, 6 mJ CO<sub>2</sub> laser output pulse energy was obtained, corresponding to a total quantum efficiency of about 20%. The slope quantum efficiency was about 35%, and the peak power was approximately 40 kW. The output energies obtained at 10 atm gas pressure using multiline pumping were in the same range, but the values of the quantum efficiency were uncertain in that case due to uncertainties in the measurements of the absorbed pumping energy. The values listed above are by far the highest that have been reported for an optically pumped high-pressure CO<sub>2</sub> laser (cf Table 1.1).

Continuous tuning of the CO<sub>2</sub> laser frequency between two CO<sub>2</sub> line centres has been demonstrated by using a beam expander and a diffraction grating in the laser resonator. The measured spectral bandwidth of the laser radiation was larger than 0.2 cm<sup>-1</sup> including the 0.1 cm<sup>-1</sup> resolution bandwidth of the spectrometer, and it seems that an additional frequency selective element such as a Fabry-Perot etalon will be necessary to obtain narrow-band tuning of the laser frequency. The influence on the tuning characteristics from variations in the laser gain between the line centres has not been analyzed. Maximum output energies of approximately 1 mJ have been obtained in this case.

CO<sub>2</sub> laser oscillation between the CO<sub>2</sub> line centres has also been demonstrated by using a second mirror in front of the grating and a Fabry-Perot etalon which provided the fine tuning. Further frequency tuning experiments must be performed before it can be concluded which of the configurations should be preferred. To our knowledge this is the first time that frequency selective elements like a grating and an etalon have been used in an optically pumped high-pressure CO<sub>2</sub> laser for demonstration of continuous tuning of the laser frequency (see comments in section 6.3).

The theoretical laser model developed in this work takes into account the effects of line overlapping and the contribution to the laser gain from the sequence bands, which are both important in high-pressure molecular lasers. The interaction between different vibrational/rotational lines has been ignored. The model is based on the assumptions of a characteristic vibrational temperature in each of the vibrational modes and a common temperature for the T/R degrees of freedom. A list of important assumptions and simplifications in the model is given in section 3.3. CO<sub>2</sub> laser pulse shapes and quantum efficiencies as well as the space and time dependences of the pumping laser intensity, the number of excited vibrational quanta in the different vibrational modes and the CO<sub>2</sub> laser gain are calculated using this model.

According to the theoretical calculations there should be only minor differences in the CO<sub>2</sub> laser pulse shapes and in the quantum efficiencies for the various 10 atm



laser gas mixtures used in the experiments. This is partly confirmed by the experimental results, but some significant deviations are observed which show that effects that we have ignored in the theoretical model may be of importance. In particular there are significant differences in the laser oscillation build-up times which we are unable to explain. The formation of pressure waves in the laser gas has been suggested as an explanation for lower output energy and lack of tail in the laser pulse at high DF partial pressure. The effect of pressure waves was most clearly demonstrated in the gain measurements where a strong defocusing of the probing beam was observed. It is however not clear how this effect will influence the performance of the laser. The possibility of a non-Boltzmann distribution in the DF vibrational ladder has been suggested as an explanation for higher transmitted pumping energies in the experiments than in the theoretical calculations.

The calculations show that molecular energy relaxation processes should not seriously affect the quantum efficiencies of this laser system. Fast deactivation of the  $\text{CO}_2$   $\nu_3$  mode by collisions with DF has been pointed out as a possible limiting factor, but the calculations of chapter 4 show that total quantum efficiencies of about 80% should be feasible in a  $\text{CO}_2$  laser resonator where resonator losses other than the output coupling can be avoided. The magnitude of the round trip resonator losses  $\ell_R$  relative to the output coupling  $T_{\text{OUT}}$  is important for the quantum efficiencies that can be obtained, and our results indicate that a high  $\ell_R$  limits the experimental quantum efficiencies. The slope quantum efficiency was approximately the same for all gas mixtures and gas pressures used in the single-line pumping experiments, and this strongly indicates that the slope efficiency is given by the ratio  $T_{\text{OUT}} : \ell_R$ . This gives an  $\ell_R$  in the range of 14–18% for the experiments with the 3.5% output coupler, and it suggests that great improvements in the quantum efficiencies might be obtained in a low-loss laser resonator.

Even though there are some discrepancies between experimental and calculated results, we find that the theoretical model describes many of the essential features of the laser system fairly well. The model is particularly valuable for evaluation of effects such as saturation in the pumping process and the contribution to the laser gain from the sequence bands, and for evaluation of the reduction in the efficiency due to molecular relaxation processes. It also appears that good agreement with output energies and quantum efficiencies can be obtained when the experimentally estimated value of  $\ell_R$  is used in the theoretical model. The disagreements in the pulse shapes and build-up times are significant. It should however be noted that the measured build-up times are within the range of 200–320 ns except for the mixture with the lowest DF partial pressure. By comparison the calculated build-up time is about 220 ns for  $\ell_R = 6\%$  and 280 ns for  $\ell_R = 15\%$  for all the gas mixtures. To our knowledge the present work is the first where the experimental characteristics of an optically pumped high-pressure  $\text{CO}_2$  laser are compared with the results of a reasonably comprehensive theoretical model.

The results of the frequency tuning experiments are promising, but extensions of the work will be required to prove that the laser system can be developed into a practical, continuously tunable laser source. The extra resonator losses caused by the frequency selective elements may be a limiting factor, and special attention should be paid to this problem. An extended series of single-line pumping experiments accompanied by computer simulations should provide a definite conclusion about the magnitude of the resonator losses which seemed to limit the quantum efficiency in the two-mirror laser experiments. If the high loss factor is confirmed, it will be important to find out which components (mirrors or windows) are responsible and what precautions can be taken to reduce the losses. An analysis of the frequency tuning characteristics based upon the spectral characteristics of the laser gain and of the frequency selective elements would be desirable, but the complexity of the spectral gain curve will make this difficult.

This work did not provide a conclusion about which DF pumping laser resonator configuration should be chosen, and it seems that radiation damage problems will be decisive for this question. In multiline operation, using a stable two-mirror DF laser resonator, the pumping beam has a hot-spot pattern which leads to enhanced damage problems. Multiline DF laser operation using an unstable two-mirror resonator should therefore be considered. This might reduce the damage problems, and better matching with the  $TEM_{00}$   $CO_2$  laser resonator mode would also be obtained. The advantage of using multiline pumping is that higher pumping energies are available, even though only the  $(1 \rightarrow 0)$  laser lines are efficient for the excitation. This will be important because the frequency selective elements lead to increased resonator losses and higher pumping threshold in the tuning experiments.

The optical transfer pumping scheme presented in this work may also allow operation with other isotopes of the  $CO_2$  laser molecule or with  $N_2O$ . This might produce continuously tunable laser radiation in a large part of the  $900-1100\text{ cm}^{-1}$  region. However, limited information is available about the kinetics of these systems, and it remains to be seen if they are suitable for high-pressure operation.

We conclude by stating that a new optical excitation scheme for a high-pressure  $CO_2$  laser has been investigated in this work, and the potential of optical pumping as a particularly simple and efficient excitation technique has been demonstrated.

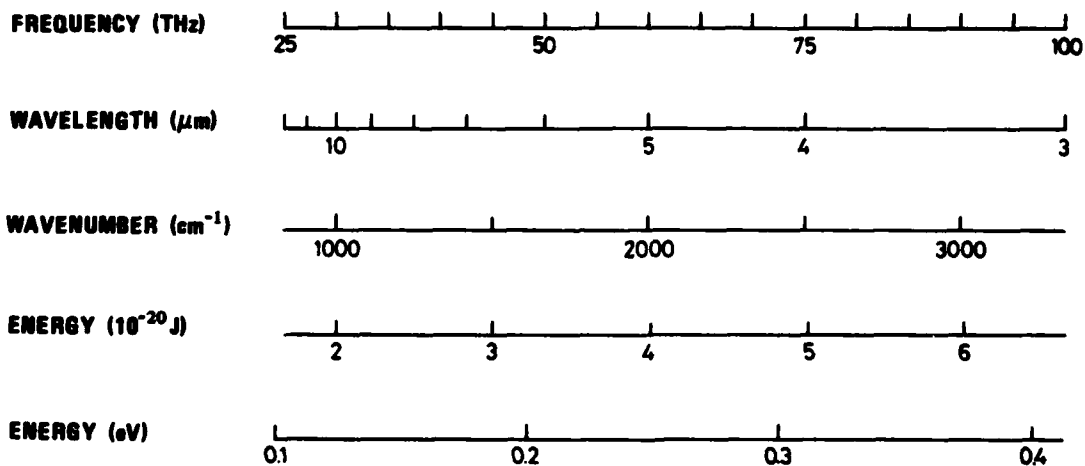
#### Acknowledgements

This work has been done under the supervision of Gunnar Wang to whom the author is deeply indebted for numerous valuable discussions and advice. Thanks are due to Tycho Jæger for stimulating discussions and encouragement during the work. The author is grateful to Christian Holm for coating the dichroic laser mirrors and to Ivar Lie for providing the numerical solutions to the equations in the laser model. Helpful assistance from and cooperation with Stian Løvold, Stig Landrø and Øyvind Christensen are also greatly appreciated.

## APPENDIX A

## UNIT CONVERSION SCALES

The scales given below show the correspondance among the units for the frequency, wavelength, wavenumber and energy of a photon. The correspondance is unique, and we have found it convenient to give the value of the corresponding wavenumber both when referring to the frequency and to the energy. Strictly speaking, this correspondance is only meaningful in the case of a photon, but the wavenumber in units of ( $\text{cm}^{-1}$ ) is commonly used also when referring to atomic and molecular energies as well as the linewidths of atomic and molecular transitions.



## APPENDIX B

## LIST OF SYMBOLS

Symbols that are only used where they are defined are not listed.

$A_{u\ell}$	– spontaneous Einstein coefficient
$\Delta E$	– general notation for energy difference
$g(\nu)$	– line shape function ( $\int g(\nu)d\nu = 1$ )
$I_L$	– CO <sub>2</sub> laser radiation intensity in the laser resonator
$I_{OUT}$	– CO <sub>2</sub> laser output radiation intensity
$I_P$	– DF pumping laser radiation intensity
$I_{OP}$	– constant describing the intensity of the theoretical pumping pulse (equation (4.1))
$J$	– rotational quantum number
$k_x$	– rate of process x
$k_{x,M}^0$	– specific rate constant of process x due to collisions with molecule M
$k_{D1}, k_{D2}, k_{D3}$	– decay rates of the energies in the $\nu_1, \nu_2$ and $\nu_3$ CO <sub>2</sub> vibrational modes
$k_T$	– energy transfer rate from the DF vibrational mode to the CO <sub>2</sub> $\nu_3$ mode
$L$	– general index for the CO <sub>2</sub> laser transition and for the CO <sub>2</sub> laser radiation ( $\alpha_L, \nu_L$ etc)
$L_A$	– internal length of the laser gas cell
$L_C$	– total optical length of the CO <sub>2</sub> laser resonator
$\ell$	– index for the lower CO <sub>2</sub> laser level and for the lower level of the DF absorption transition
$\ell_R$	– total round trip resonator losses
$l$	– quantum number for the vibrational angular momentum of the degenerate CO <sub>2</sub> $\nu_2$ mode
$N$	– molecular density
$N_\ell, N_u$	– population densities of the lower/upper CO <sub>2</sub> laser levels or for the lower/upper levels of the DF absorption transition
$\Delta N$	– population inversion of the CO <sub>2</sub> laser
$\bar{N}_i$	– average number of excited vibrational quanta per molecule ( $i = 1, 2, 3$ – CO <sub>2</sub> vibrational modes, $i = 4$ – DF vibrational mode)
$\bar{N}_i^e$	– equilibrium value of $\bar{N}_i$
$\bar{N}_{12}$	$= \bar{N}_1 + \bar{N}_2 / 2$
OPL	– optically pumped laser
$P$	– general index for the DF absorption transition (pumping transition) and for the DF pumping laser radiation ( $\alpha_P, \nu_P$ etc)
$P(J)$	– P-branch transition (defined in section 3.1.1)
$p$	– gas pressure
$Q, Q_V, Q_R$	– partition functions
$R$	– "rotational"
$R(J)$	– R-branch transition (defined in section 3.1.1)

T	- "translational"
T	- common temperature for the T/R degrees of freedom
$T_i$	- vibrational temperature ( $i = 1, 2, 3$ - $\text{CO}_2$ vibrational modes, $i = 4$ - DF vibrational mode)
$T_{\text{OUT}}$	- output coupling of the $\text{CO}_2$ laser resonator
u	- index for the upper $\text{CO}_2$ laser level and for the upper level of the DF absorption transition
V	- "vibrational"
$v_i$	- vibrational quantum number ( $i = 1, 2, 3$ - $\text{CO}_2$ vibrational modes, $i = 4$ - DF vibrational mode)
z	- position coordinate along the $\text{CO}_2$ laser resonator axis
$z_0$	- Rayleigh distance of a $\text{TEM}_{00}$ Gaussian beam
$\alpha_L$	- $\text{CO}_2$ laser gain coefficient
$\bar{\alpha}_L$	- average $\text{CO}_2$ laser gain coefficient in the $\text{CO}_2$ laser resonator (see equation (3.43))
$\alpha_P$	- absorption coefficient of the DF absorption transition
$\gamma$	- half width at half maximum of Lorentz broadened transitions
$\gamma_L, \gamma_P$	- half widths of the $\text{CO}_2$ laser transition and of the DF absorption transition
$\gamma_M^0$	- specific Lorentz line broadening coefficient due to collisions with the molecule M
$\eta$	- quantum efficiency
$\theta$	- degeneracy (indices u, l, J identify the kind of level involved)
$\kappa$	- Lorentz line overlapping factor (defined in section 3.1.5)
$\lambda_L, \lambda_P$	- $\text{CO}_2$ laser wavelength/DF laser wavelength
$\nu_L, \nu_P$	- $\text{CO}_2$ laser frequency/DF laser frequency
$\nu_i$	- vibrational frequency ( $i = 1, 2, 3$ - $\text{CO}_2$ vibrational modes, $i = 4$ - DF vibrational mode)
$\nu_0$	- line centre frequency
$\rho$	- population probability (quantum numbers will identify the kind of level involved)
$\omega$	- beam radius of a $\text{TEM}_{00}$ Gaussian beam
$\omega_0$	- beam radius at the beam waist

## APPENDIX C

## ENERGY TRANSFER BETWEEN HARMONIC OSCILLATOR VIBRATIONAL MODES

Section 1.7.1 of (27) treats the general theory of energy transfer between two harmonic oscillator vibrational modes a and b with frequencies  $\nu_a$  and  $\nu_b$ . It is assumed that vibrational temperatures  $T_a$  and  $T_b$  describe the populations of the vibrational levels, and the average excitation energies in the modes a and b per molecule are denoted  $E_a$  and  $E_b$ . Assuming that only single vibrational quanta can be transferred in a collision between two molecules, one finds that the following equations describe the transfer process

$$\frac{dE_a}{dt} = -k_T(T, T_b)(E_a - E_a(T, T_b)) \quad (C.1)$$

where

$$E_a(T, T_b) = h\nu_a \cdot \left\{ \exp \left[ \frac{h\nu_b}{kT_b} + \frac{\Delta E}{kT} \right] - 1 \right\}^{-1} \quad (C.2)$$

$$k_T(T, T_b) = k_0 \cdot \left[ \exp \left( \frac{h\nu_b}{kT_b} \right) - 1 \right]^{-1} \cdot \left[ \exp \left( \frac{h\nu_b}{kT_b} \right) - \exp \left( -\frac{\Delta E}{kT} \right) \right] \quad (C.3)$$

$$\Delta E = h\nu_a - h\nu_b$$

T - T/R temperature

$k_0$  - constant

Assuming that a and b are the DF vibrational mode ( $\nu_a = \nu_4$ ) and the  $\text{CO}_2$   $\nu_3$  mode ( $\nu_b = \nu_3$ ) respectively, equation (C.1) corresponds to equations (3.31) and (3.32) of section 3.2.4. Introducing the quantity  $\bar{N}_3$  into equation (C.3) it can be shown that

$$k_T = k_T(T, T_3) = k_0 \cdot \left\{ \bar{N}_3 \left[ 1 - \exp \left( -\frac{\Delta E}{kT} \right) \right] + 1 \right\} \quad (C.4)$$

Since  $\Delta E = h\nu_4 - h\nu_3 \approx 550 \text{ cm}^{-1}$  and  $kT \approx 208 \text{ cm}^{-1}$ , at  $T = 300 \text{ K}$ , we can approximate by ignoring the exponential factor, and we find that

$$k_T \approx k_0(1 + \bar{N}_3) \quad (C.5)$$

With  $k_0 = k_T^0 \cdot p_{\text{CO}_2}$  this corresponds to the expression for  $k_T$  used in equations (3.31) and (3.32).

We also find that  $E_4(T, T_3)$  of equation (C.2) corresponds to  $h\nu_4 \cdot \bar{N}_4^e$  of equations (3.31) and (3.32). The equilibrium condition of equation (3.33) can be found from equations (C.1) and (C.2), using the quantities  $\bar{N}_3$  and  $\bar{N}_4$ .

## APPENDIX D

## CONSTANTS AND PARAMETER VALUES USED IN THE COMPUTER CALCULATIONS

Constants and parameter values used in the computer calculations are summarized below. References are given to the places where they occur in the text or to numbers in the reference list. All temperature dependent parameters are given at  $T = 300$  K.

## a) The DF absorption transition (section 3.2.3)

These data are used in the calculation of  $\alpha_P$ . It is assumed that the 1P(7) DF laser line is used for pumping.

$$\begin{aligned}\nu_{0P} &= 2743.5 \text{ cm}^{-1} \\ A_{ul} &= 31 \text{ s}^{-1} \quad (45) \\ \gamma_P (\text{cm}^{-1}) &= 0.29 \cdot p_{DF} (\text{atm}) + 0.05 \cdot p_{CO_2} (\text{atm}) + 0.005 \cdot p_{He} (\text{atm}) \quad (\text{Table 3.1}) \\ \rho(J=7) &= 0.042 \\ \rho(J=6) &= 0.075\end{aligned}$$

(The values of  $\rho$  are calculated using the DF rotational constants  $B \approx 10.86 \text{ cm}^{-1}$  and  $D \approx 6 \cdot 10^{-4} \text{ cm}^{-1}$  given in (62).)

b) The  $CO_2$  laser transition

These data are used in the calculation of  $\alpha_L$  (section 3.1.5). It is assumed that the  $^{12}O_2$  laser oscillates on R(18) at  $974.6 \text{ cm}^{-1}$ .

$$\begin{aligned}\nu_{0L} &= 974.6 \text{ cm}^{-1} \\ A_{ul} &= 0.19 \text{ s}^{-1} \quad (63) \\ \gamma_L (\text{cm}^{-1}) &= 0.096 \cdot p_{CO_2} (\text{atm}) + 0.061 \cdot p_{He} (\text{atm}) \quad * \quad (41) \\ \kappa &= 1.5 \quad (25, 29) \\ \rho(J=18) &= 0.0728 \\ \rho(J=19) &= 0.0715\end{aligned}$$

(The values of  $\rho$  are calculated using the  $CO_2$  rotational constants  $B \approx 0.387 \text{ cm}^{-1}$  and  $D \approx 1.33 \cdot 10^{-7} \text{ cm}^{-1}$  given in (64).)

\* The broadening of the  $CO_2$  laser lines by collisions with DF is not known, but it should contribute negligibly.

## c) Energy transfer and relaxation processes (sections 3.2.4 and 3.2.5)

$$\begin{aligned}k_T^0 &= 1.5 \cdot 10^8 \text{ s}^{-1} \cdot \text{atm}^{-1} \quad (44, 48) \\ k_{D_2} (s^{-1}) &= 1.1 \cdot 10^5 \cdot p_{CO_2} (\text{atm}) + 2.4 \cdot 10^6 \cdot p_{He} (\text{atm}) \quad ** \quad (\text{Table 3.3}) \\ k_{D_3} (s^{-1}) &= 1.5 \cdot 10^7 \cdot p_{DF} (\text{atm}) + 2.7 \cdot 10^5 \cdot p_{CO_2} (\text{atm}) + 6.5 \cdot 10^4 \cdot p_{He} (\text{atm}) \\ &\quad (\text{Table 3.2})\end{aligned}$$

\*\* The relaxation constant due to collisions with DF is not known.

## d) Resonator parameters

$$L_A = 10 \text{ cm}$$

$$L_C = 22 \text{ cm}$$

$T_{OUT}$  and  $l_R$  are variable input parameters to the computer program.



## APPENDIX E

## SPECTRAL CHARACTERISTICS OF OPTICAL COMPONENTS

Figure E.1 below shows the spectral transmittance of the laser mirrors and the beam-splitter used in the set-up of Figure 5.1. The curves are only given in the frequency regions of the CO<sub>2</sub> laser and of the DF pumping laser.

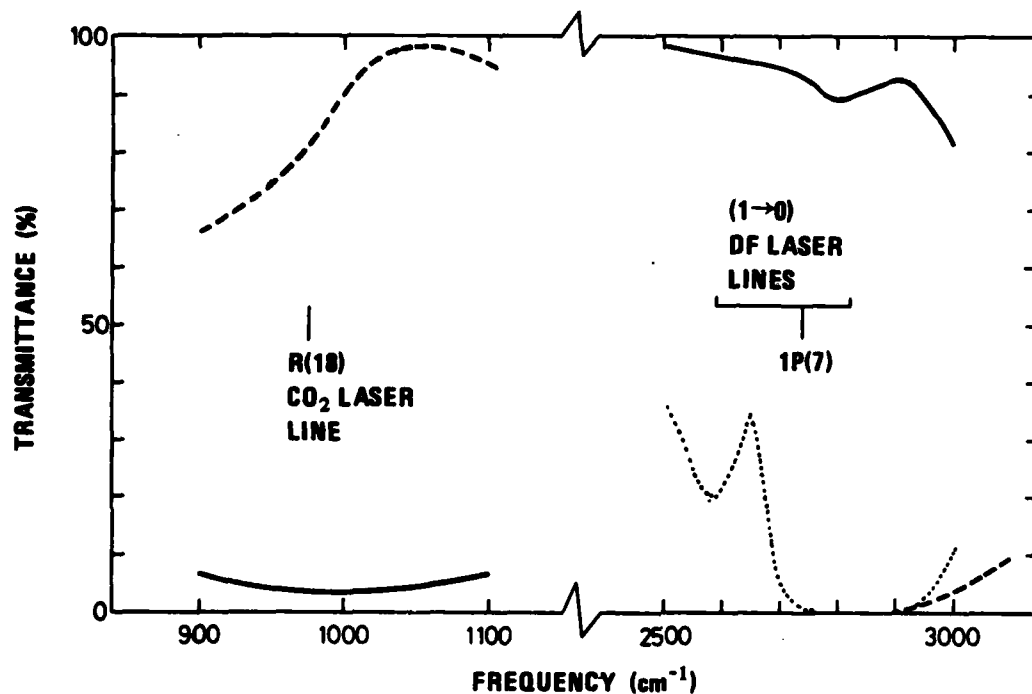


Figure E.1 Spectral transmittance of laser mirror  $M_1$  (solid curve), laser mirror  $M_2$  (dotted curve) and beamsplitter BS (dashed curve)

The transmittance of  $M_2$  is less than 0.5% at CO<sub>2</sub> laser wavelengths. The transmittance of  $M_1$  (output coupling) is approximately 3.5% at the CO<sub>2</sub> laser R(18) line at 975 cm<sup>-1</sup>.

## APPENDIX F

### THE CHOICE OF MATERIALS IN THE GAS HANDLING SYSTEM; GAS MIXING PROCEDURES

Our observations of reactions between the DF gas and the gas handling system were briefly summarized in section 5.5. This appendix will give a more detailed description of the observations and of the gas mixing procedures.

We shall first briefly comment on some of the general properties of the DF gas. The boiling point of DF is as high as 20°C, which means that a maximum DF vapour pressure of about 1 atm can be obtained at room temperature (this was no limitation in our work where much lower DF pressures were used). It is a very corrosive and toxic gas which requires handling with the utmost care. The deuterium is easily backexchanged with hydrogen, and the presence of adsorbed water vapour on surfaces in the gas handling system may be critical. At DF partial pressures above 100 torr the DF molecules start to form polymers, and these are recognized by the presence of broad continuous absorption bands in the infrared spectrum (65). Such polymer absorption was observed in our experiments for DF pressures exceeding 150 torr, and we were concerned about the influence that the polymers might have on relaxation rates in the laser system. It turned out that the optimum DF partial pressure in the laser was considerably lower, and no polymer absorption has been observed in our typical laser gas mixtures.

Besides the corrosive nature of the DF gas, the most serious problem in the preparation of the gas mixtures seems to be adsorption of DF on surfaces in the gas handling system. This is confirmed by the fact that the DF pressure decreases quickly after an amount of DF is filled into the system, and after evacuation the pressure starts to increase due to outgassing. The phenomenon is probably similar to the well-known surface adsorption of water vapour. Since DF is very reactive, it is likely that a combination of adsorption and chemical reaction with the surfaces is responsible for the time evolution of the pressure. A typical time evolution of the pressure in a stainless steel gas cell is shown in Figure F.1. We observe that the pressure drops very quickly the first minutes after filling 110 torr DF into the cell, and several hours later the decay rate decreases to 0.2 – 0.3 torr per hour. It seems natural to believe that the rapid decay at the start is caused by surface adsorption, while the slow decay may be attributed to a chemical reaction.

According to our observations the decay rate depends greatly on the choice of materials in the gas handling system. From the literature it is found that the fluorocarbon plastics teflon and Kel-F and the copper-nickel alloy monel are widely used gas cell materials in spectroscopic studies of DF and HF. This is consistent with recommendations in corrosion guide books. No specific information is found about characteristic chemical reactions or the amount of DF adsorption on surfaces. Sapphire is usually chosen as cell window material, but it could not be used in our laser experiments since it absorbs the CO<sub>2</sub> laser radiation.

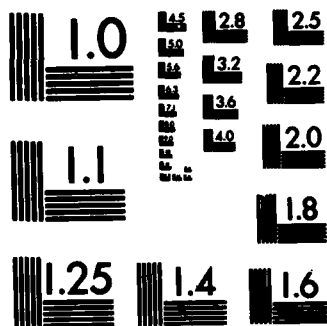
We have tested teflon, monel and stainless steel in the gas handling system. ZnSe has been used for Brewster window material in the laser gas cells, while sapphire was tested in gas cells which were used for measurements of the infrared absorption spectra of DF. The DF pressure was measured by a capacitance manometer (MKS Baratron model 220B), where parts exposed to the gas were made of inconel. This manometer is intended for use with corrosive gases, and it worked without problems during the experiments.

AD-A122 131 CONTINUOUSLY TUNABLE OPTICALLY PUMPED HIGH-PRESSURE DF 2/2  
YIELDS CO2 TRANSFER LASER(U) NORWEGIAN DEFENCE RESEARCH  
ESTABLISHMENT KJELLER K STENERSEN 25 AUG 82  
UNCLASSIFIED NDRE/PUBL-82/1003 F/G 20/5 NL

END

FORMED

DATE



MICROCOPY RESOLUTION TEST CHART  
NATIONAL BUREAU OF STANDARDS-1963-A

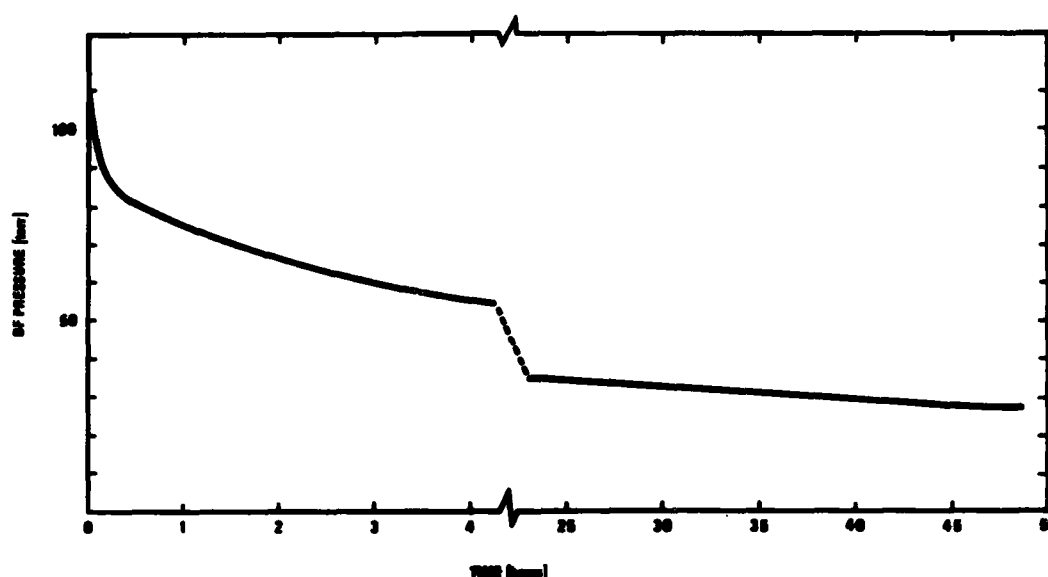


*Figure F.1 Time evolution of the DF pressure after filling 110 torr DF into a stainless steel gas cell*

Our tests have included observations of the time evolution of the DF pressure, measurements of the infrared absorption spectra of the gas and visual observation of the surfaces. The conclusions about the choice of materials can be summarized as follows:

- a) Teflon is the best material with respect to decay of the DF pressure. In a teflon gas cell the pressure decreased typically to 60% of its initial value in three days. Teflon is a relatively soft material, and it was not suited for our high-pressure laser gas cells.
- b) Monel does not seem to be a favourable material, contrary to our expectations from the recommendations in the literature. We found that the DF pressure decreased rapidly after each gas filling, even though the system had been saturated with large quantities of DF several times in advance. No significant signs of chemical attack were observed on the monel surface, and we assume that surface adsorption is responsible for the rapid decay of the DF pressure. A monel laser gas cell was used in all the multiline pumping experiments, and provided that the surfaces were well saturated with DF in advance, we were able to keep the DF pressure variation as low as 2–3 torr during a measurement series which usually lasted 2–3 hours.
- c) The pressure decay rate in stainless steel cells was significantly lower than in monel cells, and it was observed that the decay rate decreased markedly after a cell had been filled repeatedly with DF for a period of some months. The cell surface was then clearly corroded, and we can only suggest that the layer produced by the corrosion may influence the surface adsorption rate. The pressure decay curve shown in Figure F.1 was measured before such "passivation" of the cell had been obtained. A stainless steel laser gas cell was used in the single-line pumping experiments, and after good passivation of the cell it became relatively easy to maintain a constant DF pressure during an experiment. The gas mixing procedure used in these experiments is described at the end of this appendix.

- d) The ZnSe Brewster windows have been used for more than one year without significant signs of chemical attack. The windows are sealed to the gas cell with viton o-rings, and it is unknown whether chemical reactions with these play any role.
- e) Sapphire windows have been used in some of our absorption cells, and they seem to have excellent resistance to chemical attack from DF. For a more permanent sealed-off version of the laser it might be considered to construct a sapphire laser gas cell.
- f) Dielectric coatings have been tested on some of our gas cell windows, but they were seriously attacked by the DF gas. For this reason Brewster windows and external laser mirrors had to be used in the laser experiments.
- g) Infrared absorption spectra of the DF gas showed that the absorption decreased in agreement with the decay of the gas pressure. With the exception of HF (see section 5.5 and Appendix G) no other gases with infrared absorption spectra have been observed in these measurements.

A schematic of the gas handling system is shown in Figure F.2. The following gas mixing procedure was used in the the single-line pumping experiments:

- After evacuating the whole system via valve 4 the DF was filled into the system. Evacuation and filling was repeated twice. The reason for this was that the tubes between valves 1, 2 and 3 had been exposed to air when the gas cell was decoupled at 5 for the previous laser experiment. Water vapour might have been adsorbed at the tube walls in the meantime, and we wanted to exchange as much as possible of the hydrogen in the water by the two first fillings and evacuations. The third time, a DF pressure which was considerably higher than the desired final value was filled in, and valve 2 was closed. We could then observe how the pressure decreased for several hours as in Figure F.1. When the decay rate was less than 1 torr per hour, we reduced the pressure slightly below the desired value. The pressure would then increase slowly before a new decay started, and for a period of 2–3 hours we were able to maintain a nearly constant DF pressure.

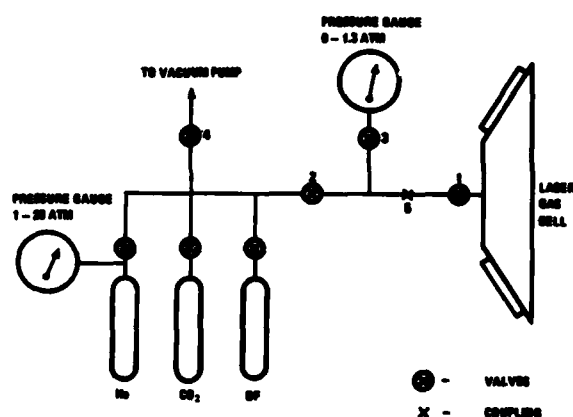


Figure F.2 Schematic of the gas handling system

- When the desired DF pressure had been obtained, valve 1 was closed, the system was evacuated, and CO<sub>2</sub> and He were filled into the cell in turn. No special precautions were taken to ensure homogeneous mixing of the three gases in the cell, but we have not observed effects that indicate inhomogeneous mixing in the experiments.
- Observation of the DF absorption spectrum has been an important test of the DF contents in the laser gas mixtures. A spectrum was always recorded for each gas mixture, and in some cases the spectrum was measured both before and after the laser experiments. No significant changes in the DF absorption were observed between the two measurements, indicating that the DF partial pressure was

constant. We also assume that changes in the spectra would have occurred as a result of redistribution among the gases if the gas mixtures were greatly inhomogeneous.

## APPENDIX G

## IMPURITIES IN THE DF GAS

The presence of a significant fraction of HF was observed in measurements of the infrared absorption spectrum of the DF gas. According to the manufacturer the DF gas should contain less than 2% HF. The DF gas was bought in 10 g quantities in monel lecture bottles from Ozark-Mahoning Company of Tulsa, Oklahoma, which is the only manufacturer of the gas as far as we know. It became clear that the HF content was considerably larger than 2%, but several contacts with the manufacturer did not solve the problem. Four lecture bottles with DF were received, and they all contained a substantial amount of HF.

At first we believed that HF might be formed by chemical reactions with our gas handling system. It was observed that the HF absorption in the infrared spectrum decreased when the system was passivated with the gas several times, and exchange of deuterium with hydrogen in water vapour adsorbed on the surfaces may explain this effect. However, after a few gas fillings the relative strengths of the DF and HF absorptions in the spectrum remained constant. This was observed for all the gas cell materials that were tested, and it therefore seems that HF had been formed during the production of the gas or later by chemical reactions in the lecture bottles.

The determination of the exact fractions of DF and HF from the absorption spectra was not trivial since the resolution bandwidth of our photospectrometer (Perkin-Elmer model PE 580B) was broader than the widths of the DF and HF absorption lines. Uncertainties in the values of Einstein coefficients and Lorentz line broadening coefficients may also lead to errors. It was chosen to compare the absorption on the 1P(9) DF line at  $2693\text{ cm}^{-1}$  with that on the 1P(7) HF line at  $3644\text{ cm}^{-1}$ . The Lorentz self-broadening coefficients and the line centre absorption coefficients are approximately the same for these two lines in pure pressure broadened DF and HF respectively (45, 66). The broadening of the 1P(9) DF line by HF is approximately equal to the self-broadening (47), and we have assumed that the same is the case for the broadening of the 1P(7) HF line by DF, for which no data have been found. Knowing these parameters, it is possible to calculate the DF and HF fractions from an absorption measurement. The procedure that we have used for calculation of the fractions takes into account the effect of the limited instrumental resolution. The details will not be discussed here. Absorption spectra were recorded both of the DF gas (including the HF impurity) and of pure HF gas as a reference. This allowed us to perform the calculations in two different ways which both gave an HF fraction of approximately 20%. Considering the various sources of error we have concluded that the HF fraction should be in the range of  $(20 \pm 5)\%$ .

A second source of impurity may be the formation of  $D_2$  in the lecture bottles by reaction of DF with the walls. The possibility was pointed out by Dr J J Hinchey at United Technologies Research Center, Connecticut, in a private communication. This was examined by cooling the bottles to 77 K and measuring the remaining gas pressure. Practically all the DF should then be in liquid phase, but in three of the bottles gas pressures ranging from 100–150 torr were measured.  $D_2$  formation is a possible explanation for this observation, and it should be noted. In the fourth bottle the remaining pressure was negligible, and gas from this bottle was used in all the laser experiments.



## References

- (1) Walther H, Rothe K W (Eds) (1979): Laser spectroscopy IV, Proceedings of the Fourth International Conference, Rottach-Egern 1979, Springer-Verlag, Berlin, Heidelberg, New York.
- (2) Kompa K L, Smith S D (Eds) (1979): Laser-induced processes in molecules, Springer Series in Chemical Physics, 6, Springer-Verlag, Berlin, Heidelberg, New York.
- (3) Shank C V, Ippen E P, Saphiro S L (Eds) (1978): Picosecond phenomena, Springer Series in Chemical Physics, 4, Springer-Verlag, Berlin, Heidelberg, New York.
- (4) Rockwood S (1976): Uranium isotope separation and its demand on laser development. In: Tunable lasers and applications (Eds A Mooradian, T Jaeger, P Stokseth), Springer-Verlag, Berlin, Heidelberg, New York, 140-9.
- (5) Shen, Y-R (Ed) (1977): Nonlinear infrared generation, Topics in Applied Physics, 16, Springer-Verlag, Berlin, Heidelberg, New York.
- (6) Hinkley E D (Ed) (1976): Laser monitoring of the atmosphere, Topics in Applied Physics, 14, Springer-Verlag, Berlin, Heidelberg, New York.
- (7) Yariv A (1975): Quantum electronics, 2 ed, John Wiley, New York, 210-8.
- (8) Bagratashvili V N, Knyazev I N, Letokhov V S (1971): On the tunable infrared gas lasers, *Opt Commun* 4, 154-6.
- (9) Alcock A J, Leopold K E, Richardson M C (1973): Continuously tunable high-pressure CO<sub>2</sub> laser with UV photopreionization, *Appl Phys Lett* 23, 562-4.
- (10) Harris N W, O'Neill F, Whitney W T (1976): Wide-band interferometric tuning of a multiatmosphere CO<sub>2</sub>-laser, *Opt Commun* 16, 57-62.
- (11) Løvold S, Wang G (1982): Ten-atmospheres high repetition rate rf-excited CO<sub>2</sub> waveguide laser, *Appl Phys Lett* 40, 13-5.
- (12) Løvold S (1981): Continuously tunable high repetition rate rf excited CO<sub>2</sub> laser, FFI/RAPPORT-81/7011, Forsvarets forskningsinstitutt.
- (13) Jones C R (1978): Optically pumped mid-ir lasers, *Laser Focus* 14, 8, 68-74.
- (14) Chang T Y (1977): Optical pumping in gases. In: Nonlinear infrared generation (Ed Y-R Shen), Springer-Verlag, Berlin, Heidelberg, New York, 215-72.
- (15) Chang T Y, Wood O R II (1972): Optically pumped atmospheric-pressure CO<sub>2</sub> laser. *Appl Phys Lett* 21, 19-21.
- (16) Chang T Y, Wood O R II (1973): Optically pumped 33-atm CO<sub>2</sub> laser, *Appl Phys Lett* 23, 370-2.
- (17) Kildal H, Deutsch T F (1976): Optically pumped gas lasers. In: Tunable lasers and applications (Eds A Mooradian, T Jaeger, P Stokseth), Springer-Verlag, Berlin, Heidelberg, New York, 367-77.

- (18) Chang T Y, Wood O R II (1977): Optically pumped continuously tunable high-pressure molecular lasers, *IEEE J Quantum Electron* QE-13, 907-15.
- (19) Chang T Y, Wood O R II (1974): Optical transfer 42-atm N<sub>2</sub>O laser, *Appl Phys Lett* 24, 182-3.
- (20) Wang J H S, Finzi J, Mastrup F N (1977): cw optically resonance pumped transfer laser in DF-CO<sub>2</sub> system, *Appl Phys Lett* 31, 35-7.
- (21) Demtröder W (1981): Laser spectroscopy, Springer-Verlag, Berlin, Heidelberg, New York, 321-74.
- (22) Moulton P F, Mooradian A (1979): Tunable transition-metal-doped solid state lasers, in ref (1), 584-9.
- (23) Stenersen K, Wang G (1981): Optically pumped high-pressure DF-CO<sub>2</sub> transfer laser, *Opt Commun* 29, 251-4.
- (24) Ref (7) pp 99-148.
- (25) Alcock A J, Fedosejevs R, Walker A C (1975): Gain characteristics of a multi-atmosphere UV-preionized CO<sub>2</sub> laser, *IEEE J Quantum Electron* OE-11 767-73.
- (26) Oraevskii A N, Stepanov A A, Shcheglov V A (1975): Kinetics of vibrational exchange in two-component gaseous mixtures in the presence of a resonant laser radiation field, *Sov J Quantum Electron* 4, 876-83.
- (27) Smith K, Thomson R M (1978): Computer modeling of gas lasers, Plenum Press, New York, London.
- (28) Stepanov B I, Trushin S A, Churakov V V (1976): Two-component molecular laser pumped optically in the 4.3  $\mu$ m band, *Sov J Quantum Electron* 6, 715-8.
- (29) Reid J, Siemsen K J (1978): Gain of high-pressure CO<sub>2</sub> lasers, *IEEE J Quantum Electron* QE-14, 217-20.
- (30) Herzberg G (1947): Molecular spectra and molecular structure II, Infrared and Raman spectra of polyatomic molecules, D Van Nostrand Company, Inc, New York.
- (31) Reid J, Siemsen K J (1977): Laser power and gain measurements on the sequence bands of CO<sub>2</sub>, *J Appl Phys* 48, 2712-7.
- (32) Gray L D, Selvidge J E (1965): Relative intensity calculations for carbon dioxide, Part I. Internal partition function, *J Quant Spectrosc Radiat Transfer* 5, 291-5.
- (33) Grunwald E, Dever D F, Keehn P M (1978): Megawatt infrared laser chemistry, John Wiley, New York, 42-.
- (34) Jacobs R R, Pettipiece K J, Thomas S J (1974): Rotational relaxation rate constants for CO<sub>2</sub>, *Appl Phys Lett* 24, 375-7.
- (35) Pack R T (1980): Analytic estimation of almost resonant molecular energy transfer due to multipolar potentials. VV processes involving CO<sub>2</sub>, *J Chem Phys* 72, 6140-52.

- (36) Dang C, Reid J, Garside B K (1980): Gain limitations in TE CO<sub>2</sub> laser amplifiers, *IEEE J Quantum Electron* QE-16, 1097-103.
- (37) Gordietz B F, Sobolev N N, Sokovikov V V, Shelepin L A (1968): Population inversion of the vibrational levels in CO<sub>2</sub> lasers, *IEEE J Quantum Electron* QE-4, 796-802.
- (38) Moore C B, Wood R E, Hu B-L, Yardley J T (1967): Vibrational energy transfer in CO<sub>2</sub> lasers, *J Chem Phys* 46, 4222-31.
- (39) Siemsen K J, Reid J, Dang C (1980): New techniques for determining vibrational temperatures, dissociation and gain limitations in cw CO<sub>2</sub> lasers, *IEEE J Quantum Electron* QE-16, 668-76.
- (40) Dang C, Reid J, Garside B K (1981): Detailed vibrational population distributions in a CO<sub>2</sub> laser discharge as measured with a tunable diode laser. Private communications (The authors work at the Department of Engineering Physics and Physics, McMaster University, Hamilton, Ontario, Canada L8 S 4M1).
- (41) Abrams R L (1974): Broadening coefficients for the P(20) CO<sub>2</sub> laser transition, *Appl Phys Lett* 25, 609-11.
- (42) Miller J L (1978): The high-pressure absorption spectra of the CO<sub>2</sub> 10.6- and 9.4- $\mu$ m bands, *J Appl Phys* 49, 3076-83.
- (43) Zeleznik F J, Svehla R A (1970): Rotational relaxation in polar gases II, *J Chem Phys* 53, 632-46.
- (44) Bott J F, Cohen N (1973): Temperature dependence of several vibrational relaxation processes in DF-CO<sub>2</sub> mixtures, *J Chem Phys* 59, 447-52.
- (45) Bonczyk P A (1975): Determination of Einstein-A and linewidth dependence on pressure for 3.4- $\mu$ m DF spectra, I, Absorption measurements for pure DF. *Phys Rev A* 11, 1522-6.
- (46) Dillon T A, Stephenson J C (1973): Calculation of vibrational and rotational energy transfer between HF, DF, HCl and CO<sub>2</sub>, *J Chem Phys* 58, 2056-64.
- (47) Bonczyk P A (1976): Determination of the linewidth dependence on foreign-gas pressure for 3.4- $\mu$ m DF spectra, *Phys Rev A* 13, 251-2.
- (48) Lucht R A, Cool T A (1974): Temperature dependence of vibrational relaxation in the HF, DF, HF-CO<sub>2</sub> and DF-CO<sub>2</sub> systems, *J Chem Phys* 60, 1026-35.
- (49) Identical to ref (38).
- (50) Taylor R L, Bittermann S (1969): Survey of vibrational relaxation data for processes in the CO<sub>2</sub>-N<sub>2</sub> laser system, *Rev Mod Phys* 41, 26-47.
- (51) Identical to ref (38).
- (52) Manes K R, Seguin H J (1972): Analysis of the CO<sub>2</sub> TEA laser, *J Appl Phys* 43, 5073-8.
- (53) Pechersky M J (1981): Shock waves in pulsed gas lasers, *Laser Focus* 17, 12, 61-7.

- (54) Cohen N, Bott J F (1976): Kinetics of hydrogen-halide chemical lasers. In: Handbook of chemical lasers (Eds R W F Gross, J F Bott), John Wiley, New York, 35-94.
- (55) Deka B K, Dyer P E (1978): Mode control and performance studies of a pulsed unstable resonator HF/DF laser, *IEEE J Quantum Electron* QE-14, 661-73.
- (56) Brink D J, Hasson V (1980): Compact megawatt helium-free HF/DF lasers, *J Phys E: Sci Instrum* 13 553-6.
- (57) Siegman A E (1974): Unstable optical resonators, *Appl Opt* 13, 353-67.
- (58) Krupke W F, Sooy W R (1969): Properties of an unstable confocal resonator CO<sub>2</sub> laser system, *IEEE J Quantum Electron* QE-5, 575-86.
- (59) Damage threshold stated by II-VI Incorporated, who manufactures the ZnSe components used in our experiments.
- (60) Hinch J J (1973): Vibrational relaxation of hydrogen and deuterium fluorides, *J Chem Phys* 59, 233-40.
- (61) Chang T Y, McGee J D, Wood O R II (1976): Continuous tuning of a single laser mode over 5 cm<sup>-1</sup> in a high-pressure N<sub>2</sub>O/CO<sub>2</sub> transfer laser, *Opt Commun* 18, 279-81.
- (62) Huber K P, Herzberg G (1979): Molecular spectra and molecular structure. IV, Constants of diatomic molecules, Van Nostrand, New York, 306.
- (63) Biryukov A S, Volkov A Y, Kudryavtsev E M, Serikov R I (1976): Analysis of the data on spontaneous emission probabilities and collisional broadening cross sections of 00<sup>0</sup>1-10<sup>0</sup>0 lines of the CO<sub>2</sub> molecule, *Sov J Quantum Electron* 6, 946-50.
- (64) Rothman L S, Benedict W S (1978): Infrared energy levels and intensities of carbon dioxide, *Appl Opt* 17, 2605-11.
- (65) Smith D F (1958): Hydrogen fluoride polymer spectrum, hexamer and tetramer, *J Chem Phys* 28, 1040-56.
- (66) Hinch J J, Hobbs R H (1979): Pressure-broadened linewidths in the 2.5 μm band of HF and the influence of polymer formation, *J Opt Soc Am* 69, 1546-9.

